Spin Texture Formation in Perovskite-Based Artificial Spin Ice Structures

By

DAYNE YOSHIKI SASAKI
DISSERTATION

Submitted in partial satisfaction of the requirements for the degree of

DOCTOR OF PHILOSOPHY

in

Materials Science & Engineering

in the

OFFICE OF GRADUATE STUDIES

of the

UNIVERSITY OF CALIFORNIA

DAVIS

Approved:

_____
Yayoi Takamura, Chair

_____
Jeremy Mason

_____
Rajesh Chopdekar

Committee in Charge

2024

Spin Texture Formation in Perovskite-Based Artificial Spin Ice Structures

ABSTRACT

Artificial spin ices (ASIs) are lithographically-patterned arrays of interacting magnetic nanoislands which have traditionally been designed such that each nanoisland possesses an Ising-like magnetic configuration (i.e., behaves as a bar magnet). These systems were originally introduced as an engineered analog of spin-ice crystals whose atomic-level magnetic ordering could be emulated and visualized with conventional magnetic microscopy techniques. Since this initial study, ASIs have served as a platform for designing and investigating phenomena including phase transitions between different global magnetic ordering states, magnetically-reconfigurable spin wave dynamics, and computation in nanomagnet-based devices.

Many ASI studies have used $Ni_{80}Fe_{20}$-based nanoislands whose material and geometric properties enforce the formation of uniform, Ising-like magnetizations in each nanoisland. While these systems have facilitated the investigation of magnetic ordering phenomena in various array geometries, ASIs fabricated from ferromagnetic complex oxides offer opportunities to explore how the nanoisland material properties and magnetostatic interactions can influence the behavior of the individual nanoislands and ASI as a whole. Understanding how these magnetic parameters can tailor the nanoisland functionalities will be essential in the development of nanomagnet-based computing devices.

This dissertation focuses on ASIs fabricated from the ferromagnetic perovskite oxide $La_{0.7}Sr_{0.3}MnO_3$ (LSMO) to understand how the interaction between magnetostatically-coupled nanostructures can influence the formation of spin textures. Soft x-ray photoemission electron microscopy (X-PEEM) was used to perform magnetic domain imaging of LSMO-based ASIs. Through these imaging studies, these systems were observed to allow the formation of both Ising

states, observed in traditional ASI systems, as well as complex spin textures (CSTs), comprised of single and double vortices. The formation of these different spin texture states were found to be sensitive to the ASI geometry as well as the magnetization of the neighboring nanoislands. Through the use of micromagnetic simulations, an energetic analysis of the system was performed which revealed how spin texture formation arises from a competition between effects intrinsic to each nanoisland as well as the magnetostatic interaction between adjacent nanoislands. This competition is facilitated by the unique combination of magnetic material properties of LSMO.

The unusual domains stabilized in LSMO-based ASIs also raises the question of the relaxation kinetics of CST-bearing ASI systems. Insights into the thermal relaxation behavior of LSMO-based ASIs was provided using X-PEEM and an *in-situ* pulsed annealing protocol which allows for "snapshots" of the time-dependent relaxation to be acquired. By tracking the domain changes in each nanoisland as a function of the annealing time, several types of apparent domain conversion were observed whose relative transformation rates evolved over time. These results suggest that the domain formation kinetics of each individual nanoisland is sensitive to the evolving magnetizations of the neighboring nanoislands.

These static and dynamic studies of LSMO-based ASIs demonstrate how magnetostatic interactions can be used to tailor spin texture formations in these systems. Moreover, this work highlights the potential for material-driven ASI studies to provide deeper insights into ASI and domain formation physics.

ACKNOWLEDGEMENTS

There are many people to whom I owe my gratitude for making this journey of pursuing a Ph.D. possible (and somewhat less painful). Above all else, I owe my deepest gratitude to Prof. Yayoi Takamura who not only guided me with the utmost patience throughout my studies, but who offered me the opportunity to begin my journey in a field I was deeply interested in but had no prior experience in. While I had a lack of experience in the field of thin films and nanomagnetism, she let me join her group and provided encouraging and consistent mentorship. Despite her numerous responsibilities as the department chair, she always made the effort to take time out of her busy schedule to address the numerous questions I had and review the seemingly infinite number of manuscript drafts I had. I'm forever grateful for her deciding to take me under her wing. That being said, I still refuse accept that she beat me by five points in our last group bowling match.

I would also like to thank Prof. Jeremy Mason for serving on my committee and for his support and guidance, especially during the early years of my graduate studies. His insights in optimal transport methods has allowed for the development of image analysis code which greatly accelerated the analysis of the magnetic micrographs studied in this dissertation. His mentorship and guidance during some of the low points in my journey helped me become a more confident and knowledgeable researcher. I would also like to thank Dr. Rajesh Chopdekar for serving on my committee and introducing me to the field of artificial spin ices. His guidance and answers to my numerous questions helped set a strong foundation for my dissertation work.

Over the past several years, I have had the opportunity to work with many individuals to perform collaborative research, which may or may not involve us collectively banging our heads against the wall trying to figure something out. I would like to first thank the current and former members of Prof. Yayoi Takamura's research group for their invaluable help and discussions

throughout my time at UC Davis. I thank Dr. Alex Kane, Dr. I-Ting Chiu, and Nolan Ahlm for mentoring me during my early years in the group, showing me how to operate the different laboratory instruments, synchrotron beamlines, and providing guidance on understanding the photon and magnetism physics our group deals with. It was my pleasure to work alongside Dr. Mingzhen Feng, who joined Prof. Takamura's group with me. I thank her for the insightful discussions we've had and for sharing the pain in managing lab-related affairs and running beamtime shifts. I especially thank Nolan Ahlm, Peter Klavins of the Physics Department, and Pete Janutolo at Bruker, for helping to resolve the seemingly infinite number issues with the x-ray diffractometer. I thank all the current and former students who have helped me with performing research and endured my mentoring as I figured out my own leadership and mentoring style: Tanaya Sahoo, Daniel Jiang, Peter Carlson, Zachary Turley, Izoah Snowden (now a graduate student in our group!), Oscar Ryan, and Alexander Solakhyan. I also would like to thank Ishmam Nihal and Hudson Shih for their insightful discussions and taking ownership over the laboratory instruments and affairs I once oversaw.

My deepest gratitude goes out to Dr. Scott Retterer at the Center for Nanophase Materials Sciences at Oak Ridge National Laboratory, who has spent the time and effort in performing electron beam lithography of my perovskite samples. Without his effort, this dissertation work would not have been possible. I am also grateful to Prof. Roopali Kukreja for helping advance my knowledge of structures and thin film processing through her coursework as well as allowing me to use her vibrating sample magnetometer.

I would also like to express my gratitude to the Dichroism Group at the Advanced Light Source, who I have had the opportunity to work closely with the support of the US Department of Energy Office of Science Graduate Student Research program. I'd like to thank Dr. Padraic Shafer

and Dr. Christoph Klewe for allowing me the opportunity to work and learn from them at Beamline 4.0.2 as well as having the confidence that I wouldn't leave their endstation as a smoldering pile of ash by the time I left. I thank the entire Dichroism Group, Dr. Padraic Shafer, Dr. Christoph Klewe, Dr. Alpha N'Diaye, and Dr. Barat Achinuq; for their mentorship, guidance, and patience as I performed my work at the Advanced Light Source. Moreover, I am grateful to Vinnie Aromin and Paul Switzer for helping me with solving the numerous engineering and electrical problems I encountered in my work. I would also like to thank the friends I have made at the Advanced Light Source for the fun and insightful discussions we have had: Dr. Stephanie Corder, Dr. Cindy Lee, Dr. Greg Su, Dr. Abe Levitan, Dr. Sophie Morley, Dr. Sujoy Roy, David Malone, Isaac Zakaria, Alexandr Razumtcev, and Nick Russo. I must also express my deepest gratitude to Dr. Andreas Scholl for providing user support for the PEEM3 microscope, despite his ongoing duties as the Deputy for Science and the Interim Director of the Advanced Light Source.

I would like to thank the friends I have made over the years who have made my time in graduate school all the more enjoyable. Special thanks goes to the members of Prof. Roopali Kukreja's group, Jugal Mehta, Meera, Dr. Rahul Jangid, Pooja Rao, Dr. Nanna Hagström, Scott Smith, CunShuo Li, and Emma Bernard, who never made any outings a dull moment. And I would also like to thank Dr. Daniel Vong, Sean Russell, Chad and Yvonne Conzelmann for the great times we've had together here in Davis.

Last, but certainly not least, I would like to thank my parents and sister for their never-ending love, support, and faith in me as I set forth on this journey.

Table of Contents

Chapter 1: Introduction

1.1 – Artificial Spin Ice

Artificial spin ices (ASIs) are arrays of interacting magnetic nanoislands produced through lithographic techniques [1]. Traditionally, ASIs were engineered such that each nanoisland possessed single domains magnetized along the nanoisland length, resulting in the nanoislands behaving as Ising-like macrospins [2]. These Ising-like states can be engineered through careful selection of nanoisland properties and geometries, the details of which will be discussed in the Section 1.3. In ASIs, a wide variety of complex behaviors have been observed which arise from dipolar interactions between the nanoislands. These complex behaviors range from excitations resembling magnetic monopole-like defects [3–5], phase transitions between different global nanomagnetic ordering states [6–8], and magnetically-reconfigurable spin-wave dynamics [9].

An important feature of ASIs is that their physics strongly depends on how the system is designed. Using different materials and ASI geometries can introduce substantial changes to the physics of the system. Moreover, the collective properties of an ASI strongly depends on how the individual nanoislands are magnetized. Thus, ASIs have received attention for their promising potential for developing low-power computing devices with functionalities that can be magnetically reconfigured after fabrication, such as tunable GHz-frequency dynamics in ASI-based magnonic crystals [9] and switchable gate operations in nanomagnetic logic architectures [10].

As will be discussed later in this chapter, this dissertation work focuses on using ASIs as an experimental platform to investigate spin texture formations in interacting nanoislands. In this section, I will discuss several aspects of ASI research starting with the concept of geometric

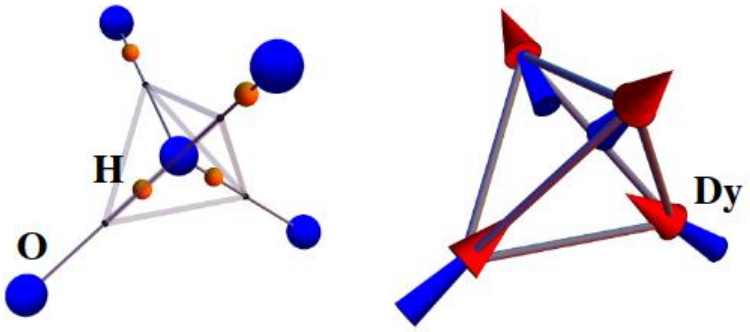

Figure 1.1: *Schematics of the ice rule in water ice (left) and a spin ice (right) material $Dy_2Ti_2O_7$ [11]. "H" and "O" corresponds with the hydrogen and oxygen ions in water ice. "Dy" corresponds with the magnetic moment of the dysprosium ion.*

frustration which serves as the physical foundation for many ASI studies. I then discuss three types of experimental degrees of freedom that have been controlled to explore different ASI physics.

1.1.1 – Geometric Frustration

As the name implies, ASIs are artificial versions of magnetic materials called spin ices. In spin ices, the arrangement of *spins* in the crystal resembles arrangements of water molecules in *ice* (hence, spin ice) [2]. Such materials include members of the pyrochlore family of crystals including dysprosium titanate ($Dy_2Ti_2O_7$) and holmium titanate ($Ho_2Ti_2O_7$) [11]. In *water* ice, the lowest energy arrangement of water molecules consists of having each O^{2-} (blue balls in Figure 1.1) surrounded by a tetrahedron of four H^+ (orange balls). Additionally, the two sets of H^+ are either near to or far away from an O^{2-} ion in the tetrahedral ordering of the ice. This arrangement is referred to as the "two-in, two-out" ice rules. In *spin* ice crystals (right diagram in Figure 1.1), spins are arranged on a tetrahedral lattice. For the example shown in Figure 1.1, the spins corresponds with the spin magnetic moments of the Dy^{3+} ion in $Dy_2Ti_2O_7$. Due to the [111] crystalline anisotropy, the spins become Ising-like (i.e., can have only 2 states/orientations) and

can only point into or away from the tetrahedra [11]. The lowest energy orientations of these spins also obey the ice rule: for a given tetrahedron two spins point in a tetrahedra while two point out.

The spins in spin ices experience geometric frustration. Frustration is the inability for a system to minimize all interactions *simultaneously*. Spin ices are *geometrically* frustrated since the simultaneous minimization of all interactions between the spins cannot be minimized because of the geometry they are placed in. Specifically, the interaction which facilitates the "2-in, 2-out" spin ice behavior is the dipolar interactions between the magnetic moments of the lanthanide ions [12]. A simplified example of geometric frustration is shown in Figure 1.2, where "↑" and "↓" spins are placed on the vertices of a square and triangle. Assuming these spins experience antiferromagnetic exchange coupling (i.e., the spins want to be antiparallel with their immediate neighbors) and behave as Ising states (can only be "↑" and "↓"), for the case of the diamond, all four spins can be placed such that all neighboring spins have antiparallel alignment, therefore minimizing all interactions simultaneously. For the case of triangle, two spins can be placed at any vertices and have antiparallel alignment. However, placing a third spin will always result in one pair of unfavorable interactions because of the lattice geometry.

Geometric frustration in magnetic crystals can be probed using sample -averaged magnetic scattering or spectroscopy techniques, such as neutron scattering or susceptibility measurements [13]. However, directly visualizing the arrangement of the individual spins in frustrated magnets is practically difficult to accomplish. Moreover, studies of geometric frustration in single crystals are constrained to the specific lattice the material has, thus preventing the investigation of frustration in lattices of arbitrary geometries. ASIs were introduced by Wang *et al.* [2] as an two-dimensional engineered analog of spin ice crystals whose frustrated interactions

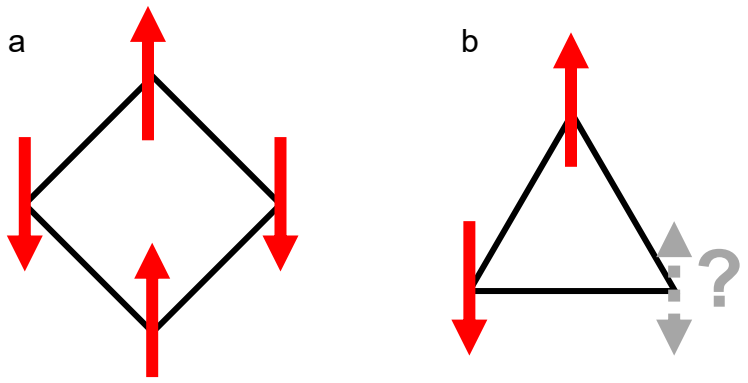

Figure 1.2: *Examples of geometric frustration in antiferromagnetically-coupled spins placed on the corners of a (a) diamond and (b) triangle. The interaction between neighboring spins connected by the polygon edge is minimized only if they are antiparallel.*

occur between magnetic nanoislands (~100 nm dimensions) rather than individual spins. Therefore, the frustrated physics in ASIs can be directly visualized using conventional magnetic microscopy. Moreover, as will be discussed below, frustration can be controlled by altering the geometry the nanoislands are placed in, a behavior that cannot be readily investigated in spin ice systems.

1.1.2 – Geometric Degrees of Freedom

One important area of interest in the field of ASIs is investigating how degrees of freedom associated with the array geometry influences the collective behavior of the nanomagnets. This collective behavior defines the ground state configuration of these systems and influences how readily such states can be experimentally accessed (i.e., the relaxation kinetics). In these systems, the *type* of array geometry used strongly influences the dipolar interactions between nearest-neighboring nanoislands and influences the collective physics in these systems. These studies have explored a wide range of ASI array geometries as shown in Figure 1.3. Additionally, the interaction strength between the dipolar coupled nanoislands can be modulated through changes in both the nanoisland size as well as interisland spacing. The geometric tunability of these systems have led

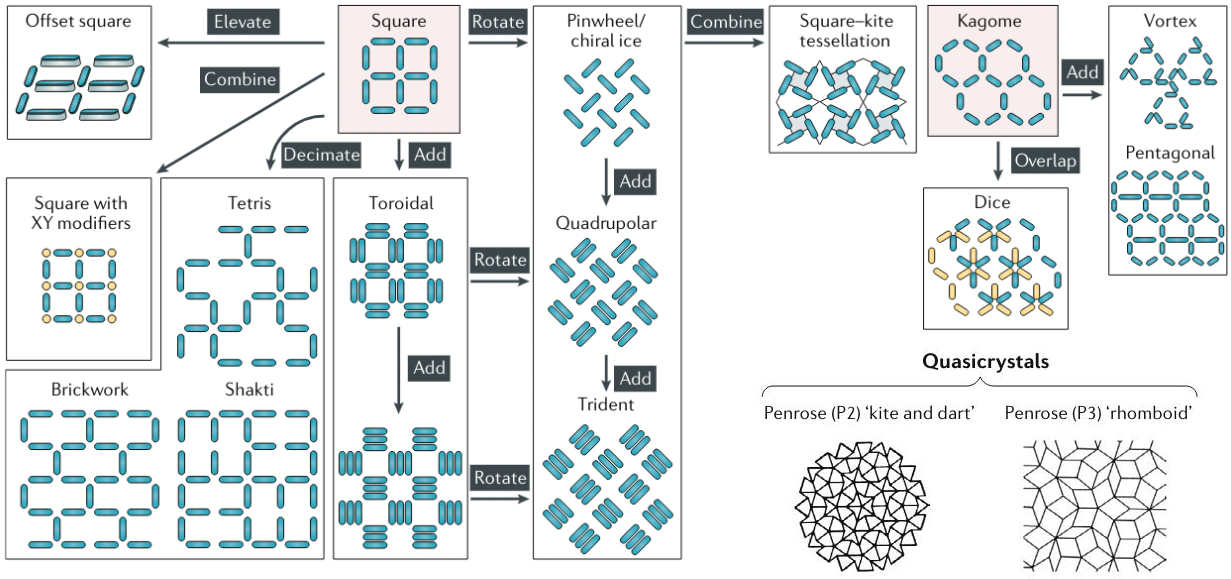

Figure 1.3: *Examples of different 2D and 3D magnetic nanoisland arrangements explored in the field of ASIs [1].*

some to describe ASIs as a "playground" for studying magnetic frustration [14–17].

The dipolar coupling energy between identical nanoisland pairs with moments $\boldsymbol{m_i}$ and $\boldsymbol{m_j}$ can be modeled for Ising-like ASIs as

$$E_{dip} = \frac{\mu_r \mu_0 m^2}{4\pi}\left[\frac{\hat{\boldsymbol{m}}_i \cdot \hat{\boldsymbol{m}}_j - 3(\hat{\boldsymbol{m}}_i \cdot \hat{\boldsymbol{r}}_{ij})(\hat{\boldsymbol{m}}_j \cdot \hat{\boldsymbol{r}}_{ij})}{r_{ij}^3}\right] \propto \frac{m^2 U_{ij}}{r_{ij}^3} \qquad \text{Eq. 1.1}$$

where μ_r is the relative permeability of a medium with respect to the vacuum permeability μ_0, $\hat{\boldsymbol{m}}$ is the unit magnetization of $\boldsymbol{m}$ with magnitude m, $\hat{\boldsymbol{r}}_{ij}$ is the unit direction between the centers of the moments with distance r_{ij}, and $U_{ij} = [\hat{\boldsymbol{m}}_i \cdot \hat{\boldsymbol{m}}_j - 3(\hat{\boldsymbol{m}}_i \cdot \hat{\boldsymbol{r}}_{ij})(\hat{\boldsymbol{m}}_i \cdot \hat{\boldsymbol{r}}_{ij})]$. The three terms in the right-most form of Eq. 1.1 summarizes the geometry-dependence of E_{dip} in ASIs: (1) increasing m or decreasing r_{ij} increases the magnitude of E_{dip} (i.e., increases the interaction strength between nanoislands) and (2) E_{dip} depends on U_{ij}, which describes how E_{dip} changes with different orientations of the Ising-like moments. In other words, for a fixed r_{ij}, changing the lattice geometry alters E_{dip} through U_{ij}. To illustrate how the geometric degrees of freedom influence the ASI physics, I'll discuss studies performed on two ASI lattice geometries relevant to this dissertation:

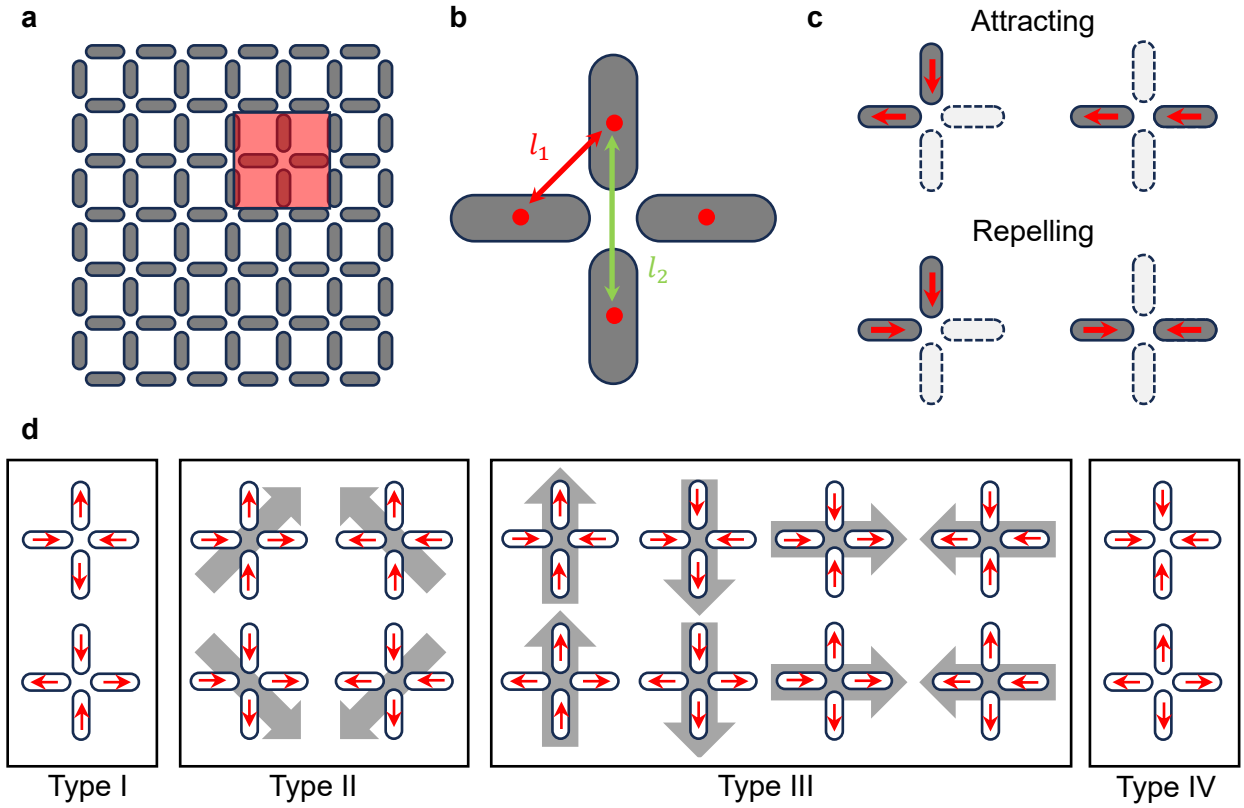

Figure 1.4: *(a) Schematic of the square ASI. (b) Close-up schematic of the ASI vertex (red box in (a), where the strongest nanoisland interactions occur. The distances l_1 and l_2 indicate the unequal distance between the centers (red dot) of the perpendicular nanoislands (l_1) and nanoislands across the vertex (l_2). (c) Schematics of the attracting and repelling Ising magnetization configurations, where the red arrows indicate the nanoisland magnetization. (d) The 16 possible Ising magnetization configurations for the square ASI vertex. The 16 states are grouped into four classes based on degeneracy and are labeled based on the relative dipolar interaction energy (i.e., $E_{Type\ I} < E_{Type\ II} < E_{Type\ III} < E_{Type\ IV}$). The large gray arrows indicate the net magnetization of the nanoislands set.*

the square and brickwork ASI.

1.1.2.1 – Square Artificial Spin Ice

The first ASI introduced by Wang *et al.* (e.g., Figure 1.4(a)) had arrangements of

nanoislands which resembled a square grid and was thus referred to as the square ASI [2]. In ASIs, the strongest dipolar interactions between the Ising-like nanoislands occur at the vertices of the square array (Figure 1.4(b)) where the nanoisland tips were in the closest proximity. At each vertex, there are 16 possible ways to arrange the Ising-like moments as shown in Figure 1.4(d). However, these configurations have varying degrees of degeneracy and are subdivided into four vertex types (Type I-IV) numbered based on their relative dipolar energies (i.e., $E_{Type\ I} < E_{Type\ II} < E_{Type\ III} < E_{Type\ IV}$). As the nanoisland separation decreased, the ASI trended from a random configuration (i.e., populations of Type I-IV vertices were representative of their multiplicities) to one which had a majority of vertices (over 70%) with the ice-like Type I and II configurations [2]. In other words, decreasing the nanoisland separation (r_{ij} in Eq. 1.1) increased the nanoisland interaction and motivated the formation of lower-energy Type I and II vertices.

The Type I and II vertices obey the ice rules as two Ising moments point into a vertex while two Ising moments point away. However, these two states have different energies as a result of the unequal distances between adjacent nanoislands (l_1 in Figure 1.4(b)) and nanoislands across a vertex (l_2 in Figure 1.4(b)). This behavior results in a difference in interaction strength between these two types of nanoisland arrangements. Thus, the ground state for a square ASI is 2-fold degenerate and consists of a system that has only Type I vertices. Additionally, in the ground state, nanoislands are magnetized such that they form loops of magnetization around the square-voids in the ASI. The ordering in square ASIs is said to be antiferromagnetic from two different viewpoints: (1) neighboring pairs of parallel islands have antiparallel moment alignment and (2) neighboring pairs of magnetic loops have opposite chirality. The first attempts to access the square ASI ground state were performed using ac field demagnetization [2,18], which demonstrated that field-based protocols are not sufficient to establish a global Type I configuration. Subsequent studies used

thermal annealing protocols to successfully drive the ASIs into a global ground state configuration [19–24], the details of which will be elaborated on in Section 1.1.3.

While the square ASI possesses a two-fold degenerate ground state, a true square ice requires that all ice-rule-compliant vertices (i.e., Type I and II) are degenerate. Various approaches have been used to fabricate ASIs that can experimentally reproduce the square ice model. One such method involves elevating sets of nanoislands in the out-of-plane direction to equalize all interactions at the square ASI vertex (i.e., "offset square" in Figure 1.3, [25]). Another method involves placing magnetic nanodisks at each vertex to modify the interactions between the nanoislands ("square with XY modifier" in Figure 1.3, [26]).

As shown in Figure 1.3, the square ASI also served as a parent system for several different array geometries created by either systematically removing ("decimate"), adding, and/or rotating nanoislands. Additionally, different ASI types based on hexagonal and quasicrystal lattices have also been explored. These explorations were motivated by the ability to fundamentally alter the *collective* physics of the ASI by simply changing the placement of the individual dipolar-coupled nanoislands. This dissertation work primarily focuses on investigating the square and brickwork ASI lattices, the latter of which will be discussed in the following section.

1.1.2.2 – Brickwork Artificial Spin Ice

The brickwork ASI lattice is formed by selectively removing nanoislands from the square ASI lattice until the voids between the nanoislands resemble tiling of bricks as shown in Figure 1.3 and 1.5. As a result, the vertices in brickwork ASIs contain three nanoislands which can be magnetized into $2^3 = 8$ unique Ising configurations. Similar to the ASI, the brickwork ASI has a two-fold degenerate ground state. However, the brickwork ASI possess a lower two-fold rotational

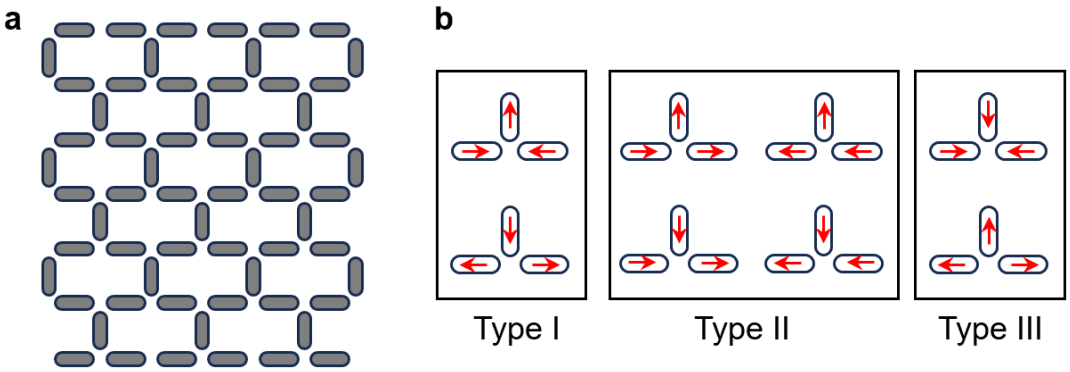

Figure 1.5: *(a) Schematic of the brickwork ASI. (b) The eight possible Ising magnetization configurations for the brickwork ASI vertex. The eight states are grouped into three classes based on degeneracy and are labeled based on the relative dipolar interaction energy (i.e.,* $E_{Type\ I} < E_{Type\ II} < E_{Type\ III}$*).*

symmetry while the square has a higher four-fold rotational symmetry.

The lattice of the brickwork ASI is topologically identical to the six-fold symmetric Kagome ASI lattice. That is, vertices in both systems have identical vertex connectivity (i.e., each vertex is linked to three other vertices via the nanoislands) and transformations between the two ASIs can be performed by changing the angles between the nanoislands from 120° (Kagome ASI) to 90°/180° (brickwork ASI). Despite being topologically identical, the two ASI systems exhibit markedly different pair-wise nanomagnet correlations and abilities to access ground state configurations during ac demagnetizing experiments [27]. This behavior illustrated how the ASI behavior is more sensitive to the lattice geometry, which controls the symmetry of the vertex-level interactions, rather than the lattice topology.

Despite exhibiting similarities to the square and Kagome ASI, the brickwork ASI has received relatively less attention. The few studies performed on this system focused on investigating its magneto-transport response [28], ground state accessibility using field-dependent

protocols [27,28], simulated thermodynamic properties [29], and GHz-frequency response [30]. Consequently, experimental studies of the thermal behavior in brickwork ASIs remains unexplored, in contrast to the square and Kagome ASI systems where such behaviors have been extensively investigated.

1.1.3 – Materials-Based Degrees of Freedom

Traditionally, ASIs have been fabricated from the soft ferromagnetic alloy called permalloy ($Ni_{80}Fe_{20}$). The magnetic properties of permalloy can facilitate the formation of Ising-like magnetic domains in elongated nanoislands, where the magnetizations are parallel with the nanoisland length. In other words, fabricating ASIs from permalloy thin films allows the system to be modeled within an Ising framework and serve as an experimental model to study geometrically frustrated Ising spins. While permalloy-based ASI systems have facilitated the investigation of magnetic frustration and dynamics in various array geometries, exploration of different material systems introduces unique opportunities for ASI studies.

One strategy towards this direction is to fabricate ASIs from single layers of a material *other* than permalloy. In an effort to study thermal activity in ASIs, several groups studied ASIs fabricated from $Gd_{0.3}Co_{0.7}$ [19,20] and $FePd_3$ [21] thin films, which exhibits bulk Curie temperatures near 500 K. Since studies of thermal activities require either ultrathin (~3 nm) nearly superparamagnetic nanoislands or near Curie point temperature, these two material systems are advantageous over permalloy, which possesses a bulk Curie temperature near 800 K [22] and, therefore, have a higher risk of thermally-induced interdiffusion or oxidation. Chopdekar *et al.,* demonstrated that ASIs fabricated from the ferromagnetic perovskite oxide $La_{0.7}Sr_{0.3}MnO_3$ (LSMO) can exploit the T_C of LSMO (~350 K) to thermally anneal the system into a ground state without requiring the use of ultra-thin layers or temperatures well above room temperature [23].

Another material property exploited for ASI-related studies is the magnetocrystalline anisotropy, which causes the material to preferentially magnetize along certain crystallographic directions (as discussed in Section 1.3). Specifically, Louis *et al.* [31] demonstrated that 300 nm x 300 nm x 2 nm Fe square nanoislands can establish a four-state Potts model by exploiting the magnetocrystalline anisotropy of Fe (i.e., the squares have magnetizations which lie along the in-plane ⟨100⟩ easy directions of the Fe film). This behavior is in contrast with the nanoislands used in ASIs, which are designed to behave as Ising states (i.e., only two available magnetization orientations).

Heterostructured (i.e., multilayered) thin films also present unique opportunities to introduce magnetic interfacial interactions to the physics of an ASI. Parakkat *et al.* fabricated square ASIs from bilayers of ferromagnetic Fe and antiferromagnetic IrMn which exhibit an phenomenon called exchange bias [32,33]. In exchange biased systems, the behavior of the ferromagnetic layer is influenced by a directional anisotropy induced by the antiferromagnetic layer [34]. In other words, materials and ASIs with exchange bias can behave as if there is an external magnetic field built into the system, thus favoring magnetizations oriented along the exchange bias direction. In square ASIs, it was shown that these exchange biased nanoislands altered the energies and degeneracies of the different vertex configurations [32]. By altering the relative strengths of the exchange bias and dipolar fields [32] or selectively introducing exchange biased nanoislands in a nominally Fe-based ASI [33], different ordering phases were accessed in the square ASI.

1.2 – Perovskite Oxides

While permalloy-based ASI systems have facilitated the investigation of magnetic frustration and dynamics in various array geometries, relatively less attention has been given to

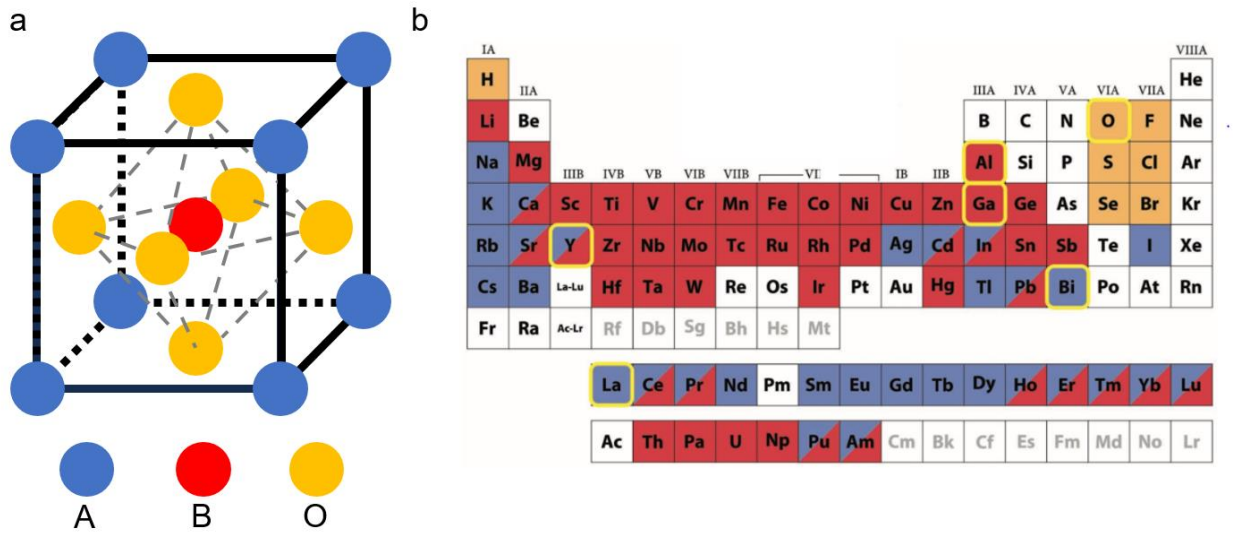

Figure 1.6: *(a) Schematic of the perovskite unit cell with chemical formula ABO_3. The blue, red, and orange balls correspond with the A-, B-, and O-site ions. The B-site cation is surrounded by an octahedra of oxygen anions, as illustrated by the dashed gray lines. (b) Periodic table color-coded based on which site on the unit cell can accommodate those elements [37].*

investigating how the nanoisland material properties influences the behavior of the ASI system. One material system which can facilitate such materials-focused studies are the perovskite oxides (a.k.a. complex oxides). This class of materials exhibit a wide range of behaviors including insulating and metallic states, antiferromagnetic and ferromagnetic states, and even ferroelectric or superconducting states [35,36]. Moreover, owing to a sensitive coupling between charge, lattice, orbital, and spin degrees of freedom; the properties of these complex oxides can be tuned using parameters such as substrate orientation, individual layer thickness, and epitaxial strain state [35,36].

Perovskite oxides have a typical chemical formula of ABO_3, where the *A*- and *B*-sites can accommodate a wide range of cations as shown on the periodic table in Figure 1.6 [37]. The

perovskite unit cell is structured such that, for an ideal cubic cell, the *B*-site cation (typically a transition metal element, red ball in Figure 1.6(a)) resides at the unit cell center and the *A*-site cation (typically a alkali or rare earth metal, blue ball in Figure 1.6(a)) sit at the primitive cubic lattice positions. The oxygen anions (orange balls in Figure 1.6(a)) sit at the face centers of the unit cell. For the general class of perovskite materials, the oxygen may be substituted with either a halogen or chalcogen. Henceforth, I will restrict our discussion to perovskite *oxides* which are the focus of this dissertation work. The ideal perovskite structure has cubic symmetry, which is the case for the perovskite $SrTiO_3$. However, the unit cell structure depends on the ionic radii of the constituent elements which are dependent on their valence, coordination, and spin state [38]. Predictions of the stable unit cell structure based solely off the ionic radii can be made by calculating Goldschmidt's tolerance factor, *t*, as

$$t = \frac{r_A + r_O}{\sqrt{2}(r_B + r_O)} \qquad \text{Eq. 1.2}$$

where r_A, r_B, and r_O are the ionic radii of the *A*-site, *B*-site, and oxygen ions, respectively [39]. The Goldschmidt tolerance factor is a ratio of two lengths along the unit cell and corresponds with the *A-O-A* (face-diagonal) and *O-B-O* (octahedral axis length) bonds. When $0.9 \leq t \leq 1$, the perovskite adopts a cubic structure. As *t* deviates further from 1, the crystal will adopt lower symmetry to stabilize structures with increasing ionic size mismatches. Specifically, structures with hexagonal symmetries are predicted if $t > 1$ and orthorhombic or rhombohedral symmetries if $0.7 \leq t < 0.9$. Below 0.7, the material is predicted to lose its perovskite structure.

1.2.1 – Crystal Field Splitting

The electronic and magnetic properties are intimately tied with the structure of the crystal and therefore the bonding between the different ions. In this dissertation work, the perovskite oxides *B*-site contain first row transition metals, whose *3d* orbitals bond with the *2p* orbitals of the

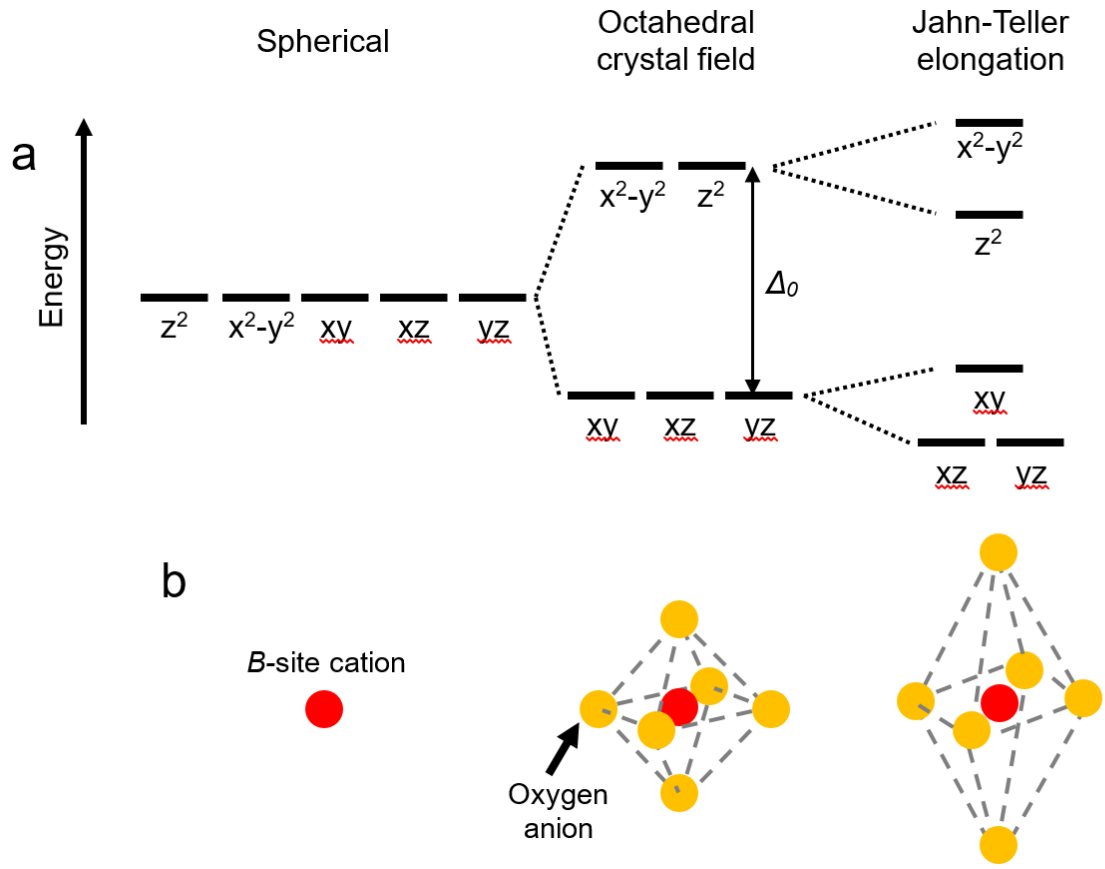

Figure 1.7: *(a) Schematic of the 3d orbital energy states for a B-site cation under a spherical field, octahedral crystal field, and Jahn-Teller tetragonal distortion. The crystal field splitting energy is represented by Δ_0. (b) Corresponding schematics of the ion placements for the different energy diagrams. The red and orange balls correspond with the B-site cation and oxygen anion in the perovskite unit cell in Figure 1.6. The gray dashed lines are used to illustrate the octahedron the oxygen anions form around the B-site cation and do not correspond with oxygen-oxygen bonds.*

oxygen anions. In the absence of other atoms, the *3d* orbitals shown are degenerate (i.e., the "spherical" case of Figure 1.7(a,b)). This behavior changes inside the perovskite structure, where the *B*-site cation is surrounded by an octahedra of oxygen anions (orange balls in Figure 1.7(b)). This effect can be understood through crystal field theory [40], which considers the electrostatic

repulsion between the electronic orbitals to explain the degeneracy (or lack thereof) between the *3d* orbitals. In other words, the *B*-site 3*d* orbitals which point towards the oxygen positions possess higher energies [41]. For the octahedrally-coordinated *B*-site cation, the d_z^2 and d_x^2-$_y^2$ orbitals (collectively referred to as "e_g" orbitals) are maximally oriented with the *O*-sites and thus have the highest energy as shown in Figure 1.7(a). In contrast, the other three orbitals have lower energies and are referred to as the t_{2g} orbitals. The energy difference between the t_{2g} and e_g orbitals is referred to as the crystal field stabilization energy (CFSE) Δ_0. In these energy-split orbitals, electrons will first fill the lowest energy level states based on Hund's rule of maximizing the amount of parallel spin states. The placement of additional electrons depends on the balance between CFSE and the energy penalty of pairing electrons in an orbital (i.e., Coulombic repulsion). In the case where the CFSE is weaker than the electron pairing energy, the additional electrons will occupy the higher energy orbital states with the same spin orientation as the lower energy states to form a "high spin" configuration. Conversely, if the CFSE is larger than the pairing energy, then the lower energy orbitals will all be occupied before filling the higher energy states, forming a "low spin" state.

Additional changes to the orbital energy levels can be induced through several other effects. Depending on the electron filling of the orbitals, the oxygen octahedra surrounding the *B*-site cation can undergo a spontaneous distortion through the Jahn-Teller (JT) effect (Figure 1.7(a,b)). The JT effect occurs if a system can lower its total energy by splitting the e_g and t_{2g} states into different energy levels. For this reason, JT distortion will not occur if there are no degeneracies between the different *d*-orbital electrons. For instance, in the case of the $3d^5$ electrons (i.e., 5 electrons in the 3*d* level), the t_{2g} and e_g levels will not undergo JT distortion if the electrons are in a high-spin configuration. However, the $3d^5$ electrons will undergo JT distortion of the electrons

are in a low-spin configuration. The energy levels of the orbitals can also be influenced by straining the material through, for instance, epitaxial growth which will be discussed later in this dissertation.

1.2.2 – Magnetism in Perovskite Oxides

The ferromagnetic behavior of a material depends on the manner in which the electron magnetic moments order in the material. Fundamentally, this behavior is driven by exchange interactions between electrons in the material [41]. The exchange interaction is a consequence of two different effects acting simultaneously. First, through Pauli's exclusion principle, electrons can only occupy the same orbital if they have antiparallel spins. That is, one "up" and one "down" spin electron can occupy the same orbital, but two electrons with the same spin cannot occupy that same orbital. Second, through Coulomb interactions, the electrons energetically prefer to maximize their spatial separation to minimize the electrostatic repulsion. That is, to minimize Coulomb repulsion, the electrons prefer to avoid occupying the same orbital. The simultaneous satisfaction of both Pauli's exclusion principle and Coulomb repulsion minimization results in the energetic preference to have parallel spin alignment (i.e., Hund's rules of electron filling in orbitals).

The origins of magnetic ordering in perovskite oxides are the indirect exchange mechanisms. Typically, in perovskite oxides, the *B*-site cations are magnetically active while the *A*-site cations possess a full valence shell (i.e., no net magnetic moment). In this situation, the magnetically-active cations, henceforth referred to as the *B*-site cations, interact with one another through indirect exchange interactions across *B*-*O*-*B* bonds, where *O* corresponds with the oxygen anion. This indirect mechanism is in contrast to direct exchange interactions which involves direct interaction between the electrons of the metal cations. For perovskite oxides, two types of indirect exchange interaction models are of importance: superexchange and double-exchange.

Superexchange results from a partial degree of covalent bonding between the *3d B*-cation and *2p* oxygen anion orbitals and satisfaction of Pauli's exclusion principle over the bonds [42–44]. The magnetic ordering which arises from superexchange can be predicted through the guiding principles established by Goodenough, Kanamori, and Anderson [43–46]. These principles, also known as the "GKA rules", illustrate how ferromagnetic and antiferromagnetic superexchange coupling depends on the cation orbital filling and whether the *B-O-B* bond angle is 180° or 90°. A concise statement of the GKA rules is provided in [43] and is summarized for the 180° *B-O-B* bond as follows: antiferromagnetic ordering is established between (1) two half-filled or (2) empty orbitals while (3) ferromagnetic ordering is established between one half-filled and one empty orbital. It is important to also note that the antiferromagnetic superexchange interactions of (1) and (2) are stronger than the ferromagnetic superexchange described by (2) [43,44].

An example of how the superexchange mechanism works across a 180° *B-O-B* bond is illustrated with Figure 1.8(a-c), which illustrates Cases 1-3 discussed above. To help guide the discussion, the two *B*-cations will be distinguished as B_1 and B_2. To simplify the discussion, the example shown in Figure 1.8 shows *3d* orbitals under a spherical field. However, the discussion can be further extended to octahedral fields. In all these cases, Pauli's exclusion principle must be obeyed, where the overlapping orbitals can only contain one up and one down spin electron. This scenario is exemplified in Case 1 shown in Figure 1.8(a), which can represent the case of the antiferromagnet $LaFeO_3$ [47], where both Fe^{3+} cations are in the high spin $3d^5$ state. If the left cation possess all down spins, then the B_1-*O* bond can only be established using an up spin from the oxygen *2p* orbital. This behavior leaves a remaining down spin in the oxygen orbital which can only be bonded to the B_2 *3d* orbitals if they all contain up spins, resulting in an antiferromagnetic

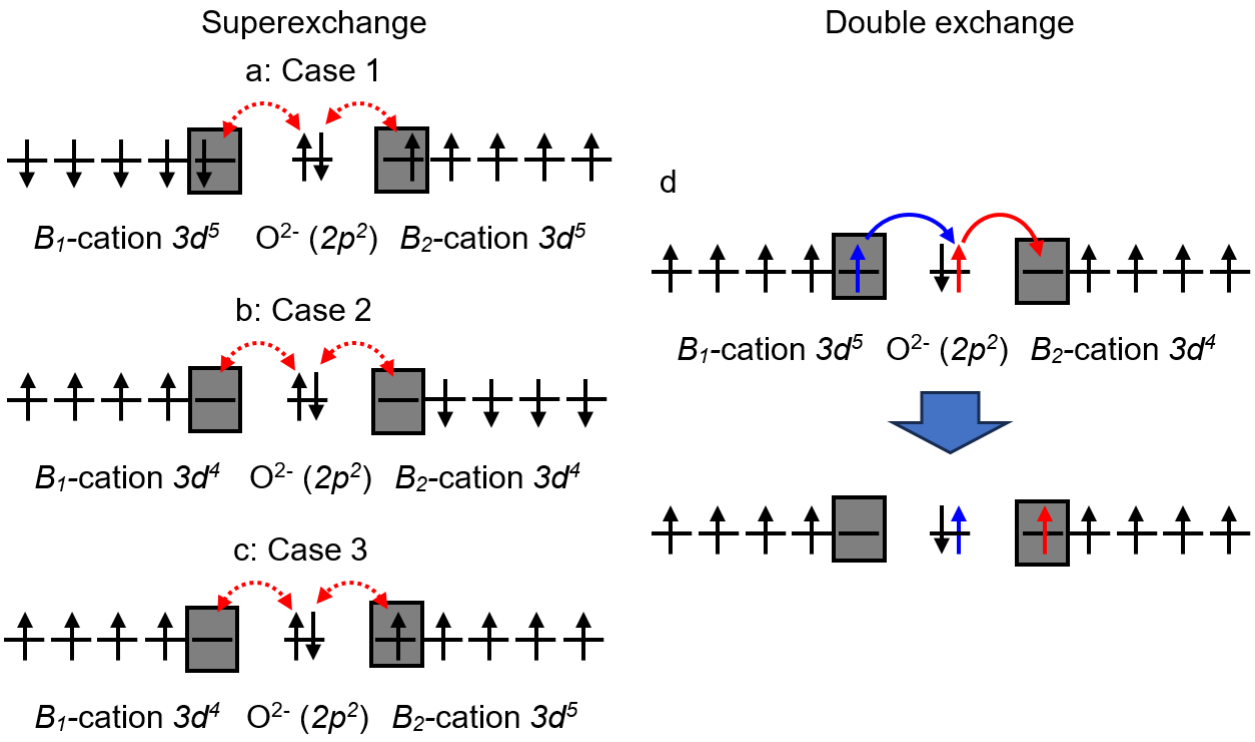

Figure 1.8: *(a-c) Schematic of the superexchange mechanism across a 180° B_1-O-B_2 bond for the cases when the bonding B-cation orbitals (a) are both half-filled, (b) have one empty orbital, or (c) have one that is half-filled and the other that is empty. These conditions correspond with Cases 1-3 in the text. (d) Schematic of the double exchange mechanism, where the different spins and their transfer are color coded based on the different ions they originated from. For all figures, the gray boxes serves to highlight the 3d orbital which participates in the B-O-B bond analyzed in these examples. For simplicity, the 3d orbitals are shown here to be under a spherical field.*

coupling between the B_1 and B_2 cations. In addition to Pauli's exclusion principle, the minimization of electrostatic interactions must also be considered (i.e., Hund's rules are applied).

In Case 2 (Figure 1.8(b)), the B_1 cation possesses four up spin electrons and one empty orbital and can represent the case of the antiferromagnet $LaMnO_3$ [48], where the Mn^{3+} ions are in a high spin $3d^4$ state. The oxygen in this situation can contributes its electron density either into

the filled or unfilled orbital states. However, it is energetically favorable for the donated electron to occupy the unfilled state to minimize electrostatic repulsion. Through the same logic, it is also energetically favorable for the contributed oxygen electron to have an up spin. This, again, leaves us with a remaining down spin oxygen electron available for bonding. Through the same principles discussed above, the resulting B_1-O-B_2 bond will have antiferromagnetic coupling between the cations.

Case 3 (Figure 1.8(c)) represents the situation where B_1 has an empty orbital with four up spin electrons while B_2 is half-filled. By applying the discussion of Case 2 to the B_1-O bond, we are left with a remaining down spin oxygen *2p* electron. If we apply the principles of Case 1 to the O-B_2 bond, we find that the B_2 valence electrons must be in the up spin state. Therefore, unlike the situations where B_1 and B_2 are of the same valence state (Case 1 and 2), the mixed valence Case 3 results in ferromagnetic ordering.

Ferromagnetism in the mixed valence situation can also give rise to metallicity. This situation can be explained through another indirect exchange interaction called double exchange. This mechanism, proposed by Zenner [49], has been used to explain the simultaneous presence of ferromagnetism and metallicity in the manganite perovskites [41,49]. In double exchange, the electrons use the oxygen anion to "hop" from one metal cation to another. Schematically this behavior is illustrated in Figure 1.8(d). The principle behind double exchange is that, for the oxygen cation to facilitate an electron transfer between the B_1 and B_2 cations, two electron exchanges (hence, double exchange) need to happen. Specifically, from Figure 1.8(d), an electron from the oxygen (red spin) would need to be transferred to the B_2 cation (red arrow) and an electron from the B_1 cation (blue spin) then needs to hop to the oxygen anion (blue arrow). Since spin flips

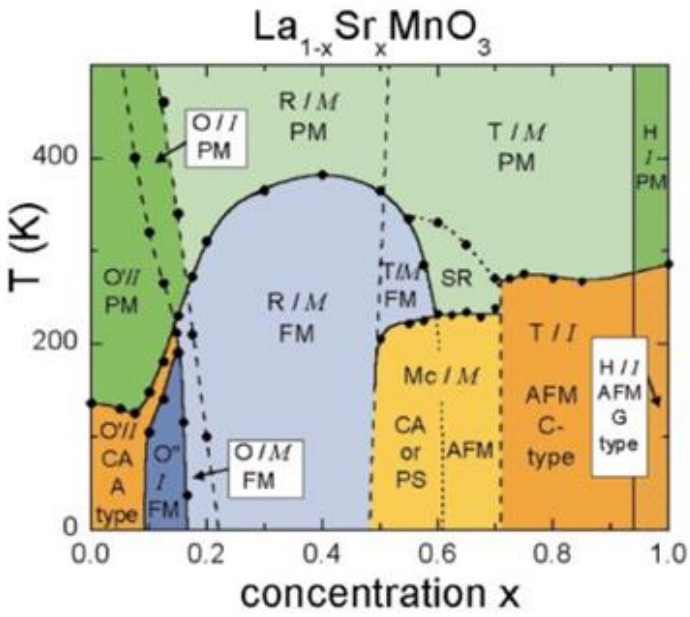

Figure 1.9: *Phase diagram of single-crystalline $La_{1-x}Sr_xMnO_3$ (LSMO) as a function of Sr-doping concentration, x, and temperature, T [48]. Information about the structural, magnetic, and electronic properties are given with the following symbols. Structure: O – orthorhombic, O' – Jahn-Teller distorted orthorhombic, O'' - orbital-ordered orthorhombic, R – rhombohedral, T – tetragonal, Mc – monoclinic, H – hexagonal. Electronic state: M – metallic, I – insulating. Magnetic ordering: FM – ferromagnetic, PM – paramagnetic, SR – short-ranged order, PS – phase separated, AFM – antiferromagnetic with A-, C-, or G-type moment ordering.*

are forbidden in this exchange process (i.e., both the red and blue spins are up), the electron transfer is energetically favorable only when the coupling between B_1 and B_2 are ferromagnetic (i.e., otherwise Hund's rules would be violated). A material system which exhibits this double exchange mechanism is the perovskite $La_{1-x}Sr_xMnO_3$ (LSMO), which will be discussed below.

1.2.3 – $La_{1-x}Sr_xMnO_3$ (LSMO)

$La_{1-x}Sr_xMnO_3$ is one member of the perovskite oxide family which exhibits a wide variety of structural, magnetic, and electronic phases as shown in Figure 1.9 [48]. LSMO is sometimes

referred to as Sr-doped $LaMnO_3$, where increasing the Sr concentration x increases the amount of Sr cations occupying the *A*-site perovskite unit cell which, in turn, decreases the overall concentration of La in the compound. One effect of the Sr doping is it creates a mixture of Mn^{3+} ($3d^4$) and Mn^{4+} ($3d^3$) cations to establish charge neutrality, as Sr and La has a nominal charge of 2+ and 3+, respectively. While the end members of LSMO, $LaMnO_3$ and $SrMnO_3$, are antiferromagnetic insulators, moderate Sr doping (i.e., $x = 0.3$) results in a ferromagnetic metallic state owing to an increasing dominance of the double exchange interaction. LSMO has received a wide attention owing to its unique properties, such as colossal magnetoresistance [50,51] and half-metallicity [52], which have potential applications in computing memory devices such as magnetic tunneling junctions [53,54]. As will be discussed in the later sections, this dissertation work focuses on lithographically patterned thin films (~ 40 nm thickness) of the metallic and ferromagnetic $La_{0.7}Sr_{0.3}MnO_3$ which has been extensively studied as a micro/nano-structured [23,55–60] system. Henceforth, any discussion of LSMO will specifically refer to $La_{0.7}Sr_{0.3}MnO_3$.

1.3 – Magnetic Domain Formation

The principles discussed in the previous section describes how ferromagnetic ordering can be established between two adjacent cations (i.e., atomic-scale ferromagnetic ordering). However, having ferromagnetic ordering on the atomic scale does not necessarily imply that uniform magnetization will be established across longer (e.g., bigger than nanometer) length scales. In many cases, a ferromagnetic body will contain regions called magnetic domains, within which the magnetic moments are uniformly magnetized. For micron- and nano-sized magnetic bodies, the different domains which appear within the volume may collectively be referred to as a domain with a specific name. Several examples of names used for these domains will be given below.

The formation of magnetic domains can be described using micromagnetics, which models the magnetic body and moment distribution as a continuum, along with an energetic theory of magnetic domain formation [61]. With these techniques the form of the magnetic domain may be predicted with knowledge of the magnetic material properties as well as the shape of the body. In micromagnetics, the system is modeled as a vector field of unit magnetizations directions $\boldsymbol{m} = \boldsymbol{M}/M_{sat}$, where $\boldsymbol{M}$ is the unnormalized magnetization and M_{sat} is the saturation magnetization. This section will cover several basic principles behind the formation of spin textures and the types of textures that appear.

1.3.1 – Magnetic Energies

The origin of magnetic domains can be understood through thermodynamic principles, where the lowest energy spin texture is one which simultaneously minimizes several energy terms representing different aspects of atomic-scale magnetic phenomena [61]. The exchange energy, E_{ex}, represents a fundamental property of ferromagnetic materials: adjacent magnetic moments prefer to align parallel with each other. Any deviations from parallel moment alignment incurs an energy penalty E_{ex}, which depends on the material property known as the exchange stiffness A_{ex}. E_{ex} is defined as

$$E_{ex} = A_{ex} \int (\nabla \boldsymbol{m})^2 \, dV \qquad \text{Eq. 1.3}$$

where V is the volume of the magnetic body.

The magnetocrystalline anisotropy energy, E_{mca}, describes the energetic preference for magnetic moments to preferentially align along certain crystallographic directions referred to as "easy" axes. E_{mca} penalizes any deviations from complete parallel alignment between the magnetic moments and the crystallographic easy axes, which depends on the magnetocrystalline anisotropy

constant of the material, K_1. Formally, E_{mca} can be defined for systems with cubic magnetocrystalline anisotropy (e.g., easy axes along ⟨100⟩ or ⟨111⟩ directions) as

$$E_{mca} = K_1 \int [(\boldsymbol{c}_1 \cdot \boldsymbol{m})^2(\boldsymbol{c}_2 \cdot \boldsymbol{m})^2 + (\boldsymbol{c}_1 \cdot \boldsymbol{m})^2(\boldsymbol{c}_3 \cdot \boldsymbol{m})^2 + (\boldsymbol{c}_2 \cdot \boldsymbol{m})^2(\boldsymbol{c}_3 \cdot \boldsymbol{m})^2] dV \qquad \text{Eq. 1.4}$$

where $\boldsymbol{c_1}$, $\boldsymbol{c_2}$, and $\boldsymbol{c_3}$ represents the orthogonal anisotropy directions [62]. For systems with cubic anisotropy, Eq. 1.4 can include higher order anisotropy terms with, for instance, constants K_2, K_3, and so forth. However, such terms are usually small and can be neglected [61,63].

The magnetostatic energy, E_{ms}, quantifies the cost for stray fields to exist in the system. These stray fields are produced by magnetic poles which are created at any regions where $\boldsymbol{M}$ diverges (i.e., $\text{div}(\boldsymbol{H_s}) = -\text{div}(\boldsymbol{M})$). E_{ms} is defined as

$$E_{ms} = -\frac{\mu_0 M_{sat}}{2} \int \boldsymbol{H_s} \cdot \boldsymbol{m}\, dV \qquad \text{Eq. 1.5}$$

E_{ms} reflects the production of long-range stray fields which depend on M_{sat}, the shape of the material, and how the material is locally magnetized throughout the material. E_{ms} depends on how multiple magnetic bodies interact with each other through the stray fields they produce (i.e., Eq. 1.1). I note that the convention used to describe the unit magnetization varies across the literature, where the symbol $\boldsymbol{m}$ may be associated with the unit magnetization (e.g., Eq. 1.5) or the magnetic moment (e.g., Eq. 1.1). In the subsequent chapters, the definition of $\boldsymbol{m}$ will be made explicit.

1.3.2 – Magnetic Domain Walls

When a system forms multiple magnetic domains (i.e., the red boxed regions in Figure 1.10) the individual domains are bordered by regions known as domain walls (i.e., the black boxed regions in Figure 1.10). Domain walls are regions where the magnetic ordering transitions between the magnetizations of the two domains they connect. While the orientations between two different domains can take on a wide range of angles, I will focus here on the case where the two domains (arrows outside the box in Figure 1.10 (a,b)) are oriented at 180° from each other. Thus, this type

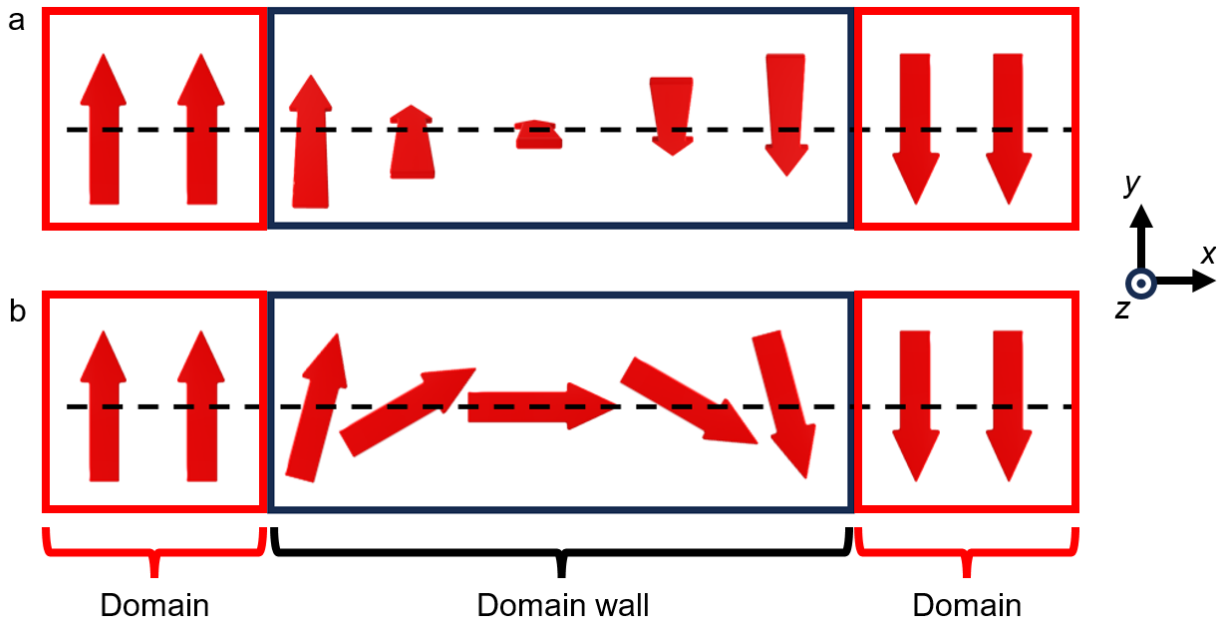

Figure 1.10: *(a,b) Schematics of two types of 180° domain walls: the (a) Bloch wall, where the moments rotate out of the x-y plane, and (b) Néel wall, where the moments rotate in the x-y plane.*

of wall is known as a 180° domain wall which is present in materials with uniaxial anisotropy. The principles discussed for the 180° domain wall can also be applied to other wall orientations, such as a 90° wall (connecting two perpendicular domains) can also be observed in materials with cubic anisotropy.

Domain walls are also named for the different modes used to gradually transition between two different domains. As shown in Figure 1.10(a), the moments can gradually transition between the two domain orientations by rotating about the x-axis within the y-z plane, producing what is known as a Bloch wall. The magnetic moments within the wall could also rotate about the z-axis within the x-y plane to produce what is known as a Néel wall.

While the creation of domain walls can reduce the total energy of the system by allowing multiple domains to form in energetically optimal configurations, energetic penalties also exists for creating these walls which influences their equilibrium widths (i.e., length over which gradual

moment rotation can occur). E_{ex} motivates the system to maximize the width of the domain wall to minimize the extent of misalignment between the adjacent magnetic moments. Conversely, E_{mca} prefers the formation of narrow domain walls which, in turn, minimizes the amount of moments that are not aligned with the easy axes. Additionally, E_{ms} can influence the formation of either Bloch or Néel walls. If the width of the domain wall is comparable to the dimensions of the ferromagnetic body, then the presence of a Bloch domain wall would produce magnetic poles at the surface (i.e., have moments pointing normal to the sample surface). In contrast, the moments within a Néel wall can minimize the amount of surface magnetic poles produced through its in-plane rotation. The width and type of domain wall present depends on the balance of the aforementioned energy terms. Bloch domain walls can be favored in bulk systems while Néel walls may be favored in thin film systems. Since domain walls are continuous transitions between two regions, there exists no unique definition of the domain wall width. Various methods of defining the widths of different wall types have been developed and can be related to the magnetic material properties of the system [61]. Regardless of the exact domain wall definition used, the equilibrium size and appearance of the domain wall reflects a magnetization configuration capable of minimizing the total energy of the system.

1.3.3 – Spin Textures

Domain patterns within micro- or nano-structured magnetic bodies (e.g., produced through lithography) may be collectively referred to as a type of domain or a spin texture. Investigations into the spin textures of micro- and nano-patterned materials has been motivated by their potential to serve as the foundation for spin-based information storage and processing [10,64–69]. In the context of ASIs, the ability to engineer different spin texture is of utmost importance in realizing physical systems which can be modeled within an Ising framework. Thus, in order to exploit the

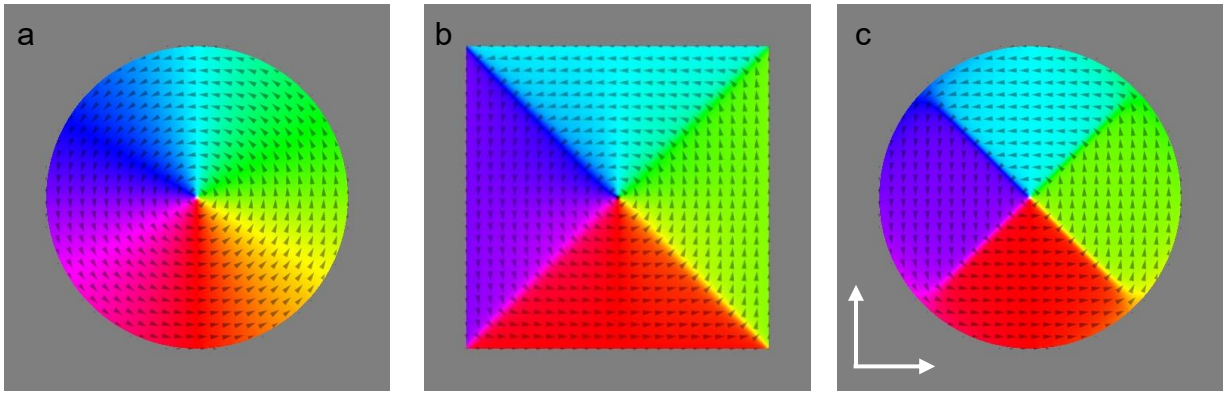

Figure 1.11: *(a-b)Magnetization maps of a (a) 2 μm diameter disk and (b) 2 μm wide square with 40 nm thicknesses. Spin textures were simulated with MuMax[3] [62] using M_{sat} = 390 kA/m and A_{ex} = 3.6 pJ/m (i.e., LSMO properties at 115 K from Ref. [58]). K_1 was set to 0 kJ/m^3. (c) Same as (a) but simulated using K_1 = 10 kJ/m^3. Arrows within the shape indicate the orientation of the local magnetization. The white arrows in (c) indicate the easy axes of the magnetocrystalline anisotropy.*

properties of different spin textures for research or applications purposes, a thorough understanding of how spin textures can be engineered is required. The experimental and theoretical methods which can be used to understand spin texture formation are discussed in Chapter 2.

As discussed in Section 1.3.1, the appearance of a spin texture in a demagnetized system (i.e., no field-dependent history) reflects the ability of that magnetic body to simultaneously minimize several energetic terms to achieve that (meta)stable state. Figure 1.11 shows two types of spin textures which have been commonly observed in lithographically-patterned ferromagnetic thin films: the vortex state in disk-shaped microstructures (i.e., Figure 1.11(a)) and the Landau state in square-shaped microstructures (i.e., Figure 1.11(b)). The details of how Figure 1.11 was simulated is discussed in Section 2.7. The appearance of these two structures can be understood from the standpoint of E_{ms} minimization: By maximizing the amount of moments having tangential orientation with the perimeter, the amount of magnetic poles formed is minimized in comparison

to a disk with uniform magnetization. For this reason, the vortex and Landau spin textures are also referred to as "flux-closure" domains. The formation of such domains does incur an E_{ex} penalty (i.e., the moments are not maximally aligned). In particular, the core of these structures experience a large degree of moment misalignment and tend to point out of the disk plane in an attempt to minimize the local E_{ex}. However, the total E_{ex} penalty of forming a flux-closure domain over a uniform magnetization may be offset by the associated reduction in E_{ms}. The out-of-plane orientation of the core is referred to as the polarity, while the direction of magnetization rotation in the vortex/Landau spin textures are referred to as the chirality.

The vortex and Landau spin textures have subtle differences in that the magnetization in a vortex spin texture (Figure 1.11(a)) smoothly vary over the magnetic body. Conversely, a Landau spin texture contains four uniformly magnetized domains which are separated by 90° domain walls (Figure 1.11(b,c)). If we consider the disk-shaped structure in Figure 1.11, then the observation of a vortex state (Figure 1.11(a)) implies that the magnetocrystalline anisotropy is negligible. Conversely, if the magnetocrystalline anisotropy is not negligible, then a Landau spin texture forms to maximize the alignment of moments with the easy axes *while* minimizing stray field production and, thus, E_{ms}.

If we return to the square micromagnet in Figure 1.11(b), we find that a Landau spin texture will form if the magnetocrystalline anisotropy is negligible (i.e., $K_1 \sim 0$ kJ/m^3). In contrast, an identically-sized disk-shaped micromagnet with negligible magnetocrystalline anisotropy (Figure 1.11(a)) will prefer to form a vortex spin texture rather than a Landau state. This behavior results from the sensitivity of E_{ms} to the *shape* of the magnetic body which, for a given type of spin texture, can alter the extent of magnetic poles produced. In other words, there exists a "shape anisotropy"

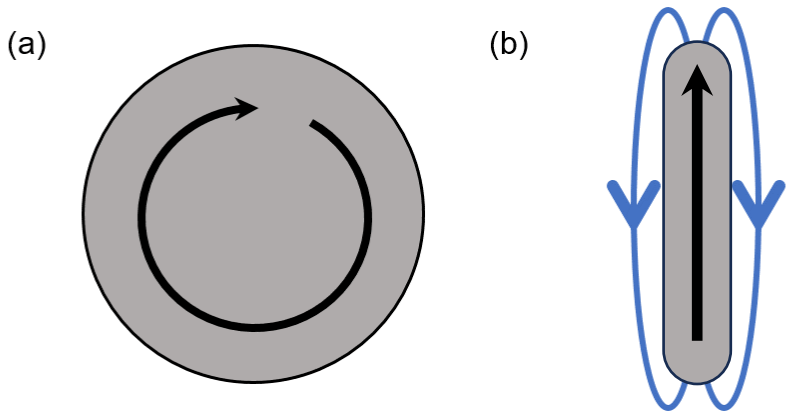

Figure 1.12: *(a,b) Schematic examples of the optimal spin texture state (black arrow) in micron-sized (a) disk and (b) stadium (i.e., rectangle with circular end caps) geometries. Blue arrows indicate stray field production. The diameter of the disk in (a) is identical to the length of the stadium in (b).*

which, through E_{ms}, penalizes domain formations which do not minimize the stray field production for the specific geometry being studied.

Shape anisotropy can also be observed when the aspect ratio of a magnetic body is altered. A detailed discussion about this form of shape anisotropy is provided in Chapters 3 and 4, but, for clarity, I will briefly discuss some of the key points here. Consider, for instance, the disk- and stadium-shaped micromagnets shown in Figure 1.12(a) and (b), respectively. As discussed earlier, the disk geometry may energetically prefer to form a vortex spin texture state. However, if the width of the disk is reduced to form a stadium shape (Figure 1.12(b)), it may become energetically preferable to form a single domain state magnetized along the stadium length. This form of shape anisotropy reflects the minimization of both E_{ms} and E_{ex} since, for an arbitrary spin texture, both parameters depend on the micro/nanomagnet aspect ratio (see Figure 4.2 in Chapter 4). In ASI systems, the nanoislands are deliberately designed to possess elongated structures (e.g., Figure 1.12(b)) so that only single domain states form.

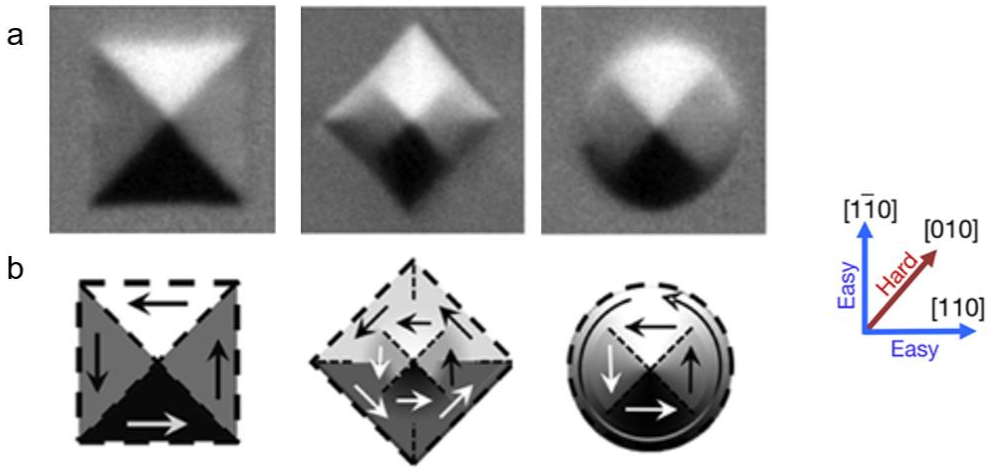

Figure 1.13: *(a) Magnetic domain contrast images of 2 μm square, diamond, and circle microstructures patterned into LSMO thin films measured at 32 K using x-ray photoemission electron microscopy. The LSMO film was 40 nm thick and was deposited on (001) Nb:$SrTiO_3$. (b) Schematics of the magnetization configuration in (a). Legend on the far right indicates the easy axes of the LSMO film. Adapted from Ref. [58]. Copyright 2016, American Chemical Society.*

So far, the examples discussed for the micromagnets examined cases where the material property is homogeneous throughout the material. However, spatial variations in the magnetic properties can give rise to interesting spin texture formation. Figure 1.13 shows several spin textures observed in 40 nm LSMO thin films patterned into micromagnets using an Ar-implantation-based patterning technique [58,59] which will be discussed in Section 2.2. In these structures, it was observed that multiple concentric domain types can exist. For instance, the diamond micromagnet possesses two concentric Landau spin textures, where the inner Landau pattern has domains aligned with the LSMO easy axes while the magnetizations of the outer Landau pattern are parallel with the micromagnet edges. Similarly, in the disk micromagnet, the inner spin texture is a Landau pattern while the outer spin texture resembles a vortex. This domain formation was explained by modeling the radial variation of K_1 with a sigmoid function, where K_1 vanished ~300 nm away from the micromagnet edges. This spatially-varying magnetocrystalline

anisotropy was hypothesized to originate from the patterning process used to create the LSMO micromagnets. The nonmagnetic matrix regions surrounding the micromagnets swells during an Ar-flood-implantation processing step, leading to an altered the strain state near the micromagnet/matrix interface and a local modification of K_1 which is strain-dependent in LSMO [58].

1.4 – Outlook

Understanding how spin textures form in patterned magnetic thin films is a complex problem requiring the simultaneous consideration of different magnetic effects which depend on the material properties, geometry, and magnetization state. As a consequence, prediction of the equilibrium spin texture state in isolated nanomagnets with an arbitrary combination of material and geometric properties can be a complex problem requiring a combination of experimental imaging and theoretical analysis. Moreover, systems such as ASIs are composed of interacting nanoislands, where the total energy of the system exhibits an additional dependence on the magnetostatic coupling between each nanoisland. However, the nanomagnets in such systems are engineered to possess specific spin texture states (e.g., only single domains). In other words, the nanoislands are designed so that domain formation is dominated by the *intra*island energetics while the *inter*island magnetostatic (i.e., dipolar) interactions plays a negligible role.

This dissertation uses ASIs fabricated from LSMO as a model system to investigate how the interaction between magnetostatically-coupled magnetic nanostructures can compete against the internal magnetic influences in each nanostructure to form complex spin textures. Chapter 2 discusses the experimental and computational methodologies used to fabricate and simulate the behavior of LSMO-based ASIs. Chapter 3 investigates ASIs fabricated from LSMO, where an ASI-geometry-dependent formation of single domain and vortex states were observed. Through an

experimental and simulation study, it was found that the spin textures observed in these systems arise from a competition between the *intra*- and *inter*-island effects which are enabled by the unique combination of magnetic properties in LSMO. The *inter*-island interaction depends on both the ASI geometry, as discussed in Chapter 3, as well as the magnetization configuration of each nanoisland, as discussed in Chapter 4. Chapter 5 investigates the relaxation kinetics of ASIs capable of stabilizing single domain and vortex states. The conclusions of this dissertation are discussed in Chapter 6, along with potential future work to further our understanding of these systems.

Chapter 2: Experimental and Computational Techniques

The experimental efforts of this dissertation depended on the production of perovskite thin films of high structural and magnetic quality, the patterning of those films into nanoscale structures, and the use of elementally- and magnetically-sensitive spectroscopy and microscopy techniques to study their physics. This chapter provides a summary of all the fabrication and analytical technique used in this dissertation. Thin film perovskite samples were grown using pulsed laser deposition and subsequently patterned into micro- and nanostructures with an ion-implantation based technique. Prior to patterning, the structural quality of the samples were characterized using x-ray reflectometry and diffraction, while the bulk magnetic properties were studied using vibrating sample magnetometry. Soft x-ray spectroscopy and microscopy were used to perform element and time-resolved studies of magnetic ordering in pristine and patterned samples. Micromagnetic simulations were performed to interpret the magnetizations of imaged magnetic domains and understand their energetics.

2.1 – Fabrication

2.1.1 – Epitaxial Film Growth

The term “thin film” generally refers to a layer of material with thicknesses in the nanometer to micron range. For this dissertation work, I will focus on single crystal thin films whose in-plane crystal structure matches that of the single crystal substrate the film is grown on. These types of films are referred to as being epitaxial, pseudomorphic, or coherent; which will be henceforth referred to as epitaxial thin films. The ability to grow epitaxial thin films depends on a number of different factors that are intrinsic to the materials used, interfaces formed, and deposition techniques used. This section will focus on the first two factors and discuss the third in Section 2.1.2.

For epitaxial growth, the substrate and target material (i.e., the thin film to be grown) should share similar crystalline structures. Increasing the extent of structural dissimilarity (e.g., increasing the lattice parameter mismatch) increases the likelihood of forming misfit dislocations or other defects, thus reducing the crystalline quality. Quantitively, this lattice mismatch can be described by the epitaxial strain ϵ experienced by a thin film

$$\epsilon = \frac{a_s - a_f}{a_s} \quad \text{Eq. 2.1}$$

where a_s and a_f are the bulk lattice parameters of the substrate and film, respectively. If the magnitude of ϵ is below a few percent, then the film can be grown epitaxially. In addition to mismatches between a_s and a_f, the likelihood of forming misfit dislocations also increases with the film thickness, where the material gradually relaxes back into its bulk structure [70].

When performing epitaxial growth, different growth modes can take place depending on the balance of the interfacial energies between the film material, substrate, and the growth chamber atmosphere. During physical vapor deposition, the vaporized target material adsorbs onto the substrate surface. The adatoms diffuse across the surface and aggregate to form clusters. The types of clusters formed depends on the balance between the energies of the substrate-atmosphere ($\gamma_{s\text{-}a}$), film-atmosphere ($\gamma_{f\text{-}a}$), and substrate-film ($\gamma_{s\text{-}f}$) interfaces. By modeling the film as a droplet, the energetic balance can be described using Young's equation

$$\gamma_{f-a} \cos\theta + \gamma_{s-f} = \gamma_{s-a} \quad \text{Eq. 2.2}$$

where θ is the contact angle the droplet forms on the substrate. How well the film material wets the surface (i.e., the value of θ) is influenced by the balance of interfacial energies. In the case where $\theta = 0°$, the film adatoms completely wets the substrate surface (i.e., spreads evenly over the surface), enabling either layer-by-layer of step-flow growth mode [71]. These two growth modes involves having individual monolayers grown in succession and is ideal for growing epitaxial thin

films. The monolayer in the layer-by-layer mode result from the growth of 2D islands of adatoms which eventually merge into a single monolayer. In step-flow mode, the monolayer may nucleate at the steps between the atomic planes formed by substrates which are not perfectly flat. Epitaxial growth of the film then proceeds by having the growth front flow away from the step. If $\theta > 0°$, the adatoms tend to cluster into islands, resulting in a three-dimensional island growth mode. The final growth mode, called Stranski-Krastanov growth, involves a layer-by-layer growth near the substrate surface, followed by an island growth mode beyond a critical thickness. The onset of island growth is determined by epitaxial strain in the film.

2.1.2 – Pulsed Laser Deposition

Pulsed laser deposition (PLD) is a laser-based physical vapor deposition technique used for the epitaxial growth of heterostructures with complex compositions and well-controlled interfaces. With optimized growth conditions, PLD offers the ability to perform stoichiometric transfer of elements from a target material to a substrate surface, growing an epitaxial film whose thickness can be controlled with atomic level precision.

In PLD, an excimer laser beam is focused on a target surface inside a vacuum chamber and ablates the target surface, forming a vapor. A plasma plume is formed as the vaporized material absorbs the remaining laser energy. The plasma plume then propagates towards the substrate where the material is deposited on. During deposition, multiple laser shots are fired at varying repetition rates as both the substrate holder and target holders are rotated. Rotation of the substrate holder facilitates uniform film deposition across the substrate while target rotation ensures uniform wear of the target surface.

The deposition of high quality epitaxial thin films requires tuning several interrelated growth parameters through a systematic trial-and-error process. The laser energy density, known

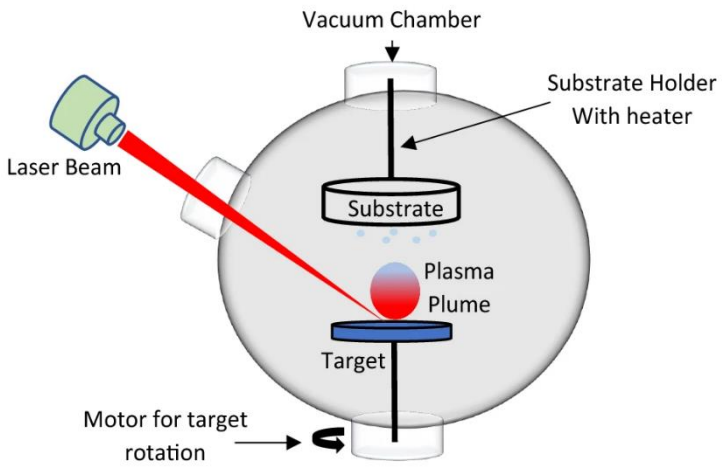

Figure 2.1: *Schematic of a PLD deposition system [148].*

as the fluence, plays a crucial role in determining the nature of material transfer from the target to the substrate. If the fluence is too low, the deposition process will be partial pressure driven which prevents the stoichiometric transfer of material. However, increasing the fluence also increases the risk of particle emission from the target, which may become embedded in the film and thus reduce its quality. For LSMO films, a fluence of ~1 J/cm^2 were found to yield thin films with structural and magnetic qualities consistent with the literature. The repetition rate of the laser can also control the structural quality of the thin film as higher repetition rates were reported to produce smoother films.

The substrate temperature can be controlled to tune surface diffusion of adsorbed atoms arriving from the laser plasma plume. An ideal substrate temperature will allow deposited ions to readily diffuse across the surface to facilitate a layer-by-layer growth mode that is ideal for growing epitaxial thin films. Surface diffusion of the adsorbed ions will be reduced by lowering the temperature, leading to an increased likelihood of growing polycrystalline or amorphous films. However, if the substrate is too hot, a risk of interdiffusion between the substrate and the deposited ions and/or grown thin film exists.

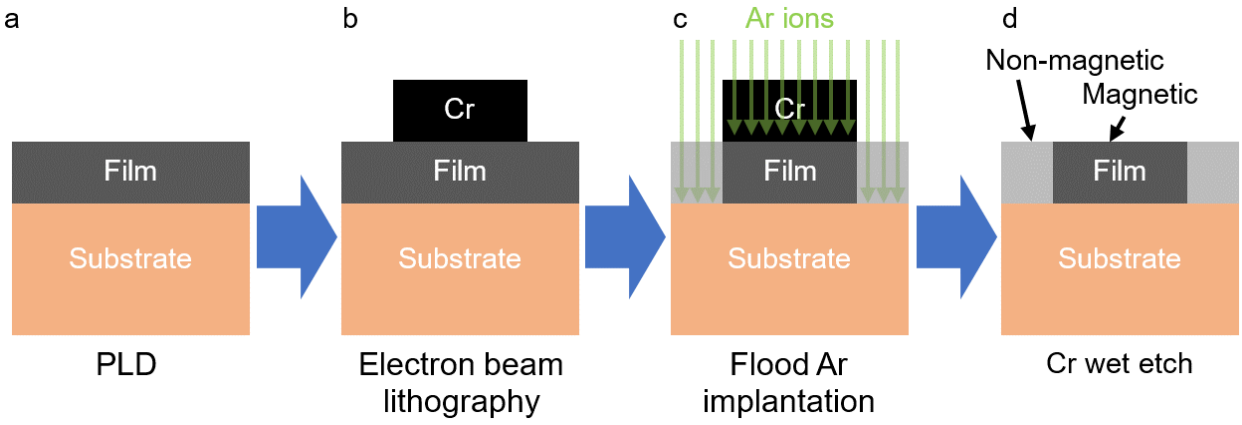

Figure 2.2: *Schematic of the Ar implantation based patterning process for perovskite thin films. (a) The perovskite thin film is grown using PLD. (b) A Cr hard mask is produced directly on top of the thin film using electron beam lithography and lift off. (c) The entire sample is subject to a flood Ar ion implantation, where regions not covered by the Cr hard mask are directly exposed to the ion flux. (d) The Cr mask is stripped using an acid wet etch, exposing the protected magnetic perovskite film which is surrounded by the Ar-ion-exposed film which have been rendered amorphous and non-magnetic.*

The pressure and gaseous species in the vacuum chamber also influences the thin film growth. For oxide films, the chamber may contain ~300 mTorr of O_2 during deposition to prevent the formation of oxygen vacancies. The presence of O_2 also reduces the kinetic energy of the plasma species traveling towards the substrate and reduce the damage of the substrate surface through ion bombardment. Moreover, post deposition, the sample may be annealed in a higher pressure of O_2 to eliminate oxygen vacancies.

2.2 – Nanoscale Patterning of Perovskite Oxides

Epitaxial perovskite oxide thin films are patterned into lithographically-defined nanostructures using an Ar-ion-implantation-based technique developed by Takamura *et al.* [59]. An overview of the patterning process will be provided here and is schematically shown in Figure

2.2. The patterning process of a PLD-grown oxide sample (Figure 2.2(a)) starts with spin-coating a positive tone resist on the sample and using electron beam lithography to define patterns into the resist. The resist is developed (i.e., the regions exposed to the electron beam are selectively washed away in a solution) followed by the deposition of ~70 nm thick Cr layer over the sample surface using thermal evaporation. Any Cr deposited on top of the resist is then removed using a lift-off cleaning step, leaving behind a Cr hard mask with the patterns originally defined through electron beam lithography as shown in Figure 2.2(b). This sample is then subject to flood Ar implantation with a dose of 10^{15} Ar/cm^2 and an energy of 50 keV (Figure 2.2(c)), which renders any exposed perovskite oxide film to be amorphous and non-magnetic (light gray regions in Figure 2.2(c,d)). All regions that are covered by the Cr hard mask are protected from the ion implantation (dark gray region in Figure 2.2(c,d)), where the Cr layer thickness is chosen to prevent Ar ion penetration into the oxide thin film. Finally, the Cr hard mask is removed using an acetic-acid-based wet etch. The specific values of the Cr mask thickness and the implantation energy used here are optimized for a ~40 nm thick film.

The resolution of this patterning process is primarily limited by the ion implantation process. During this process, the ions entering the sample collide with the atoms in the material, leading to multiple changes in the ion trajectory known as straggle. Overall, this straggle causes a columnated ion beam to produce an irradiation profile in the material that resembles a bulb-shape rather than a cylindrical column. Consequently, material under the Cr hard mask can get damaged by the incoming Ar ions. To predict the extent of straggle and ion-matter interaction, simulations can be performed using a package called Stopping and Range of Ions in Matter (SRIM) [72]. From Lee [73], it is predicted that implantation-induced defects propagate ~35 nm beneath the Cr mask for a 40 nm thick film. However, the resolution (i.e., lateral defect propagation) can be improved

by using lower implantation energies. SRIM can also be used to determine the optimal Cr mask thickness and implantation energies for films of varying thicknesses.

2.3 – Magnetic Characterization with Vibrating Sample Magnetometry

Vibrating sample magnetometry (VSM) is a technique that can characterize the magnetic properties of a material. The basic operating principle behind a VSM is that the net magnetic moment of a sample, m, can be measured by vibrating it with respect to a set of pick up coils. This vibration causes the coils to experience a time-varying magnetic flux (i.e., produced by the net sample moment) which induces a time-varying current to oppose the sample-produced magnetic flux (i.e., Lenz's Law) at the same frequency as the sample vibration. While the VSM measures the m of a sample, a more useful quantity to report is the magnetization M of the sample, which quantifies the moment *density* of a sample (i.e., m divided by the volume of the magnetic material). It is important to note that m, and thus M, reflects both the amount of moments present as well as their alignment. Thus, for a given material, m (and thus M) can possess different values depending on the history of the sample. The volume of a magnetic thin film can be determined with knowledge of the film thickness, which can be measured with x-ray reflectivity as discussed later, and the film area, which can be extracted through image analysis of a picture of a sample on top of grid paper. Henceforth, I will focus our discussion on M rather than m.

Two types of magnetometry measurements are typically performed with VSM systems. M, of a sample can be measured as a function of an applied magnetic field, H (a.k.a., M vs. H or hysteresis loops). These hysteresis loops contain quantities such as the saturation magnetization (M_{sat}, M associated with maximum moment alignment), remanent magnetization (M_r, largest value of M with $H = 0$ T), and the coercivity (H_c, the minimum H required to switch M from a net positive direction to a net negative, or vice versa). In addition, M can also be measured as a function of

temperature T (a.k.a., M vs. T). This measurement allows for the detection of the temperature-dependent transition at the Curie point T_C between a paramagnetic state to a magnetically-ordered state. In these measurements, a small static H field, usually on the order of magnitude of H_c of the material, is applied during the measurement. From an M vs T measurement, the first derivative of the measurement, dM/dT vs T, can be calculated and T_c can be assigned at the minima of the dM/dT vs T curve. The shape of an M vs T measurement depends on the strength of the H field chosen; the larger the H field, the more smoothed out the phase transition appears in the M vs T measurement. Thus, at larger H fields, the dM/dT vs T valley becomes shallow and broadened, leading to difficulties in confidently assigning T_c.

2.4 – Thin Film X-Ray Structural Characterization

2.4.1 – Instrumentation

X-rays serve as powerful non-destructive probes to characterize the properties of bulk and thin film materials. In modern laboratories, the structural properties of materials are studied using x-ray diffraction (XRD) systems. XRD systems can extract information about the structural property of a sample by using techniques based on the elastic scattering of x-rays (i.e., no photon energy loss) off of electrons surrounding the atoms of a material. These techniques will be discussed in the subsequent sections. XRD systems generally consist of an x-ray source, a detector, x-ray optics, and sample holder as shown in Figure 2.3. These components are mounted on a goniometer to facilitate several of the measurement techniques discussed in the following sections.

This dissertation work uses a Bruker D8 Discover diffractometer that has been configured for thin film measurements. The x-rays in the instrument is produced by a copper anode which produces a divergent x-ray beam comprised of, in Siegbahn notation, Cu $K_{\alpha 1}$, $K_{\alpha 2}$, and K_{β} photon energies (or, equivalently, wavelengths). The wavelengths of these emission lines (~8 keV) are

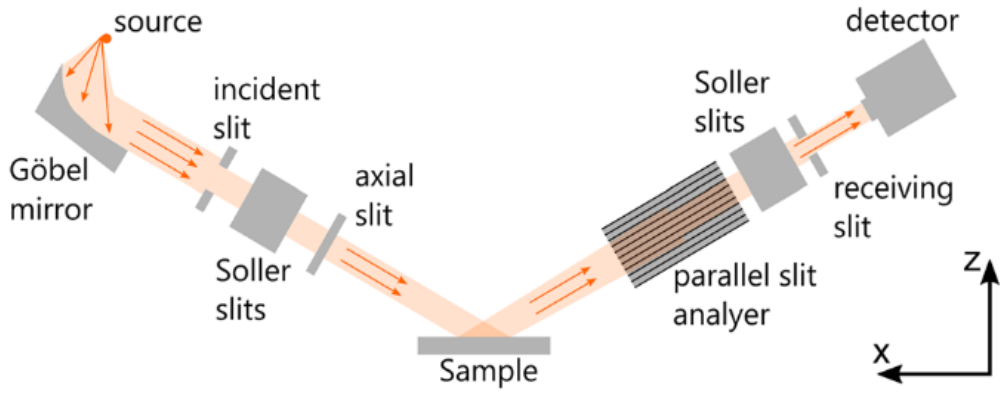

Figure 2.3: *Schematic of a thin film x-ray diffractometer setup [149]. Parallel slit analyzers were not used in this dissertation.*

described as "hard" x-rays (i.e, $h\nu > 2$ keV). The divergent x-rays are then "conditioned" into a highly collimated and monochromatic beam using several x-ray optics. The first optic the x-rays encounter is a parabolic multilayered mirror known as a Goebel mirror. This component is situated such that the x-ray source is located at the focal point of the parabolic mirror. The Goebel mirror collimates the x-ray beam while also suppressing the Cu K_β line [74]. The outgoing beam can be used to perform x-ray reflectometry measurements as discussed in the following section. For high (angular) resolution x-ray diffraction experiments, the beam ideally should consist of a single wavelength. Highly monochromated x-rays can be obtained by using optics fabricated from single crystals of Ge (220) to selectively allow the different wavelengths to reach the sample. These components are also known as "2-bounce" crystals as they are fabricated with a single channel cut in the crystal to allow the x-ray beam to bounce twice inside the optic. The now conditioned beam then illuminates the sample in the center of the goniometer which can then be directed towards the x-ray detector. Prior to entering the detector, the x-rays pass through an automated attenuator to protect the detector from oversaturation-induced damage. The Bruker D8 Discover uses a four-circle goniometer, where both the sample (θ) and detector (2θ) can rotate about the same axis. The

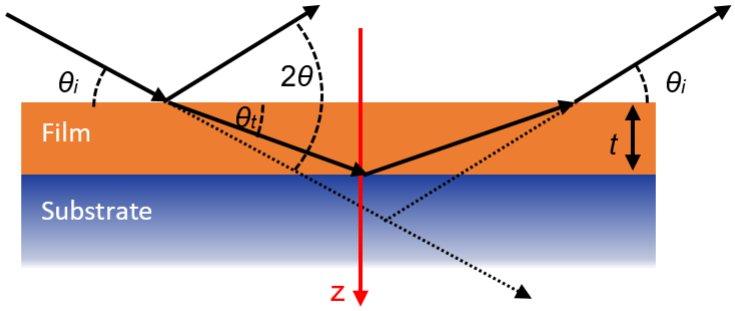

Figure 2.4: *Schematic of the XRR measurement geometry*

sample can rotate about three orthogonal axes, which include the ω rotation axis and two additional angles referred to as χ and ϕ.

2.4.2 – X-Ray Reflectometry (XRR)

X-ray reflectometry (XRR) is a technique which involves operating the x-ray source and detector at grazing angles (~ 0.3° – 10°) to characterize the thickness, roughness, and density of thin films and layers in heterostructures [74]. Measurements in XRR are performed using a θ/θ (moving detector and x-ray source) or θ/2θ (moving sample and detector) geometry, where the detector is at twice the angle of x-rays incident on the sample. The θ/θ and θ/2θ scans share identical diffraction geometries, but the former involves moving the x-ray source and detector about a stationary sample while the latter uses a stationary x-ray source and moves both the sample and detector. The XRR measurement geometry is shown in Figure 2.4. An example XRR curve measured from an LSMO single layer film deposited on a (001)-oriented STO substrate is shown in Figure 2.5.

The different features present in an XRR measurement (e.g., Figure 2.5) provide information about the thin film composition and morphology. The angle associated with the maximum measured intensity (around 0.4°) is known as the critical angle, θ_c. At this angle, total

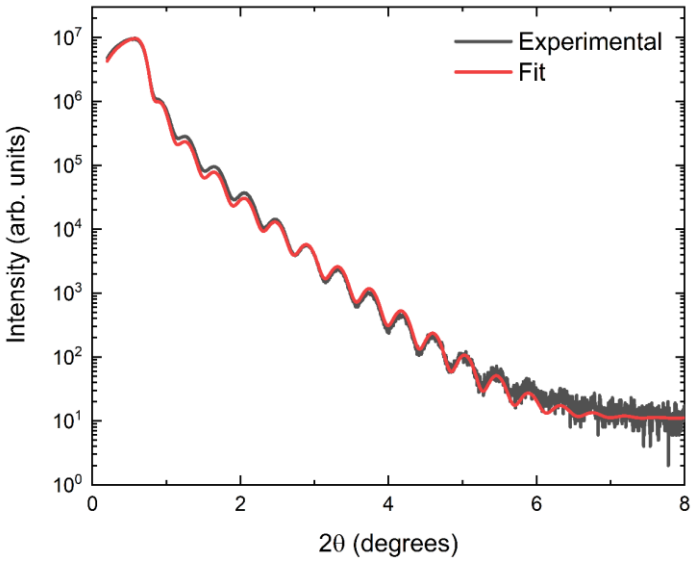

Figure 2.5: *Example XRR experimental data (gray line) and GenX fit (red line) of a 20 nm LSMO film deposited on a (001)-oriented STO substrate.*

external reflection of the x-ray beam occurs and can be theoretically determined from Snell's law as:

$$n_f \cos\theta_t = n_0 \cos\theta_i \qquad \text{Eq. 2.3}$$

where n_f and n_0 represent the refractive indices of the film and air, respectively, while θi and θ_t represent the incident and transmitted x-ray beam angles, respectively. The refractive index is a complex function with the form

$$n = 1 - \delta - i\beta \qquad \text{Eq. 2.4}$$

where i is the imaginary number with real (δ) and imaginary (β) component representing the transmission and absorption of light, respectively. For x-rays, the refractive index is always less than 1, which results in the refracted x-rays bending away from the sample normal (i.e., "z" in Figure 2.4). Assuming that the sample negligibly absorbs x-rays (i.e., $\beta \approx 0$) and applying the small angle approximation (i.e., $\cos\theta \approx 1 - \theta^2/2$) , Eq. 2.3 can be rewritten as

$$\theta_t = \sqrt{\theta_i^2 - 2\delta} \qquad \text{Eq. 2.5}$$

Given that the total reflection of the x-rays occur while $\theta_i^2 \geq 2\delta$ (i.e., θ_t is either zero or imaginary) [74], the critical angle (i.e., $\theta_i = \theta_c$) can be related to the refractive index, and thus the material properties, as

$$\theta_c = \sqrt{2\delta} \qquad \text{Eq. 2.6}$$

The critical angle serves as a fingerprint of the film density as the refractive index is related to the electron density.

As 2θ increases past θ_c, XRR curves can exhibit oscillating curves which decay by several orders of magnitude towards the background noise level. These oscillations, known as Kiessig fringes [75], contain additional information about the thin film density as the oscillation amplitudes depend on the density contrast between the different layers. The oscillation periodicity is inversely related to the layer thickness and arises from interference caused by path length differences between x-rays reflected from different surfaces and interfaces of the thin film system. How sharply the curve decays with increasing 2θ depends on the sample surface or interface roughness. For an ideally-flat surface, the intensity decays with the inverse fourth power of the scattering vector $Q = 4\pi\sin(\theta)/\lambda$, known as Porod's law [74]. As the film surface and interface roughness increases, the degree of diffuse scattering increases leading to a faster decay of the XRR signal. In practice, fitting software such as GenX [76] can be used to automatically fit sample parameters from experimental data such as the density, thickness, and roughness of the film and substrate. Figure 2.5 shows a curve fitted by GenX (red curve) to the experimental data (gray curve).

2.4.3 – High-Resolution X-Ray Diffraction (HRXRD)

XRD is another x-ray-based structural characterization technique which enables the quantitative characterization of the atomic ordering (i.e., crystallinity) in a material. The basic idea

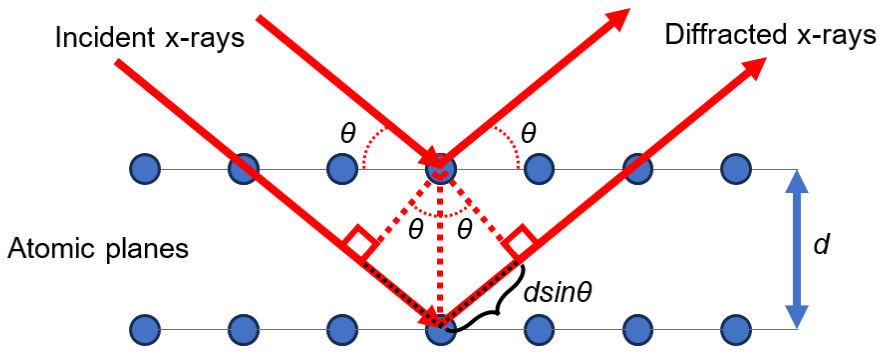

Figure 2.6: *Schematic of the geometric conditions required to fulfil Bragg's Law.*

behind XRD is that information about the sample structure (i.e., "real" space) can be determined by illuminating the samples with x-rays and studying the diffracted patterns which reveal portions of "reciprocal" space. This reciprocal space is a Fourier transform of the real space atomic ordering.

A simple physical picture of how diffraction patterns are produced by perfect single crystals can be described by Bragg's Law of diffraction, schematically shown in Figure 2.6. X-rays illuminating a sample will elastically scatter off of the atoms in a material (specifically, the electrons surrounding the atoms). These x-rays will then constructively or destructively interfere with each other as they propagate away from the atoms. In the case of single crystals, the x-rays coherently scatter from the atomic planes in the crystal as shown in Figure 2.6. When the incident x-rays illuminate the sample with an atomic plane spacing *d*, complete constructive interference is achieved only when the path length differences (i.e., black dotted line in Figure 2.6) between all scattered x-rays are integer multiples of the x-ray wavelength λ. Bragg's Law specifies this conditions as

$$2d \sin\theta = n\lambda \qquad \text{Eq. 2.7}$$

where n is an integer and θ is the angle of the incident x-ray beam. Moreover, the constructively interfering x-ray beam exits the sample at the same angle θ relative to the atomic plane. In the

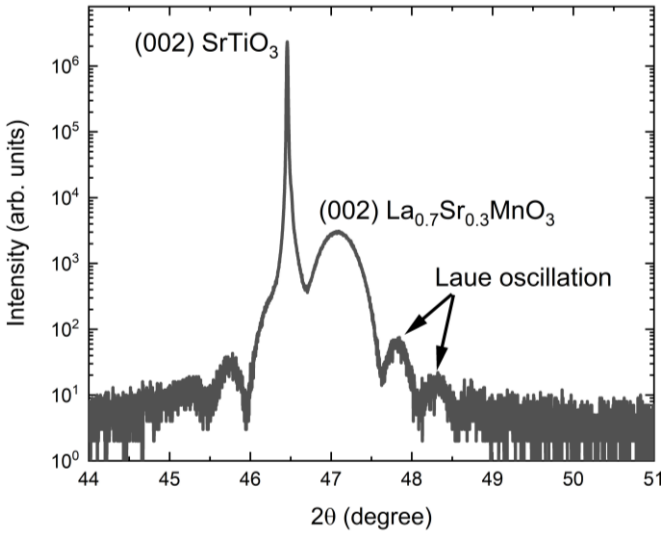

Figure 2.7: *Example HRXRD experimental data of a 20 nm LSMO film deposited on a (001) - oriented STO substrate.*

context of the XRD instrument, this diffraction condition, known as a Bragg reflection, requires either a θ/θ or θ/2θ configuration (see Section 2.3.1).

XRD can be used to investigate the structural properties of epitaxial thin films. However, because the observable Bragg reflections in these samples can be as close as 0.001° [74], a special optics setup is required to enable high (angular) resolution XRD, or HRXRD, measurements. In other words, an HRXRD measurement requires instrumentation which can produce highly collimated and monochromatic x-ray beam. The details of the instrumentation for the HRXRD system used in this dissertation is discussed in Section 2.3.1.

Figure 2.7 shows an example HRXRD measurement of the same LSMO film on a (001)-oriented STO substrate in Figure 2.7. The most intense peak corresponds with the (002) Bragg reflection of the single crystal STO substrate. The second-most intense peak (2θ ~ 47°) corresponds to the (002) LSMO diffraction peak. For single crystalline thin films, the difference between the line widths of the substrate and thin films reflect the difference in the amount of material under the diffraction condition [74]. Adjacent to the (002) LSMO and (002) STO Bragg reflections in Figure

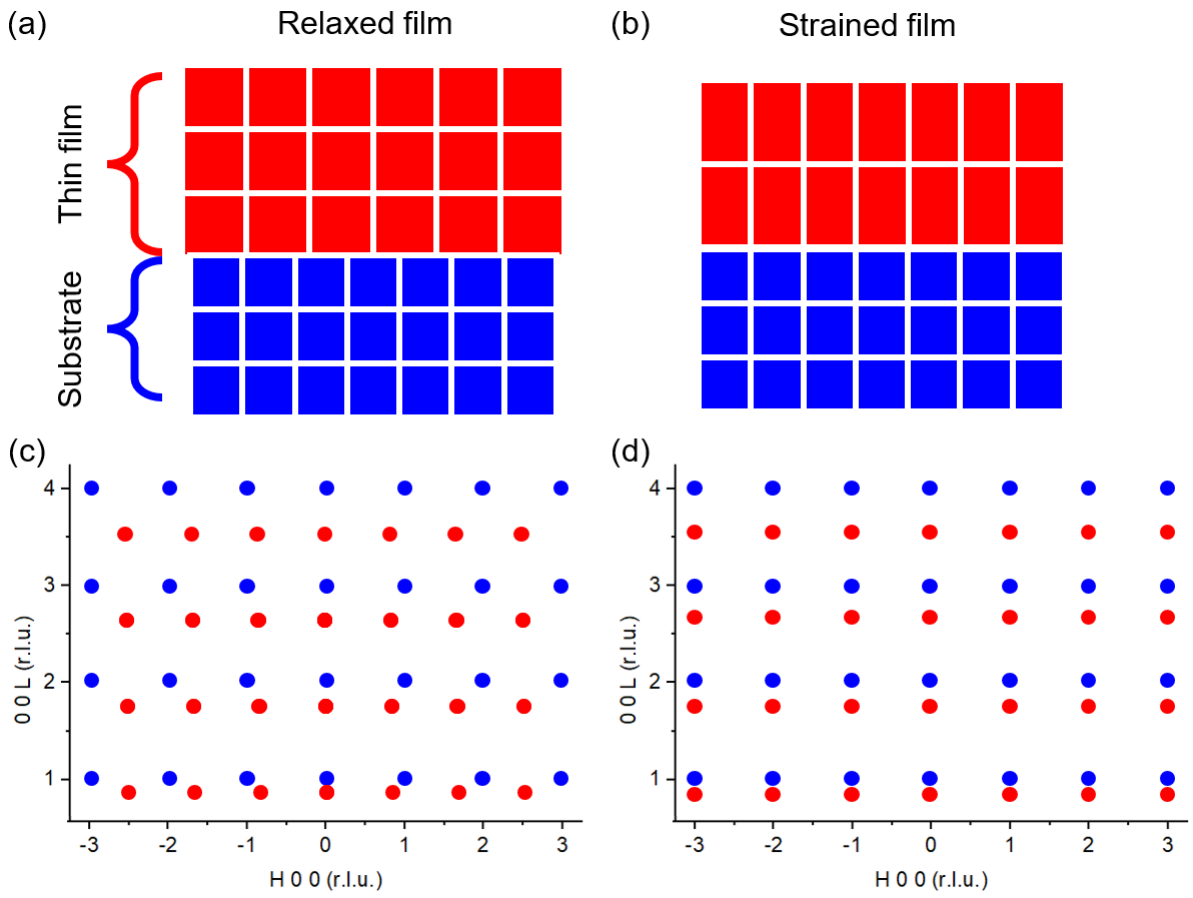

Figure 2.8: *(a,b) Schematics of an epitaxial thin film (red boxes) that is relaxed (a) or coherently strained (b) with the underlying substrate (blue boxes). (c,d) Associated reciprocal space maps of the relaxed (c) and strained (d) thin film systems, where the red and blue dots correspond with the thin film and substrate peaks, respectively. Is it assumed that both the substrate and relaxed films have cubic unit cells, and that the bulk film lattice parameter is larger than the substrate lattice parameter. The (0 0 L) and (H 0 0) axes are shown with reciprocal lattice units (r.l.u.) of the STO (001) substrate.*

2.7 are oscillations which bear some resemblance to the LSMO diffraction peak. These features, known as Laue oscillations, are similar to the Kiessig fringes observed in XRR experiments and reflect the thickness of the thin film. Unlike Keissig fringes, which do not depend on the crystallinity of the thin film, Laue oscillations reflect the partial destructive interference between

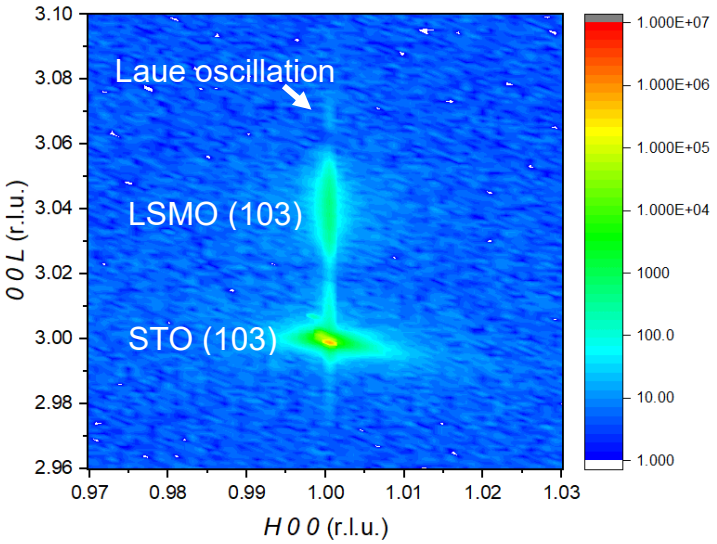

Figure 2.9: *Reciprocal space map of a strained 20 nm LSMO film on STO, scanned around the STO (103) Bragg reflection.*

the a finite number of coherently diffracting unit cells [77]. Thus, the presence of these oscillations indicates a low concentration of defects, uniform d-spacing throughout the film thickness, and are broadly used as a qualitative indication that the epitaxial thin film possesses a high degree of crystallinity.

The HRXRD measurement described above is an example of a symmetric scan, where the x-ray beam and detector angles are symmetric about the sample normal. This scan is useful to assess the crystalline quality of the sample and quantify the out-of-plane lattice parameter. However, symmetric scans alone do not shed light on the in-plane lattice parameter of the film and substrate. Since the properties of perovskites are sensitive to the strain state of the material, it is important to assess whether the grown thin film is possesses its nominal crystal structure (i.e., relaxed, Figure 2.8(a)) or is laterally matched with the substrate (i.e., strained, Figure 2.8(b)). The corresponding diffraction patterns (i.e., reciprocal space maps, RSMs) are schematically shown in Figure 2.8(c,d).

In the context of the RSMs shown in Figure 2.8(c,d), symmetric scans are vertical line scans when $H = 0$ r.l.u., where r.l.u. is the reciprocal lattice unit of the (001)-oriented STO substrate (i.e., the Miller indices of the planes). The most noticeable difference between the RSMs of the relaxed and strained films is the extent of horizontal alignment (i.e., matching in-plane lattice parameter) between the film and substrate peaks. In order to probe the extent of horizontal misalignment between the peaks, an asymmetric scan needs to be performed which can access parts of reciprocal space beyond $H = 0$ r.l.u. In practice, an area of reciprocal space is scanned to produce an RSM. Figure 2.9 shows an example RSM measured around the STO (103) peak for the same LSMO sample used in Figures 2.5 and 2.7.

2.5 – Soft X-ray Absorption Spectroscopy

X-ray absorption spectroscopy (XAS) is a technique used to investigate the chemical, electronic, and magnetic properties of a sample. In XAS, the amount of monochromatic (i.e., single wavelength/energy) x-rays a sample absorbs is measured as the photon energy is varied (e.g., through the use of monochromators). When the photon energy matches the energy required to excite a core level electron to a valence level hole (i.e., Figure 2.10 [41]), the sample will strongly (resonantly) absorb those x-rays to drive those electronic transitions. These resonant absorptions appear as "peaks" in an XAS measurement. The peak shapes and positions in XAS measurements serve as fingerprints of the chemistry and local bonding environment in the studied material. As will be discussed in the later sections, XAS can also be used as an element-resolved sensor for magnetic ordering. For the 3d transition metal perovskites studied in this work, the strongest magnetic signal can be detected through the 2p → 3d electronic excitation, known as the *L*-edge which occur within the soft x-ray photon energy range of 400 – 1000 eV [78].

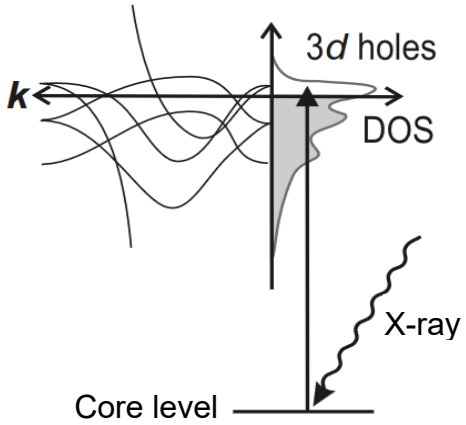

***Figure 2.10**: Schematic of an x-ray induced excitation of a core level electron into an empty 3d valence state. Adapted from Ref. [41].*

Several methods exist to measure an XAS signal which exploit two aspects of the x-ray induced electronic excitation mechanism. The first set of methods involves measuring the amount of x-rays that are absorbed to induce electronic excitation. This absorption signal can be detected through a transmission mode, where the amount of x-rays transmitted through a sample is measured. For this mode to work, the sample needs to be x-ray transparent with thicknesses on the order of 100 nm. The luminescence yield (LY) measurement mode is similar to the transmission mode, but uses a sample grown on a scintillating substrate. This substrate absorbs x-rays transmitted through the sample and emit visible light that is detected by a photodiode [79].

The second set of methods involves measuring the relaxation process which follows the core-to-valence level electronic excitation. To minimize the system energy, the excited electron will fall back into the core-level hole produced during the excitation and releases energy either in the form of a photon (fluorescence) or by emission of an Auger electron. I will focus on the latter relaxation mechanism as it is of greatest relevance to this dissertation work. Within a depth of several Angstroms, the Auger electrons can escape the sample into vacuum. Beyond this depth,

the Auger electrons will induce a cascade emission of secondary electrons which can escape the sample within a depth of several nanometers. The total amount of photoemitted electrons, called the total electron yield (TEY), is directly proportional to the probability of x-ray absorption [41].

XAS measurements can be performed at facilities known as synchrotron light sources, which produce high brilliance and highly monochromatic x-rays for scientific research. The synchrotron x-rays used in this dissertation work are produced by so-called undulator insertion devices. These instruments are sets of track-like structures containing periodic arrangement of permanent dipole magnets which serve to "undulate" the electron beam in the synchrotron storage ring which, in turn, produce x-rays. The photon energy and polarization produced by undulators can be tuned through the gap size between the undulator tracks and the phase between the dipole structure of the tracks, respectively. The light emitted from the undulator then passes through a series of monochromators, focusing mirrors, and apertures before arriving at the experimental setup known as endstations. This dissertation specifically uses the soft x-rays produced at the Advanced Light Source (ALS) at undulator beamlines (BL) 4.0.2 to perform x-ray magnetic circular/linear dichroism (XMCD/XMLD) spectroscopy and 11.0.1.1 to perform x-ray photoemission electron microscopy (X-PEEM), which will be discussed in the following sections.

2.5.1 – X-ray Magnetic Circular Dichroism

Ferromagnetism in a material is associated with a net imbalance between the population density of up and down spin states in the valence level (e.g., colored regions in the density of states schematic in Figure 2.11(a)), originating from the exchange interaction discussed in Chapter 1. Ferromagnetism can be investigated using a technique capable of probing the difference in up and down spin *holes* present above the Fermi level (white regions in the density of states schematic in Figure 2.11(a)). X-ray magnetic circular dichroism (XMCD) is a XAS-based technique which uses

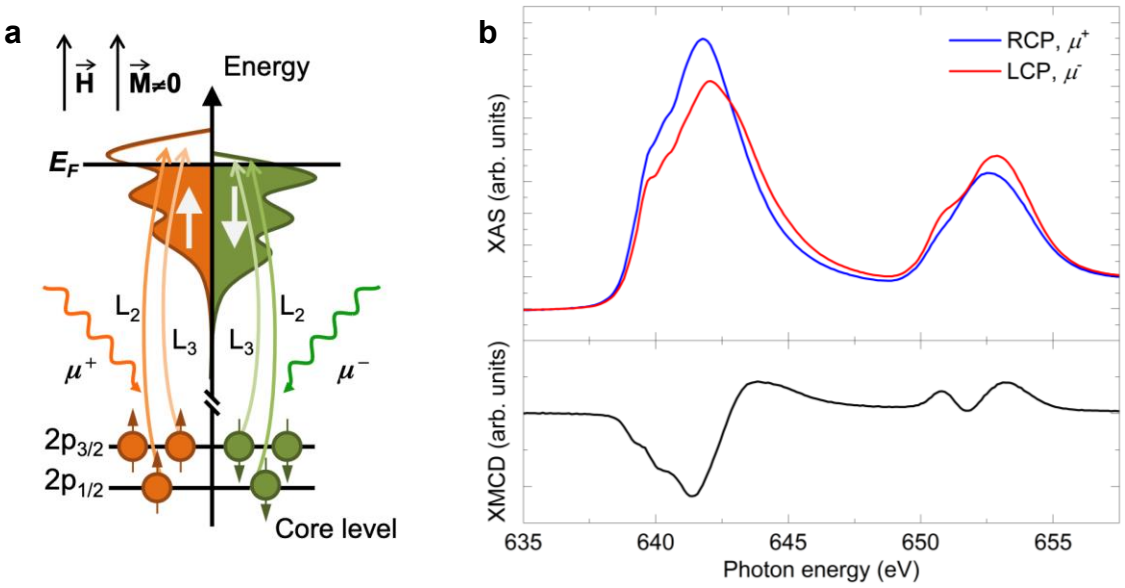

***Figure 2.11**: (a) Schematic of the circular-polarization-dependent electron excitation from the 2p core level to 3d valence states [80]. (b) XAS and XMCD spectra for an LSMO film at 80 K. RCP and LCP corresponds with right- and left-hand circularly polarized x-rays, respectively.*

circularly polarized light to preferentially excite up (down) spin core-level electrons into corresponding up (down) spin holes based on dipole selection rules [41,80]. In an XAS measurement, this behavior corresponds with different absorption spectra acquired for left/right hand circularly polarized (LCP/RCP) light. Figure 2.11(b) shows an example of this behavior in XAS measurements performed on an a LSMO thin film. The difference between XAS signals acquired with RCP and LCP is the XMCD signal.

The strength of the XMCD signal, I_{XMCD}, for an magnetically saturated (i.e., magnetized with an external field) isotropic system, scales as

$$I_{XMCD} \propto m \cos\theta \qquad \text{Eq. 2.8}$$

where θ is the angle formed between the x-ray beam and the magnetic moment $\boldsymbol{m}$ with magnitude m. In other words, the XAS-XMCD signal reflects the *net* magnetic ordering within the area probed

by the x-ray beam. Since the maximum XMCD signal is acquired when the sample is magnetized parallel/antiparallel with the x-ray beam, XMCD spectroscopy experiments are often conducted with the application of a saturating magnetic field (in the case of LSMO, H_c ~ 50 Oe). The line shape of XMCD spectra reflects which elements and their valence state contribute to magnetism. It is important to note that XMCD can serve to facilitate both spectroscopy and magnetometry measurements of a sample, as the XMCD signal strength depends on the net magnetization. The elemental sensitivity of XMCD enables element-resolved magnetometry measurements where, for instance, hysteresis loops can be measured for different elements by recording the XMCD signal as a function of an applied magnetic field.

2.5.2 – X-ray Magnetic Linear Dichroism

To probe the axial alignment of spins, as is the case for antiferromagnetic materials, x-ray magnetic linear dichroism (XMLD) can be performed. In general, linearly polarized x-rays probe any deviations from a spherical electronic charge which can originate from several different sources. Anisotropy in charge distribution can originate from chemical bonding and is referred to as x-ray *natural* linear dichroism (X*N*LD). In X*M*LD, a spherical charge density is distorted by alignment of spins and arises from spin-orbit coupling [41]. The asymmetry is induced relative to the *axis* of spin alignment. Both the natural and magnetic linear dichroism effects may co-exist. Consequently, x-ray linear dichroism (XLD) experiments must be designed carefully to isolate the contributions from X*N*LD and X*M*LD effects. One method of separating these effects is to perform temperature- and field-dependent measurements. Another method to avoid the structural-component of the XLD signal is to acquire spectra along the same crystallographic directions. Similar to XMCD, the XMLD intensity follows the following cosine-based relationship

$$I_{XMLD} \propto \cos^2 \phi \qquad \text{Eq. 2.9}$$

where ϕ is the angle formed between the polarization E-vector and the magnetic axis of alignment. For antiferromagnets, this axis of alignment is referred to as the Néel vector, L.

2.6 – X-ray Photoemission Electron Microscopy (X-PEEM)

Sections 2.5, 2.5.1, and 2.5.2 discuss how XAS can be used to probe the chemical and magnetic information about a sample. Spectroscopy, however, provides information which is spatially averaged over the region irritated by the x-ray beam. To investigate the spatial variation in sample chemistry and magnetic ordering, microscopy techniques must be employed. One such technique is known as x-ray photoemission electron microscopy (X-PEEM) which is schematically shown in Figure 2.12 [81]. X-PEEM is a photon-in electron-out technique, where an electron microscope is used to image the spatial distribution of electrons photoemitted by a sample irradiated with monochromatic x-rays. In the context of XAS and XMCD/XMLD, X-PEEM enables imaging of the spatial variation in the TEY emission across the sample surface, which reflect the chemical, electronic, and magnetic heterogeneities present. That is, the contrast observed in X-PEEM image are the XAS and XMD signals. Additional contrast also arises from sample topography and work function variation across the surface.

The photoemitted secondary electrons is collected by the microscope by applying an accelerating voltage of ~ 20 kV between the sample surface and an electron objective lens. This bias serves to preserve the spatial information of local photoelectron emission as the electrons would otherwise travel in random directions. Inside the microscope, these electrons pass through a series of lenses in the microscope and projected on to a charge-coupled device (CCD) camera to produce an image.

Acquisition of an X-PEEM image with XMCD contrast, henceforth referred to as XMCD-PEEM image, first requires the identification of the photon energy which maximizes the XMCD

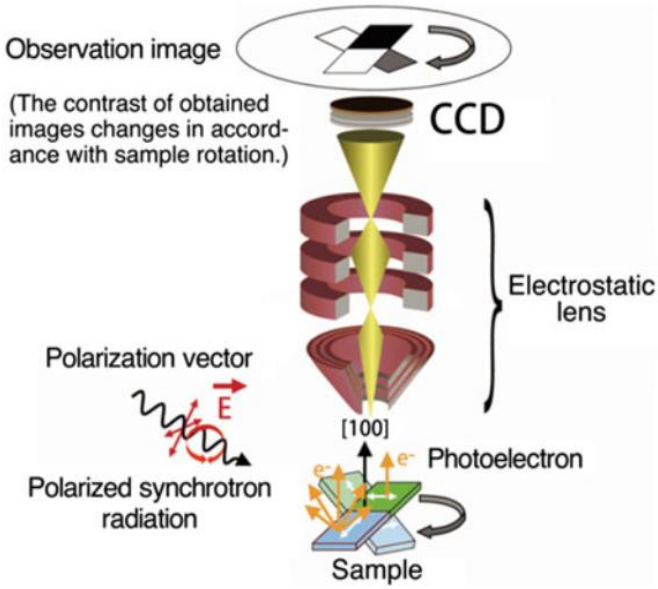

Figure 2.12*: Schematic of the optical configuration in an x-ray photoemission electron microscope [81].*

contrast. In the case of LSMO, several X-PEEM images are acquired as the photon energy is incrementally varied (~0.2 eV steps) across the Mn L_3 edge which exhibits the strongest XMCD signal (e.g., Figure 2.11(b)). The photon energy of the x-ray is then set to the value which maximizes the XMCD signal strength, which typically occurs at photon energies ~0.2 eV lower than the XAS peak. At this fixed energy, several X-PEEM image sets are acquired by alternating between RCP and LCP. Figure 2.13(a) and (b) shows X-PEEM images of a 2 μm square micromagnet patterned into LSMO acquired with RCP and LCP, respectively. To isolate the XMCD signal, an asymmetry calculation is performed as

$$I_{XMCD} = \frac{I_{RCP} - I_{LCP}}{I_{RCP} + I_{LCP}} \qquad \text{Eq. 2.10}$$

where I_{RCP} and I_{LCP} represents the intensity measured with RCP and LCP, respectively. The asymmetry calculation serves to remove other sources of contrast, such as topography (i.e., the "shadows" surrounding the square micromagnet in Figure 2.13(a,b)) and work function variations,

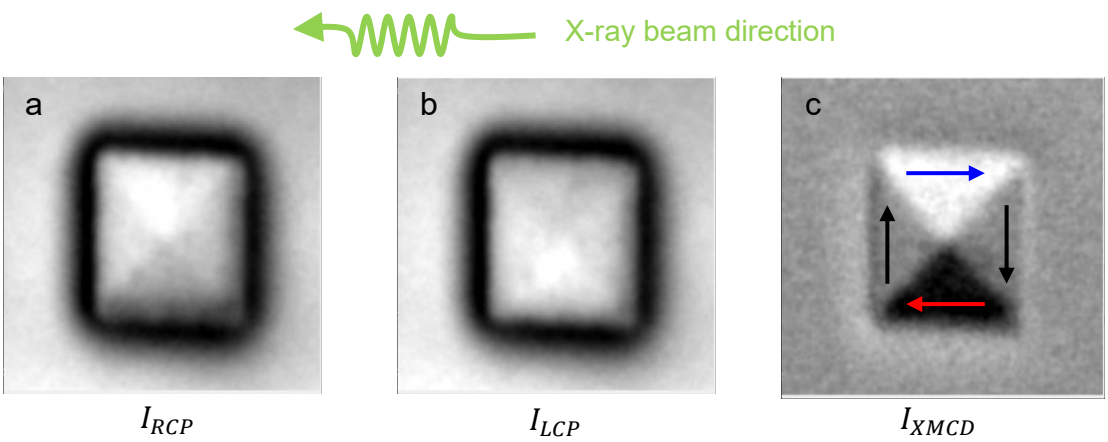

***Figure 2.13**: (a,b) X-PEEM images of a 2 μm square micromagnet patterned into a 40 nm LSMO film captured with (a) right-hand polarized x-rays I_{RCP} and (b) left-hand polarized x-rays I_{LCP} at 110 K. (c) XMCD-PEEM image calculated from the asymmetry equation $(I_{RCP}-I_{LCP})/(I_{RCP}+I_{LCP})$. The red, black, and gray arrows indicate the magnetic domain orientation. The green squiggly line indicates the in-plane orientation of the x-ray beam for all measurements.*

from the calculated XMCD-PEEM image. Figure 2.13(c) shows an XMCD-PEEM image calculated from Figure 2.13(a,b) using Eq. 2.10.

Interpretation of magnetizations from XMCD-PEEM images can be based off of Eq. 2.8 as well as consistency with domain theory discussed in Chapter 1. This latter point will be expanded upon in the following discussion. In the XMCD-PEEM image shown in Figure 2.13(c), the white and black domain corresponds with magnetization orientations which are parallel (black, red arrow) and antiparallel (white, blue arrow) with respect to the x-ray beam. The gray regions in Figure 2.13 possess $I_{XMCD} \sim 0$, which are caused by one of two different effects. If the region is ferromagnetic (i.e., non-zero *m* within the square micromagnet), then gray regions indicate that the local magnetization is perpendicular to the x-ray beam. The XMCD contrast cannot distinguish whether the domain magnetization is pointing upwards or downwards. In this situation, reasonable assumptions about the domain magnetization can be made based on the principle of energy

minimization: The flux closure Landau configuration (Figure 2.13(c) and 1.13(b)) is energetically preferable over any other orientations of the gray domain.

Alternatively, the gray contrast indicates that the region possess substantially weaker or non-existent ferromagnetic ordering, which is the case for the matrix regions surrounding the square micromagnet in Figure 2.13(c). If the nature of magnetic heterogeneities within a sample is unknown, then the origin for $I_{XMCD} \sim 0$ can be experimentally resolved by measuring the sample with two different orientations (e.g., rotate the sample by ~45°). In this second orientation, regions which previously had perpendicular magnetizations will become darker/brighter while non-ferromagnetic regions will remain gray. In practice, measuring the sample at two different orientations may be impractical as the amount of time consumed (i.e., to reorient the sample, re-establish ultra-high vacuum, and relocate the previously measured position) may be comparable to the total amount of experimental time allotted for X-PEEM instruments.

This dissertation work utilizes the PEEM3 microscope at the ALS BL 11.0.1.1. The PEEM3 microscope is capable of establishing sample temperatures between 30 K – 390 K which enables the measurement of magnetic domains in samples with T_C below room temperature. BL11.0.1.1 has a photon energy range of 160 eV – 1.8 keV and can access both circular and linear polarized x-rays. While the maximum resolution of the microscope largely depends on the samples and accelerating voltages used, one can expect a nominal spatial resolution of ~20-50 nm.

2.6.1 – Characterization of Artificial Spin Ice XMCD-PEEM Images

To characterize XMCD-PEEM images of ASI systems, the magnetizations of each nanoisland are first interpreted based off the XMCD contrast. For ASIs with Ising-like nanoislands, each nanoisland will possess a uniform contrast as shown in Figure 2.14(a) and (b). If the nanoisland lengths are not perpendicular to the x-ray beam (i.e., “90°” in Figure 2.14(a)), then the

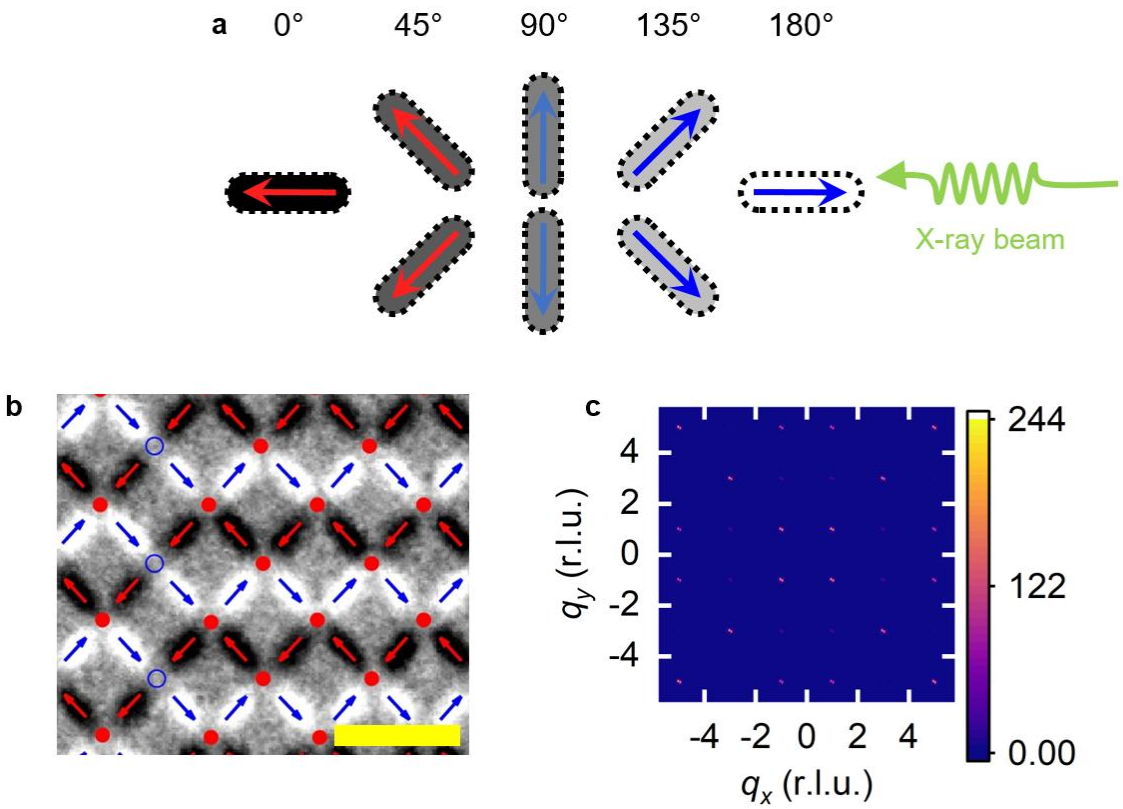

***Figure 2.14**: (a) Schematic of the XMCD intensity as a function θ, the angle between the magnetization orientation and the x-ray beam direction. Nanoislands capable of only bearing uniform magnetizations will appear as uniformly colored stadium-shaped regions in the XMCD-PEEM images. (b) Zoomed-in XMCD-PEEM image of an LSMO square ASI, with the XMCD contrast adjusted for visual clarity. Nanoisland magnetizations are indicated with the red and blue arrows. Type I and II vertices are indicated with the red dot and blue circles, respectively. Yellow scale bar: 1 μm. X-ray beam orientation for both (a) and (b) are indicated with the squiggly green arrow. (c) An example magnetic structure factor for a square ASI containing a majority (96%) of Type I vertices.*

XMCD grayscale contrast will be dark or bright if the magnetization of the nanoisland is generally point parallel or antiparallel to the x-ray beam, respectively. As discussed in Section 2.5, the XMCD contrast cannot distinguish whether the domain magnetization is generally pointing

upwards or downwards. However, the perpendicular-component of the magnetizations can be assigned by employing a shape anisotropy approximation, where the nanoislands are assumed to possess magnetizations along the length of the nanoisland. This magnetization assignment for nanoislands with 45° orientations is schematically shown in Figure 2.14(a) and (b). For visual clarity, the contrast in Figure 2.14(b) was readjusted by enhancing the darkness and brightness of the black and white nanoislands, respectively. For nanoislands which contain spin textures other than single domains, manual identification and assignment of the spin texture state was performed as discussed in Chapter 3.

After assigning the magnetizations to each nanoisland, the ASIs were characterized using two quantities: vertex statistics and magnetic structure factor (MSF) calculations. The vertex statistics indicates how close the ASI is to its ground state by showing the populations of different energy vertex states present in the system (see Sections 1.1.2.1 and 1.1.2.2). As an example, the Type I and II vertex states are shown in Figure 2.14(b) as red dots and blue circles, respectively. This quantity also depends on the strength of dipolar coupling between the nanoislands. For nanoislands which experience no dipolar interactions (i.e., infinite nanoisland separation), the vertex statistics will be representative of the different multiplicities of each vertex state. As the nanoisland interactions become stronger (e.g., by reducing nanoisland separation or increasing the nanoisland moment), the population of the ground state Type I vertex state will increase while the higher energy vertex states will decrease.

The MSF [25,26] is a computed magnetic scattering pattern of the ASI, calculated as

$$I(\boldsymbol{q}) = \frac{1}{N}\sum_{i=1}^{N}\sum_{j=1}^{N} \boldsymbol{S_i^{\perp}} \cdot \boldsymbol{S_j^{\perp}} \exp\left(i\boldsymbol{q} \cdot \boldsymbol{r_{ij}}\right) \qquad \text{Eq. 2.11}$$

where the I is the scattering intensity at a reciprocal space vector $\boldsymbol{q}$ with unit vector $\hat{\boldsymbol{q}}$, and $\boldsymbol{S^{\perp}}$ is the component of the spin vector $\boldsymbol{S}$ perpendicular to $\boldsymbol{q}$ calculated as

$$\boldsymbol{S}^{\perp} = \boldsymbol{S} - (\hat{\boldsymbol{q}} \cdot \boldsymbol{S})\hat{\boldsymbol{q}} \qquad \text{Eq. 2.12}$$

Figure 2.14(c) shows an MSF calculated for the full image of the ASI in Figure 2.14(b). For ASIs which exhibit long-range and homogeneous magnetic ordering, intense and narrow peaks will appear in the MSF. As the ASI loses long-range ordering (e.g., due to thermally-induced fluctuations of the nanoisland magnetizations), the peaks shown in an MSF will become weak and broadened while still possessing structure. An example of this behavior for the square ASIs is shown in Figure 3.3 of Chapter 3. Analysis of the MSF peak shape and intensity can allow for quantitative comparison of magnetic ordering between the different ASIs.

2.7 – Micromagnetic Simulations

Spin texture formations in magnetic micro- and nanostructures can be simulated using software called micromagnetic simulation packages. Micromagnetic simulations model the system using a continuum approximation of the magnetic moments. Inputs for this simulation are the magnetic material properties (e.g., M_{sat}, A_{ex}, K_1), the 2D or 3D geometry of the magnetic body, and the magnetization of the body. In the case of the package MuMax^3 [62], which was utilized in this dissertation, a finite-difference method was used to discretize the system into a 2D or 3D grid of orthorhombic cells, where each cell is assigned a unit magnetization vector $\boldsymbol{m}$. Here, we will use the same definition of $\boldsymbol{m}$ and $\boldsymbol{M}$ in Section 1.3. For accurate simulations, the dimensions of the orthorhombic cells should be comparable to or smaller than the exchange length l_s

$$l_s = \sqrt{(2A_{ex})/(\mu_0 M_{sat}^2)} \qquad \text{Eq. 2.13}$$

For the LSMO nanomagnets studied in this work, $l_s \sim 6$ nm (see Chapters 3 and 4).

Micromagnetic simulations solve the Landau-Lifshitz-Gilbert equation, which describes the time-dependent equation of motion for a magnetic moment under an effective magnetic field

$$\frac{\partial \boldsymbol{M}}{\partial t} = \gamma \boldsymbol{M} \times \boldsymbol{H}_{eff} - \frac{\alpha\gamma}{M_{sat}}\left(\boldsymbol{M} \times \left(\boldsymbol{M} \times \boldsymbol{H}_{eff}\right)\right) \qquad \text{Eq. 2.14}$$

where γ is the gyromagnetic ratio, α is the empirical Gilbert damping parameter, and $\boldsymbol{H}_{eff}$ is the effective field [63]. The first term represents the precessional motion of $\boldsymbol{M}$ under a magnetic field while the second represents the damping of the $\boldsymbol{M}$ precession (i.e., tendency for $\boldsymbol{M}$ to eventually reach its equilibrium orientation). $\boldsymbol{H}_{eff}$ allows for the different magnetic energy terms discussed in Section 1.3.1 to be represented as magnetic fields which effectively act on $\boldsymbol{m}$. That is, the exchange and magnetocrystalline anisotropy terms can be written as effective fields $\boldsymbol{H}_{ex}$ and $\boldsymbol{H}_{mca}$, respectively. $\boldsymbol{H}_{eff}$ itself is the sum of the different effective field contribution. The time-dependent magnetization evolution can be simulated by numerically evaluating Eq. 2.14 over several time step iterations.

Micromagnetic simulations can be used to determine (meta)stable spin texture states. In equilibrium, the torque on $\boldsymbol{M}$ exerted by $\boldsymbol{H}_{eff}$ must vanish (i.e., $\boldsymbol{m} \times \boldsymbol{H}_{eff} = 0$) [61,63]. In other words, the lowest energy state is one where $\boldsymbol{M}$ is aligned with the local $\boldsymbol{H}_{eff}$. By using non-zero damping ($\alpha > 0$ in Eq. 2.14), micromagnetic simulations can be used to iteratively minimize the total energy of a modeled magnetic system. One strategy to access (meta)stable states is to use large values of α so that the damping term of Eq. 2.14 dominates [63]. In MuMax^3, a built-in relax function was used which disables the precessional term in Eq. 2.14 and iteratively advances the simulation until the total energy and torque variation achieve a threshold minimum [62].

2.8 – Conclusion

This chapter summarizes the different techniques used to fabricate and analyze perovskite-oxide-based ASI systems. PLD was used to synthesize pristine LSMO thin films, which were characterized using x-ray diffraction, x-ray reflectometry, and vibrating sample magnetometry. ASIs were patterned into these thin films using a process based on electron beam lithography and flood argon implantation. XMCD-PEEM studies of the ASIs were performed at the Advanced

Light Source in Lawrence Berkeley National Laboratory, which enabled the characterization of magnetic ordering and spin texture states in the LSMO-based ASIs. Micromagnetic simulations were performed to understand the energetics of different spin texture states observed in the ASI systems.

Chapter 3: Formation of Complex Spin Textures in Thermally Demagnetized $La_{0.7}Sr_{0.3}MnO_3$ Artificial Spin Ice Structures*

3.1 – Introduction

Artificial spin ices (ASIs) are lithographically patterned arrays of interacting single domain magnetic nanoislands that can be represented as an ensemble of dipolar-coupled Ising macrospins that are unable to simultaneously minimize all neighboring magnetic interactions (i.e., they exist in a frustrated state). Originally introduced as an engineered analog of spin ice crystals whose frustrated physics could be directly visualized with conventional magnetic microscopy, [2] ASIs have served as a platform for designing and investigating phenomena including configurational excitations resembling magnetic monopole-like defects [3–5], phase transitions between different global nanomagnetic ordering states [6–8], and magnetically-reconfigurable spin-wave dynamics [9]. In ASIs, the collective physics of the entire array is highly sensitive to the interactions between individual nanomagnetic elements (i.e., *inter*-island interactions), which are influenced by the nanoisland arrangement, geometry, and magnetization. Thus, ASIs have received attention for their promising potential for developing low-power computing devices with functionalities that can be magnetically reconfigured after fabrication, such as tunable GHz-frequency dynamics in ASI-based magnonic crystals [9] and switchable gate operations in nanomagnetic logic architectures [10].

Investigations of ASI systems have traditionally used geometry-based degrees of freedom as the array geometry strongly influences the net dipolar interactions between nearest-neighboring nanoislands and, therefore, controls the collective physics in these systems. These studies have

* The content of this chapter has previously been published in Ref. [109]

produced a wide range of ASI lattice geometries including nanoisland assemblies constructed from square, Tetris “T-block”, and brick-shaped (brickwork) tilings [1,2,28,29,82]. Additionally, the interaction strength between magnetically coupled nanoislands in these arrays can be modulated through changes in both the nanoisland size as well as interisland spacing, allowing these systems to access different equilibrium configurations [83,84] or alter the system degeneracy [4,25].

A common feature that many ASI studies share is their use of the soft ferromagnetic alloy permalloy ($Ni_{80}Fe_{20}$) as the magnetic material. Permalloy possesses a near absence of magnetocrystalline anisotropy which defines the crystallographic “easy” axis that the magnetization preferentially aligns along (i.e., all in-plane axes are equally easy) [85]. The combined use of an elongated island geometry and nanometer-scale dimensions can be used to engineer single domain states by preventing the formation of domain walls (~100 nm in width) associated with multidomain states. In other words, the nanoislands possess a shape anisotropy that favors magnetization along the long axis of elongated nanoislands that can be represented as a macrospin within an Ising framework where the island magnetization exists in one of two states (e.g., “up” or “down”). By engineering the nanoisland shape anisotropy, it may be assumed that the type of spin texture (e.g., Ising-like or vortex) formed will be determined by the island-intrinsic (i.e., *intra*-island) shape effects with negligible influence from *inter*-island dipolar interactions.

While permalloy-based ASI systems have facilitated the investigation of magnetic frustration and dynamics in various array geometries, the complex oxide class of materials introduces several unique opportunities for ASI studies. Complex oxides possess charge, orbital, lattice, and spin degrees of freedom; and heterostructures or nanostructures of these materials exhibit functional properties that can be tuned using parameters such as substrate orientation, individual layer thickness, and epitaxial strain state [35,36]. The patterning of complex oxide thin

films into nano- and micron-sized polygons has been shown to result in equilibrium magnetic domain structures that depend on the competition between shape and magnetocrystalline anisotropy energies as well as exchange coupling interactions at interfaces [58–60,86,87]. Thus, complex oxides introduce an opportunity to incorporate their rich variety of tunable functional properties with the designable physics of ASIs.

Additionally, complex oxides have demonstrated promise for use in thermally-active ASI studies [23]. ASIs fabricated from the epitaxial complex oxide $La_{0.7}Sr_{0.3}MnO_3$ (LSMO) offer the advantage of possessing a bulk Curie temperature, T_C ~370 K (i.e., near room temperature) as well as exhibiting chemical stability up to 873 K in both vacuum and ambient pressure environments [88]. Therefore, LSMO-based ASIs can facilitate investigations of ASI ground states through thermal annealing protocols (i.e., raising the system temperature close to T_C) [22,89,90], unlike permalloy-based systems which face experimental challenges such as thermal degradation imposed by high temperature requirements (~800 K) [22], or through the use of ultrathin (~3 nm) nanoislands which may be prone to variations in thickness and, consequently, blocking temperature [23].

In this work, I report on our investigation of thermalized brickwork ASIs fabricated from the complex oxide LSMO. Using magnetic domain imaging performed using an X-ray photoemission electron microscope (X-PEEM), I performed *in-situ* thermal demagnetization and observed the formation of complex spin textures (CST), which consist of single- and double-vortex states. These states can be stabilized using *both* the nanoisland width and interisland spacing. Micromagnetic simulations demonstrated that these spin textures consist predominantly of single- and double-vortex states. The simulations also provide an understanding of their energetics which arises from a competition between *intra*-island effects (i.e., shape anisotropy and exchange energy)

and *inter*-island effects (i.e., magnetostatic interactions between nearest neighbor nanomagnets). By constructing a width- and spacing-dependent phase diagram from the simulated energy surfaces, I found a correlation between the experimentally-observed CST abundance and the associated energetic preference of Ising or CST states.

3.2 – Methods

A 40-nm thick LSMO film was grown epitaxially on a (001)-oriented Nb-doped $SrTiO_3$ (0.05 wt. % Nb) substrate using pulsed laser deposition with a laser fluence of ~1 J cm^{-2} and frequency of 1 Hz. During the growth, the substrate temperature was held at 700 °C with an oxygen pressure of 0.3 Torr. The films were slowly cooled to room temperature post deposition in 300 Torr O_2 to ensure proper oxygen stoichiometry. Structural characterization was performed with X-ray reflectivity and X-ray diffraction to confirm coherent growth, crystalline quality, and thickness of the film (for details, see ref [23]). ASI arrays were defined in different regions of a single LSMO film using a patterning technique based on the local modification of the structural and magnetic order by a flood Ar ion implantation (for details, see refs [59,91]). Each ASI array contained over 900 stadium-shaped nanoislands (rectangles with semicircle endcaps) with a fixed length of 470 nm and widths, *W*, varying from 100 to 175 nm to control the nanoisland moment, *m*. These nanoislands were patterned such that the two-dimensional ⟨10⟩ axes of the ASI were aligned with the ⟨110⟩ in-plane easy axes of the LSMO film under tensile strain [92]. The spacing between each nanomagnet was modified through the ASI lattice parameter, *a*, where each three-island vertex in the brickwork structure (Figure 3.1(a)) corresponds to a point in a square lattice (henceforth any discussions associated with lattices will only be associated with the ASI and not the LSMO crystal structure). By varying the value of *a* from 600 nm to 650 nm, I was able to fine tune the interisland coupling strength, $J \equiv m^2/a^3$, which reflects the scale of dipolar interaction [84].

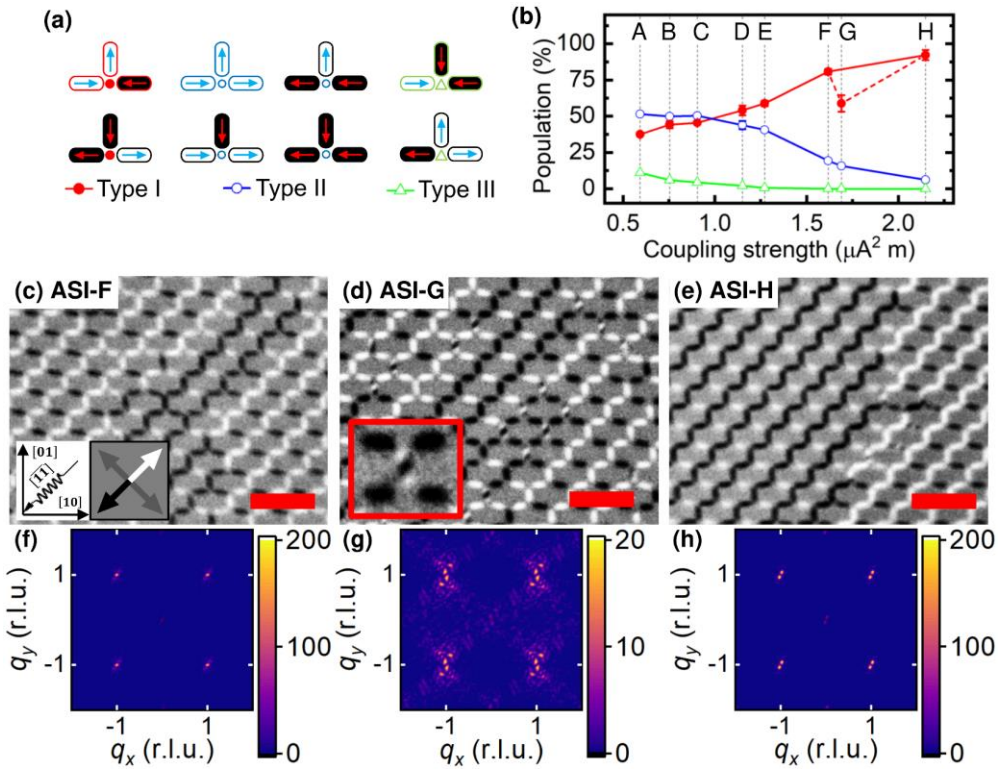

Figure 3.1: *(a) Schematic of the eight possible Ising-like moment configurations at a three-nanoisland vertex. Type I, II, and III vertices are designated as red solid circles, blue open circles, and green triangles, respectively. (b) Average vertex population for ASIs A-H plotted as a function of coupling strength, J. Each error bar correspond to the standard deviation between 2-4 unique XMCD-PEEM images of the ASIs. In ASI-G, the Ising model breaks down as the magnetic configuration of 9% ± 2% of the nanoislands cannot be classified as single domains, causing a deviation in the Type I population trend as indicated by the dashed line. (c-e) XMCD-PEEM images and (f-h) corresponding MSF calculations of ASI-F (c, f), ASI-G (d, g), and ASI-H (e, h), respectively. The experimental geometry and associated magnetic contrasts are schematically shown on the legends. Inset in (d) shows a zoom-in image of a multidomain nanoisland with contrast enhanced for visual clarity. MSFs were calculated by assuming an Ising model where CST islands possess zero net moment. Red scale bars are 2 μm. r.l.u., reciprocal lattice units, based on a square ASI lattice.*

Each unique combination of *a* and *W* has been listed in Table 3.1 and assigned a unique letter. The observed CST populations for each array are also listed in Table 3.1 and will be discussed in greater detail below. I note that for each ASI in Table 3.1, two duplicate arrays were fabricated at different regions on the same LSMO film.

TABLE 3.1. Geometric parameters and CST populations of brickwork ASI

ASI	Island width, *W* (nm)	Lattice parameter, *a* (nm)	Unique images acquired	Coupling strength, *J* (μA^2 m)	CST population (%)
A	100	650	4	0.59	0
B	100	600	4	0.75	0
C	125	650	4	0.91	0
D	125	600	4	1.15	0
E	150	650	3	1.27	0
F	150	600	2	1.62	0
G	175	650	4	1.69	9% ± 2%
H	175	600	4	2.15	0.5% ± 0.6%

Magnetic domain imaging was performed using X-PEEM using the PEEM-3 endstation at beamline 11.0.1.1 of the Advanced Light Source [93]. By using circularly-polarized X-rays, a magnetic signal can be acquired through X-ray magnetic circular dichroism (XMCD). The circularly-polarized X-rays were oriented in-plane along the $[\overline{11}]$ axis of the ASI with a 30° incidence angle relative to the sample surface. X-PEEM images were acquired at a photon energy corresponding to the maximum XMCD intensity at the Mn L_3 edge using right/left circularly polarized (RCP/LCP) X-rays. Other sources of contrast (i.e., local work function differences or topography) were minimized by performing an asymmetry calculation, $I = (I_{RCP} - I_{LCP}) / (I_{RCP} + I_{LCP})$, where I_{RCP} and I_{LCP} correspond to the pixel-wise intensities from images acquired using RCP/LCP X-rays, respectively. The XMCD contrast depends as $\cos(\theta)$ where θ is the angle between the nanoisland magnetization relative to the X-ray helicity vector since XMCD-PEEM images are sensitive only to the projection of the local magnetization onto the direction of the

incident X-ray beam [80]. X-ray absorption (XA) images, which possess information about the sample topography, were also produced by averaging the polarizations, $I = (I_{RCP} + I_{LCP}) / 2$. After a thermal demagnetization protocol, the sample temperature was set to 110 K to maximize the XMCD contrast and minimize thermally-induced magnetization evolution.

To analyze the images within the traditionally-utilized Ising framework, I developed an analysis routine based on the OpenCV implementation of the Earth Movers Distance used in image classification [94,95]. This routine automated the detection of nanoisland locations and magnetization directions. To quantitatively understand the *J*-dependent ordering behavior of the ASIs, the routine determined the populations of different vertex configurations (Figure 1(b)) which will be discussed in further detail below. Additionally, the routine determined the reciprocal space magnetic structure factors (MSF) of the ASI arrays, which is equivalent to a magnetic diffraction pattern of the ASI. MSFs were calculated by the method described by Östman *et al* [26]. For determining vertex types and MSFs, nanoislands with spin textures more complicated than single domains were assumed to possess a zero net moment.

Micromagnetic simulations were performed with MuMax^3 which calculates the lowest energy state of magnetic features in a ferromagnetic system using the Landau-Lifshitz-Gilbert equation and outputs a full vector field of the local magnetization that can be represented as a color map [62]. I have also processed the simulated magnetization vector fields to produce images that are representative of both the experimental geometry and resolution of the PEEM3 microscope. LSMO input parameters at ~110 K included the exchange stiffness, A_{ex}, = 3.6 pJ/m, saturation magnetization, M_{sat}, = 390 kA/m, and magnetocrystalline anisotropy constant, K_1, = 0 kJ/m^3 for magnetic nanoislands patterned using the ion-implantation based technique [58]. The simulated cell volume size was set to 2.5 × 2.5 × 40 nm^3 where I assumed uniform magnetization throughout

the nanoisland thickness. The lateral cell dimensions fell below the magnetostatic exchange length of $l_s = \sqrt{(2A_{ex})/(\mu_0 M_{sat}^2)} = 6.14$ nm. The region between the nanoislands were modeled to be empty space as the paramagnetic matrix between nanoislands in our ASIs possessed a permeability close to that of vacuum ($\mu_r \sim 1.1$) [23].

To examine the magnetic interactions of the nanoislands in the absence of any external magnetic fields, the ASIs were thermally annealed by heating the sample in the PEEM-3 endstation on a nonmagnetic sample holder to 350 K, which is above the experimentally-determined Curie temperature of the LSMO thin film ($T_C \sim 338$ K, ref [23]). The sample was subsequently cooled to the measurement temperature of 110 K at a rate of ~5 K/min [23]. The sample was thermally annealed twice *in-situ* at PEEM-3 and the ASI arrays were imaged after each annealing procedure. Since this sample contains two duplicates of each unique ASI, I collected 2-4 unique XMCD-PEEM images of the nanoisland magnetization (e.g., Figure 3.1(c-e)) for each ASI configuration which were used to calculate statistics. All error bars discussed in this work corresponds to the standard deviation between the XMCD-PEEM images.

3.3 – Results and Discussion

In XMCD-PEEM images, domains magnetized parallel, antiparallel, or perpendicular to the X-ray helicity appear as regions with black, white, or gray contrast, respectively. Our analysis routine automatically determined the nanoisland locations, magnetization directions, and vertex types from the XA/XMCD-PEEM images. The population of vertex types was used to quantitatively describe the magnetic configurations in ASI systems. Each three-nanoisland vertex in the brickwork ASI was classified based on its net dipolar interaction energy described Eq. 1.1. Out of the $2^3 = 8$ possible nanoisland magnetization directions available at each vertex, three sets of degenerate vertex-types exist (Figure 3.1(b)) that are labeled based on their relative energies

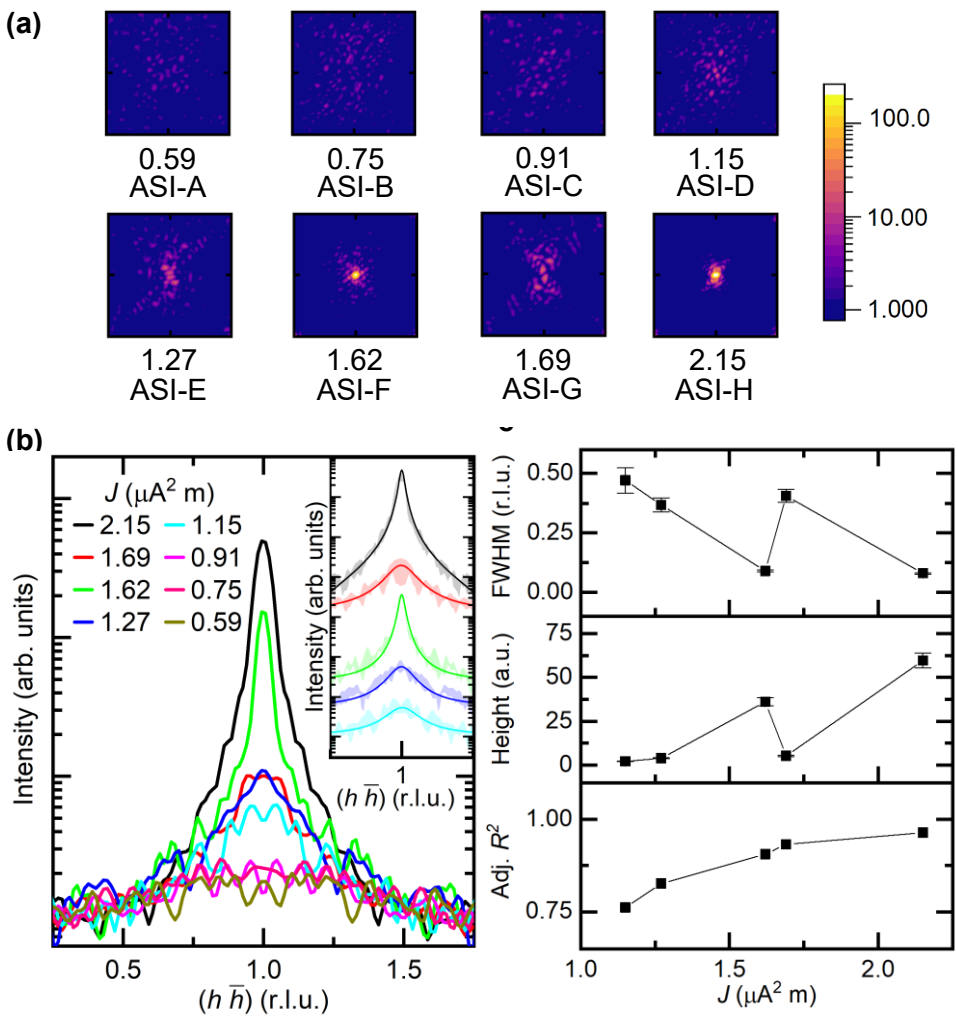

Figure 3.2: *(a) MSF of representative brickwork ASI at varying coupling strengths. Each panel is labeled with the corresponding ASI and J in units of μA² m. Each image shows the (1 1) peak and covers an area of $q_x,q_y \in [1/2, 3/2]$ r.l.u. For visual clarity, a logarithmic scale has been used. (b) MSF line scans across (1/4 $\bar{1}/\bar{4}$) to (7/4 $\bar{7}/\bar{4}$) with line width of 0.5 r.l.u. Each curve represents the mean intensity profile between MSFs from 2-4 XMCD-PEEM images of a given ASI. Inset figure shows Lorentzian function fits (solid lines) to the intensity curves at J = 2.15 μA² m to 1.15 μA² m, where the shaded regions represent the mean and standard deviation values. (c) Full-width at half-maximum (FWHM), peak height, and adjusted R^2 values extracted from the Lorentzian fits in (b). r.l.u., reciprocal lattice units.*

(i.e., $E_I < E_{II} < E_{III}$). Within the traditional Ising-framework, the prevalence of each vertex type depends on *J*. As shown in Figure 3.1(b), brickwork ASIs with small values of *J* (e.g., ASI-A) possessed randomized nanoisland magnetization directions and vertex population values representative of their multiplicities (i.e., 25% for Type I, 50% for Type II, 25% for Type III). As a consequence, the MSF of the disordered arrays possess weak and broadened peaks. As *J* increases (by increasing *W* or decreasing *a*), the ASIs established longer-ranged ordering characterized by extended stair-like steps with white or black XMCD contrast in Figure 3.1(c, e), increased population of Type I vertices, and sharp, well-defined peaks in the MSF (Figure 3.1(f, h)).

Figure 3.2 shows the *J*-dependent reciprocal space analysis conducted around the (1 1) magnetic structural peak. Qualitative inspection of the peaks suggests that the magnetic ordering in the CST-bearing ASI-G (1.69 μA^2 m) is similar in nature to the fully-Ising ASI-E (1.27 μA^2 m). This behavior becomes more apparent in the experimental line scans and corresponding Lorentzian fits in Figure 3.2(b) where the two *J* values (red and blue lines) demonstrate the greatest similarity. By characterizing these fitted profiles using the full-width at half-maximum and the peak height, I also find excellent quantitative agreement between the two *J* values.

Analysis of the XMCD-PEEM images indicated that nanoislands in ASI-A through -F were all single domain states while nanoislands in ASI-G and -H possessed a majority Ising-like nanomagnets and a small percentage of CSTs which are assigned to have zero-net moment in statistical and MSF calculations. Only 0.5% ± 0.6% of the nanoislands in ASI-H formed CSTs while 9% ± 2% were observed in ASI-G with nearly identical population across all four images acquired. Consequently, 25% ± 5% of the vertices in ASI-G were flanked by CST-bearing

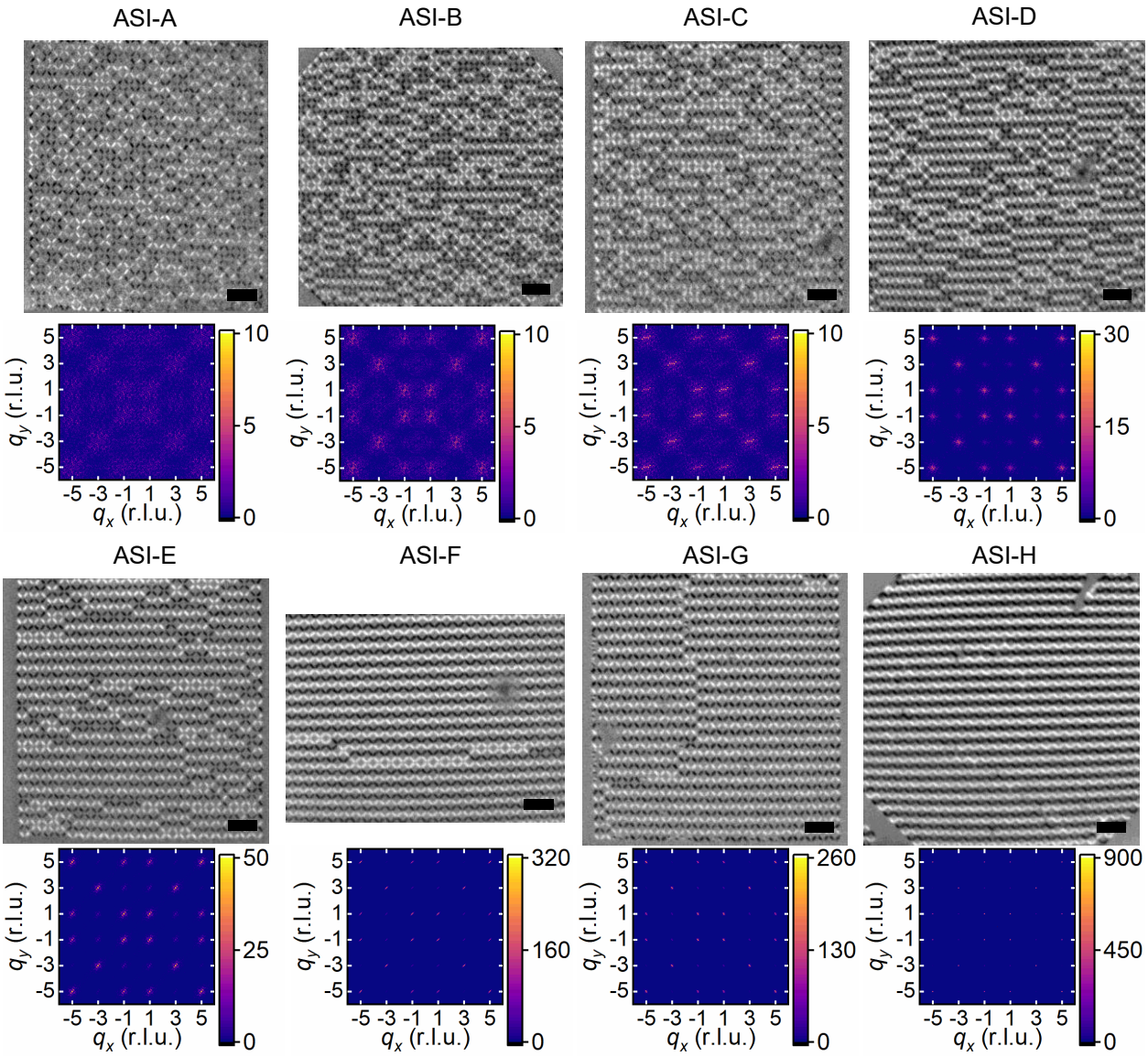

Figure 3.3. *XMCD-PEEM images and corresponding MSF of representative square ASIs at varying J. Each MSF image covers an area of $q_x,q_y \in [-6, 6]$ r.l.u. Scale bars are 2 μm.*

nanoislands and could not be classified as a Type I-III vertex, in comparison to 2% ± 2% of the vertices in ASI-H.

CST formation in LSMO-based ASIs depends strongly on the local geometric environment. In ASI-G (i.e., ASI with largest CST abundance), ~ 95% of CST-bearing nanoislands were vertically oriented. Conversely, square ASI arrays (i.e., the parent configuration of brickwork

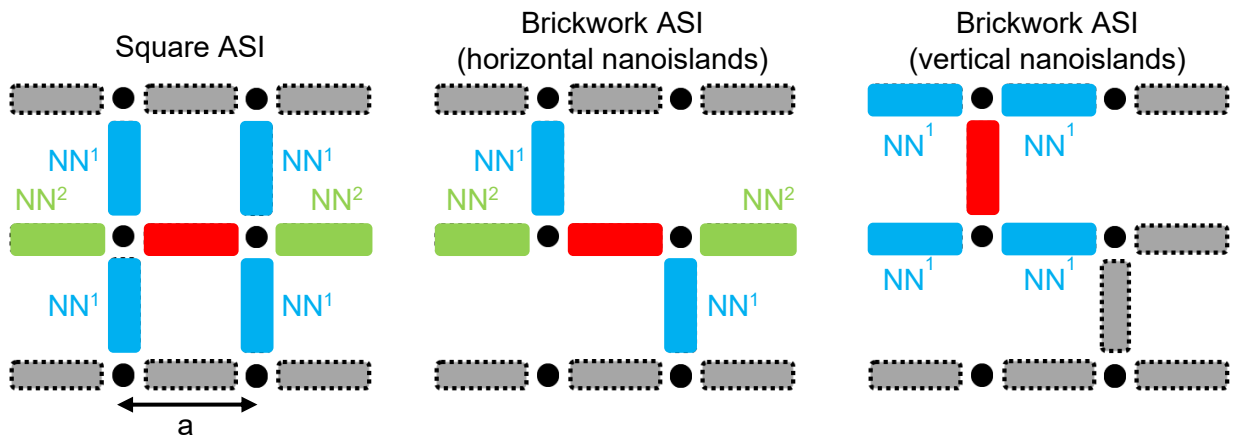

Figure 3.4: *First- (NN^1, blue rectangles) and second-nearest neighbor (NN^2, green rectangles) diagrams for reference nanoislands (red rectangles) in square ASIs and brickwork ASIs that are vertically- or horizontally-oriented. Black dots represent the ASI vertices, spaced apart by the ASI lattice parameter a. For both brickwork and square ASIs, the center-to-center distance between the reference nanoisland and NN^1 or NN^2 nanoislands are $a/\sqrt{2}$ and a, respectively.*

ASI without the removal of select nanoislands) with identical island size and ASI lattice spacing possessed only ~ 1% CSTs (Figure 3.3) on the same LSMO thin film sample as in this study, as well as in an identical square ASI studied in Ref. 25. Note that the labels assigned to square ASIs in Figure 3.3 correspond with *a* and *W* values listed in Table 3.1. The LSMO-based square ASIs exhibit ordering behaviors expected for this system, where increasing *J* (either through *W* or *a*) monotonically increases the extent of long-range ordering in the ASIs as characterized both visually in the XMCD PEEM images (i.e., long rows of black/white nanoislands) and in the MSF maps (i.e., peaks become narrower and more intense).

While each nanoisland in square ASIs possessed identical nearest neighbor configurations, in brickwork ASIs, the vertical [01]-oriented and horizontal [10]-oriented nanoislands differed in their nearest neighbor configurations and, thus, were subjected to distinct dipolar interaction environments. As shown in Figure 3.4, the horizontal brickwork ASI nanoislands possessed first-

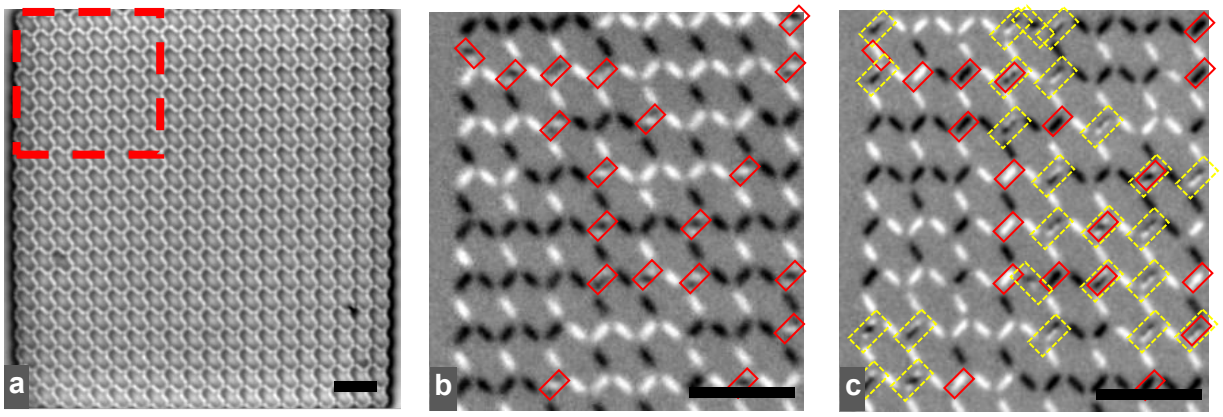

Figure 3.5. *(a) XA PEEM image of an ASI-G brickwork array. XMCD-PEEM images of the boxed region in (a) before (b) and after (c) a repeated in-situ room temperature demagnetization procedure. Red and yellow boxes in (b-c) correspond to CST locations before and after demagnetization, respectively. Scale bars are 2 μm.*

(NN^1) and second-nearest neighbor (NN^2) nanoislands that were similar in their geometric environment compared to those found in the parent square ASI. The NN^1 and NN^2 nanoislands surrounded the same vertices as the reference nanoisland with either perpendicular or parallel orientation, respectively. In comparison, the vertical nanoislands in brickwork ASIs were only flanked by perpendicularly-oriented NN^1 nanoislands. This correlation between nearest-neighbor configurations and CST formation probabilities demonstrates the sensitivity of CST formation on the local geometric environment, which therefore influenced the local dipolar interactions.

To ensure that the presence of CSTs is not purely attributed to lithographical defects, I first inspected the ASI topography in an XA PEEM image shown in Figure 3.5(a). No obvious differences in terms of nanoisland size, spacing, or edge imperfections were observed other than the black spot in the bottom right corner and these nanoislands have been treated as possessing zero net moment in the analysis. I also performed XMCD PEEM imaging of a brickwork ASI-G before (Figure 3.5(b)) and after (Figure 3.5(c)) an *in-situ* thermal demagnetization procedure. The

red boxes correspond to the locations of CSTs before demagnetization while the yellow boxes indicate CST locations after demagnetization. As shown in Figure 3.5(c), CSTs were not solely confined to certain nanoislands as 14/19 nanoislands in the red boxes possessed Ising states after demagnetization. After demagnetization, 25 nanoislands possessed CSTs, 5 of which are common to the state before demagnetization (i.e., Figure 3.5(b)). Additionally, only 1/5 of those common nanoislands was observed to possess the same exact CST after demagnetization. This analysis of XA-PEEM images indicates that local changes in the nanoisland shape or dipolar coupling due to lithographic errors can be ruled out as factors inducing CST formation. Furthermore, similar CST formation behavior has been observed in ASIs patterned in subsequent LSMO-based samples using similar widths and lattice spacing. Therefore, the behavior of ASI-G can be considered to be inherent to this system with its unique combination of a and W values as well as nanoisland geometry, and not an anomaly within a particular sample or individual defects.

Unlike ASI-F (Figure 3.1(c)) and -H (Figure 3.1(e)) which both demonstrated long-range magnetic ordering, images of ASI-G (Figure 3.1(d)) showed a stark reduction in long-range magnetic ordering with only small patches of the low energy ground-state Ising configuration. This observable change in the real-space magnetization ordering in ASI-G also corresponds to peak broadening and an order of magnitude reduction in peak intensity in the MSF (Figure 3.1(g) and Figure 3.2). Furthermore, an abrupt deviation in Type I vertex population was observed only in ASI-G in Figure 3.1(b), which may be associated with both the reduction of long-range ordering and the inability to apply the Ising model to vertices with CST nanoislands.

The XMCD-PEEM images suggest the presence of two types of CST observed in ASI-H and -G. These CST appeared as three (Figure 3.6(a)) or two (Figure 3.6(b)) regions with alternating contrast separated by transition regions of ~50 nm in width oriented along the ASI [11] axis. Kim

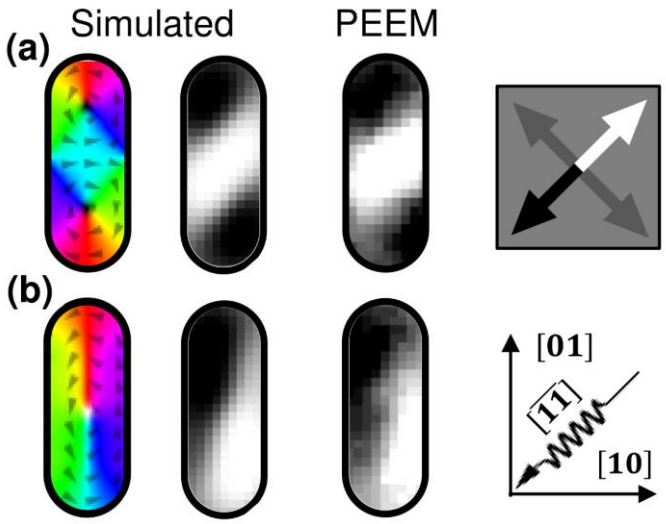

Figure 3.6*: (a, b) Simulated (left and center) and XMCD-PEEM (right) images of the double (a) and single (b) vortex spin textures. The colored regions in the vector field map (left) represent the in-plane component of the magnetization (also indicated by the arrows). The simulated XMCD images in the center have been processed to reflect both the experimental geometry and resolution (see text for processing details). The contrast in both PEEM and simulated XMCD images were enhanced for visual clarity. Schematics of the experimental geometry and associated magnetic contrast for both PEEM and simulated images are shown in the far right.*

et al. investigated similarly-sized rectangular and elongated hexagonal LSMO nanoislands and suggested that these spin textures corresponded to flux-closure states when taking into account the limited lateral resolution of the PEEM-3 microscope for complex oxide samples [60]. MuMax[3] micromagnetic simulations, [62] with Gaussian blurring to simulate actual experimental resolution limits, confirmed that the XMCD-PEEM contrast pattern can arise from the magnetization projection of single- and double-vortex spin textures as shown in Figure 3.6. The gradual rotation of the local magnetization in such CSTs is consistent with a magnetic material with minimal magnetocrystalline anisotropy, as is the case with these LSMO nanoislands patterned through ion implantation [58].

The formation of spin textures in isolated magnetic nanoislands is typically explained as a balance between magnetostatic (E_{MS}), exchange (E_{ex}), and magnetocrystalline anisotropy (E_{mca}) energies. For the elongated stadium-shaped nanoislands studied in this work (aspect ratios ranging from 1:4.7 in ASI-A and -B to 1:2.7 in ASI-G and -H), E_{MS} was expected to dominate leading to single-domain magnetic configurations. The presence of CSTs in ASI-G and -H (W = 175 nm) and their absence in ASI-A through -F ($W \leq 150$ nm) can be partially explained by considering *intra*-island energetics: As W increases, the tendency to form vortex-like states also increases since (1) E_{MS} of a single-domain state increases with greater nanoisland volume, and (2) the E_{ex} penalty for formation of a vortex state (~50 eV from micromagnetic simulations) becomes smaller than the total reduction in E_{MS}.

However, *intra*-island energetics alone do not explain how a values influenced CST formation. Our experimental results suggest that shape anisotropy alone may be insufficient to fully predict spin texture formation in ASI arrays and I must consider the competition between *inter*-island effects (i.e., dipolar interactions) and *intra*-island effects (e.g., shape anisotropy and exchange energy). To this end, I used MuMax[3] micromagnetic simulations to calculate the energies of relaxed nanomagnetic states shown schematically as Figure 3.7(a) as a function of a, W, Ising magnetization of the first nearest neighbors, M_{NN}, and center island magnetization, M_{Center}.[7] The variations in a (95 nm $\leq a \leq$ 200 nm) and W (595 nm $\leq W \leq$ 705 nm) were performed in increments of 5 nm. M_{NN} was initialized to possess uniform magnetization that reflect the magnetization configurations observed around CSTs in XMCD-PEEM images. M_{Center} was initialized to possess either an Ising state or a CST state with a single- or double-vortex. The different configurations of the five-island unit in Figure 3.7(a) are referred to as "Ising" or "CST states" depending on the magnetization state of M_{Center}.

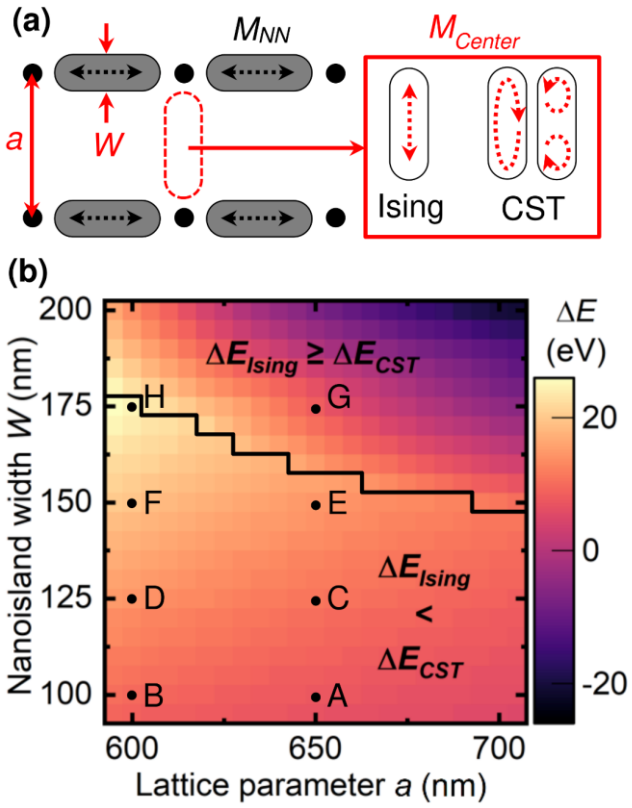

Figure 3.7: *(a) Schematic of the five-island unit simulated to determine the relative energies when the red center nanoisland takes on an Ising or CST state (i.e., single or double vortex). Each nearest neighbor magnetization (M_{NN}) can have two possible orientations. (b) Minimum energy surface calculated relative to a configuration with two Type I vertices, $E_{Dual\ I}$ (equation 2). The black line separates the regions where the minimum ΔE is associated with an Ising M_{Center} ($\Delta E_{Ising} < \Delta E_{CST}$) or a CST M_{Center} ($\Delta E_{Ising} \geq \Delta E_{CST}$). Letters correspond to the ASI configurations listed in Table 3.1.*

To compare the relative energies between CST and Ising states, I calculated the energy difference ΔE of the total energy (E) relative to a configuration consisting of two Type I vertices, $E_{Dual\ I}$, as

$$\Delta E = E(a, W, M_{NN}, M_{Center}) - E_{Dual\ I}(a, W) \qquad \text{Eq. 3.1}$$

$E_{Dual\ I}$ was found to be the ground state energy for the range of a and W values used in our XMCD-PEEM experiments. Figure 3.7(b) plots the minimum value of ΔE as a function of a and W. The black border separates the energy surface into two regions where the minimum ΔE was associated with an Ising state ($\Delta E_{Ising} < \Delta E_{CST}$) or a CST state ($\Delta E_{Ising} \geq \Delta E_{CST}$). Figure 3.7(b) shows that an intermediate range of a (595 nm $\leq a \leq$ 705 nm) and W (95 nm $\leq W <$ 150 nm) exists where the formation of Ising states was preferred over CSTs. For larger values of a and W above the black border, CST states became energetically favorable over an arrangement of Ising states in high energy Type II and III vertex configurations. Energetic analysis demonstrated that E_{MS} (~100 eV) dominated over E_{ex} (~ 10 eV) and that CST states became energetically preferred over Ising states only when the reduction in E_{MS} exceeded the E_{ex} penalty of ~50 eV. While E_{MS} depends on W which influences the *intra*-island energetics of isolated nanoislands as discussed earlier, in ASIs, E_{MS} is also influenced by a which changes the dipolar interactions of the full array. For nanoislands experiencing attracting ("heads-to-tails") interactions, as is the case for the minimum ΔE states, E_{MS} increases with a [96,97]. However, E_{MS}, and thus ΔE, demonstrated stronger dependence on W compared to a, where E_{MS} saturated as $a \rightarrow \infty$ (i.e., nanoislands become fully isolated).

By overlaying the ASI configurations in Table 3.1 over Figure 3.7(b), I found a correlation between the CST populations observed in XMCD-PEEM images and the M_{Center} state associated with the minimum ΔE. For ASI-A through -F, CSTs were absent in the arrays and were predicted to favor Ising states over CST states ($\Delta E_{Ising} < \Delta E_{CST}$). ASI-G sits well inside the region where CST states are preferred over Type II and III formation ($\Delta E_{Ising} > \Delta E_{CST}$) and possessed the highest CST population of 9% ± 2%. ASI-H resides on the border separating the two energy regions and displayed a small CST population (0.5% ± 0.6%). This correlation between the CST populations and the associated energetic preference of Ising or CST states suggests that our micromagnetic

model captures the fundamental aspects of spin texture energetics in LSMO-based brickwork ASI. This correlation also suggests the possibility for using *a*- and *W*-values within the CST-preferred region ($\Delta E_{Ising} > \Delta E_{CST}$) to investigate the kinetics of CST-Ising domain formation and ASI magnetic ordering, which can be achieved by annealing our LSMO-based ASIs below its experimentally-determined $T_C \sim 338$ K (ref [23]). Additionally, I anticipate that the application of an external magnetic field (i.e., introducing Zeeman energy into our model) may change the border location in our phase diagram as a function of field strength and direction. For instance, the border may move upwards (more *a*- and *W*-values favoring Ising states) with increasing field strength along the ⟨11⟩ directions as the ASI nanoislands become saturated. Both temperature- and field-dependent studies of spin texture energetics and kinetics would provide greater insights into how specific domain states populations can be engineered in LSMO-based ASIs.

3.4 – Conclusions

In conclusion, using a combination of XMCD-PEEM imaging and micromagnetic simulations, I demonstrated that the formation of CSTs in LSMO-based ASIs could be tuned through the balance of both the island aspect ratio and dipolar interaction based on the configuration and spacing of the nearest neighboring nanoislands. Energy analysis suggests that while the magnetostatic energy dominates the *a*- and *W*-dependent energetics, the small contribution from exchange energy determines whether nanoislands will preferentially form Ising or CST states. Additionally, the nanoisland magnetic state changes the magnetostatics arising from both *intra*-island shape anisotropy and *inter*-island dipolar interaction. These tunable nanoisland domain states provide opportunities for introducing exotic phase transitions in existing and unexplored ASI arrays which take into account the additional ways that the nanoislands interact [1]. Furthermore, the observation of tunable CST formation in LSMO-based ASIs arises

from a special balance between the inter- and intra-island energetics, which are enabled by the LSMO magnetic parameters. Our findings highlight the potential for materials-driven ASI studies to provide deeper insights into ASI and domain formation physics. These studies could involve ASIs patterned into complex oxide thin films and heterostructures to investigate exchange interactions in ferromagnetic/ferromagnetic (e.g., $La_{0.7}Sr_{0.3}CoO_3$/LSMO [98,99]) or antiferromagnetic/ferromagnetic ($La_{1-x}Sr_xFeO3$/LSMO [86,87]) interfaces, strain-controlled magnetism in ferroelectric/ferromagnetic systems (e.g., $BaTiO_3$/LSMO [100]), or optically-tunable ferromagnetism in LSMO coated with the halide perovskite $CH_3NH_3PbI_3$ [101].

Chapter 4: Energetics of Ising-Vortex Interactions in $La_{0.7}Sr_{0.3}MnO_3$ Brickwork Artificial Spin Ices

4.1 – Introduction

Spatial arrangement of spins, known as spin textures, have served as a basis for investigations into developing spin-based memory and computing devices [65,68,69,102]. The operation of such devices depend on the ability to stabilize specific types of spin textures such as single domains (i.e., uniform magnetization) [10,64,103], domain walls [69], vortices [104], and skyrmions [67,105]. The formation of spin textures is generally understood by considering the balance of energetics in the magnetic body [61]. That is, the observed spin texture results from a balance between energy terms associated with magnetic effects such as stray field production (magnetostatic energy, E_{ms}) and preference for the magnetic moments to align parallel with each other (exchange energy, E_{ex}) and along crystallographic easy axes (magnetocrystalline anisotropy energy, E_{mca}). The energetics of a given spin texture not only depend on the magnetic properties of the sample material, but also on the sample shape. This behavior is exemplified in magnetic thin films patterned into micro- and nano-sized structures, where spin texture formation can be controlled through the shape and size of the patterned geometries [60,64,65,106–108]. In epitaxial thin films, an additional control parameter comes in the form of the relative orientation between the micromagnet shape and the crystallographic easy axes [58,60].

Spin texture formation has also been investigated in ensembles of lithographically-defined interacting nanoislands known as artificial spin ices (ASIs) [65,109–111], which can provide insights into how dipolar interactions between nanoislands can influence spin texture formation. Traditionally, ASIs were designed to reproduce spin ice physics using an array of nanoislands with Ising-like single domain states [1,2]. In recent years, it has been shown that ASIs can be designed

to allow the formation of Ising domains and complex spin textures (CSTs), such as vortices [65,109–111]. Several studies of CST formation have subjected the ASIs to a magnetic field protocol [65,110,111]. While these studies revealed how Ising and CST formation depends on the simultaneous influence of the dipolar interaction and applied magnetic field, it is also of interest to understand how dipolar interactions *alone* can control the types of spin textures observed. Such an experiment can be facilitated through the use of a thermal annealing protocol (e.g., heating the sample above its Curie temperature, T_c, then cooling down to the desired measurement temperature) to allow the nanoislands to self-establish a low energy spin texture configuration.

ASIs fabricated from the ferromagnetic complex oxide LSMO can facilitate such studies owing to their near room temperature $T_c \sim 370$ K and chemical stability up to ~870 K in both ambient and vacuum environments [23,109]. Using this system, I demonstrated in Chapter 3 that spin texture formation depends on both the nanoisland geometry, controlled by its width W, and the lattice geometry, defined by the type of lattice used (e.g., square, brickwork) and its lattice parameter a. That is, the preference for CST or Ising domains to form depends on geometric control of both the nanoisland shape anisotropy *and* the interisland dipolar interactions. An understanding of spin texture formation in LSMO brickwork ASIs was provided through an energy analysis of micromagnetic simulations using the I-shaped nanoisland arrangement shown in Figure 4.1(c) [109]. This arrangement was chosen as CSTs in Chapter 3 were observed to preferentially form in the center nanoisland of the five-island arrangement (e.g., Figure 4.1(a, b)). Micromagnetic simulations were performed on this structure as a function of the geometric variables (a and W) as well as the spin texture states of the center (M_{center}) and horizonal nearest neighboring nanoislands (M_{NN}) (see Figure 4.1(c)). By calculating the energy difference ΔE of the total energy E relative to

the lowest-energy Ising configuration, $E_{\text{dual I}}$, through Equation 3.1, an a- and W-dependent phase diagram was constructed using the minimum ΔE surface. From this diagram, it was shown that the energetic preference of forming CST configurations over Ising configurations can be tuned as a function of a and W.

While Chapter 3 explores how spin texture formation depends on the *geometric* dependence of the dipolar interaction, in this work I show how these spin textures also correlate with the magnetization of adjacent nanoislands for *both* Ising and CST domains. By first investigating the energetics and stray fields of *isolated* nanoislands, an understanding of how single and double vortex CSTs magnetostatically interact with adjacent nanoislands is developed. Through this stray field analysis, I find that the tips of CSTs can be approximated as effective Ising-like dipoles that are oriented perpendicular to the nanoisland length. I use this approximation to analyze interactions between Ising- and CST-bearing nanoislands within an Ising framework to calculate the magnetostatic correlation which quantifies the number of head-to-tail interactions in the set. Through an energy analysis of micromagnetic simulations, the magnetic configuration of the nearest neighboring nanoislands (i.e., M_{NN}) was observed to induce energy splitting between the two chiralities of a single or double vortex domain. Moreover, this M_{NN}-induced energy splitting can be predicted through a correlation analysis which identifies the chiral state that maximizes the number of attracting nearest-neighbor interactions at the ASI vertices. Finally, by analyzing the magnetic domain images acquired with x-ray photoemission electron microscopy (X-PEEM) for Chapter 3, I observed preferential CST chirality formation in M_{NN} which induces energy splitting.

4.2 – Methods

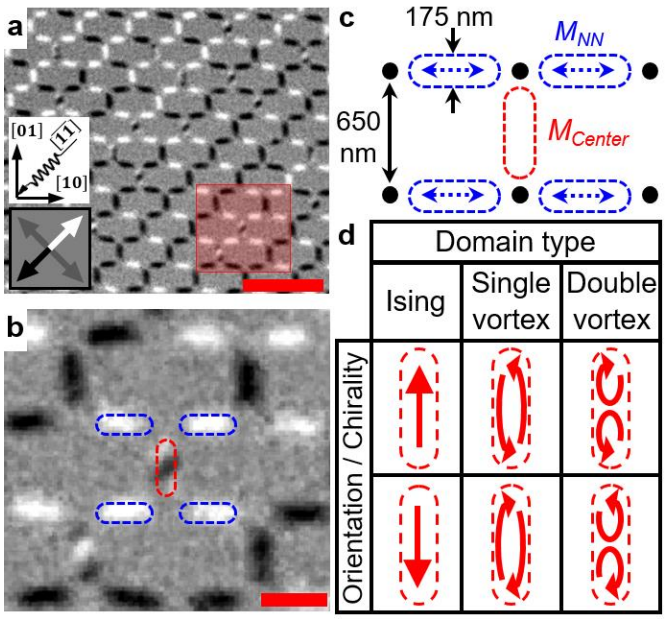

Figure 4.1: *(a) Representative XMCD PEEM image of a brickwork ASI. Scale bar is 2 μm. The experimental geometry and associated magnetic contrasts are schematically shown in the legends. (b) A zoom-in image of the boxed red region in (a). Scale bar is 500 nm. (c) Schematic of the I-shaped nanoisland arrangement simulated to determine the relative energies as a function of the spin texture inside the center red island (M_{NN}) and the Ising configuration (blue arrows) of the first nearest neighboring blue islands (M_{NN}). This arrangement of nanoislands is shown in (b) with the nanoislands outlined in red and blue. (d) Schematics of the spin textures that M_{center} can possess. The six M_{center} states are distinguished by their domain type (Ising, single vortex, or double vortex) and orientation/chirality.*

A 40-nm thick LSMO film was grown epitaxially on a (001)-oriented Nb-doped $SrTiO_3$ (0.05 wt % Nb) substrate using pulsed laser deposition with a laser fluence of approximately 1 J cm^{-2} and a frequency of 1 Hz. During the growth, the substrate temperature was held at 700 °C with an oxygen pressure of 300 mTorr. Postdeposition, the film was slowly cooled to room

temperature in 300 Torr O_2 to ensure proper oxygen stoichiometry. Structural characterization was performed with x-ray reflectivity and x-ray diffraction to confirm the film thickness, coherent growth, and crystalline quality (for details, see Ref. [23]). ASI arrays containing over 900 stadium-shaped nanoislands (rectangles with semicircle endcaps) were defined in different regions of a single LSMO film using a patterning technique based on electron beam lithography and Ar ion implantation [59]. The nanoislands had fixed lengths, L, of 470 nm and widths, W, of 175 nm. The nanoisland lengths, which lie along the two-dimensional ⟨10⟩ axes of the ASI in Figure 4.1(a), were aligned with the in-plane ⟨110⟩ easy axes of the LSMO film. The spacing between the ASI lattice points (black dots in Figure 4.1(c)) was set to 650 nm.

Magnetic domain imaging was performed using X-PEEM at the PEEM-3 endstation at beamline 11.0.1.1 of the Advanced Light Source [93]. By using circularly-polarized x-rays, the local magnetization orientation was imaged through x-ray magnetic circular dichroism (XMCD) [80]. The x-ray beam was oriented at a 30° grazing incidence with respect to the sample surface. The projection of the x-ray beam on the film surface was oriented along the two-dimensional $[\overline{11}]$ direction of the ASI (see legend in Figure 4.1(a)). X-PEEM images were acquired at a photon energy corresponding with the maximum XMCD signal at the Mn L_3 edge using left-/right-circularly polarized (LCP/RCP) x-rays. To minimize other sources of contrast (i.e., topography or local work-function differences), XMCD PEEM images were calculated using an asymmetry calculation, $I = (I_{RCP} - I_{LCP})/(I_{RCP} - I_{LCP})$, where I_{RCP} and I_{LCP} correspond to the pixel-wise intensities from X-PEEM images acquired using RCP and LCP x-rays, respectively. The XMCD signal is sensitive only to the projection of the local magnetization onto the direction of the x-ray beam and scales with $\cos(\theta)$, where θ is the angle between the local magnetization and the x-ray helicity. The sample was mounted on a nonmagnetic sample holder and thermally

annealed at 350 K, which was above the experimentally-determined Curie temperature of the LSMO thin film (T_C ~ 338 K, Ref. [23]). Subsequently the sample was cooled to a measurement temperature of 110 K at a rate of approximately 5 K/min. The measurement temperature of 110 K maximized the XMCD contrast and minimized thermally induced magnetic evolution. The sample was thermally annealed twice *in-situ* in the PEEM-3 microscope and imaged after each annealing and cooling procedure. Since the sample contained two duplicate ASI arrays, a total of four unique XMCD PEEM images of the nanoisland magnetizations were acquired to calculate statistics [109]. For clarity, the XMCD PEEM images shown in Figure 4.1(a) and (b) were processed using an unsharp mask with a 3 pixel radius and 0.5 mask weight.

Micromagnetic simulations were performed with MuMax^3 which calculates the lowest energy state of magnetic features in a ferromagnetic system using the Landau-Lifshitz-Gilbert equation and outputs a full vector field of the local unit magnetization, $\boldsymbol{m}$, that can be represented as a color map [62]. LSMO input parameters at ~110 K included the exchange stiffness, $A_{ex,}$ = 3.6 pJ/m, and saturation magnetization, $M_{sat,}$ = 390 kA/m. The magnetocrystalline anisotropy constant, K_1, was set to 0 kJ/m^3 [58,109]. The region between the nanoislands was modeled to be empty space as the paramagnetic matrix between nanoislands in our ASIs possessed a permeability close to that of vacuum (μ_r ~ 1.1) [23]. In our simulations, the lateral cell dimensions were set to 2.5 x 2.5 x 40 nm^3, where I assumed a uniform magnetization throughout the nanoisland thickness. The lateral cell dimensions fell below the magnetostatic exchange length of 6.14 nm. I simulated both isolated nanoislands and the I-shaped nanoisland arrangement shown in Figure 4.1(c). The nanoislands had stadium-shaped geometries with dimensions consistent with those used in our XMCD PEEM experiments (i.e., heights of 40 nm, L = 470 nm, W = 175 nm, and ASI lattice spacing of 650 nm). These combinations of geometric parameters and nanoisland arrangement

were chosen as vortices appeared in the greatest abundance at the center nanoisland of the I-shaped structure as shown in Figure 4.1(a, b) [109]. For studies of isolated nanoislands, W was varied from 95 nm $\leq W \leq$ 200 nm in 5 nm increments.

The magnetizations of the center nanoisland, M_{Center}, and nearest-neighboring nanoislands, M_{NN}, were defined at the beginning of each simulation. As shown in Figure 4.1(d), M_{center} is defined by the type of domain present (Ising, single, or double vortex) and the orientation/chirality of those domains. The M_{NN} nanoislands possess only Ising domains and are configured into four energetically unique arrangements labeled as C1-C4 in Figure 4.3(e). These configurations correspond with the M_{NN} observed experimentally in XMCD PEEM images. For each configuration, all Ising nanoislands were set to have uniform magnetization. The single vortex domain was defined using the vortex function in MuMax^3. The double vortex domain was initialized by initializing vortices with opposite chirality in each half of the nanoisland. After defining M_{NN} and M_{center}, the magnetizations were allowed to relax to the lowest energy (meta)stable state. The ParaView software package was used to process the MuMax^3-generated $\boldsymbol{m}$-maps and visualize their magnetization gradients, $||\boldsymbol{\nabla m}||$, and magnetization divergences (i.e., pole densities), -div($\boldsymbol{m}$), in Figure 4.2(d, e) [112]. I also used ParaView to trace out field lines from MuMax^3-generated stray field vector maps (Figure 4.3(a-c)).

4.3 – Results and Discussion

To understand spin texture formation in *interacting* nanoisland arrays, I first investigated the energetics of *isolated* nanoislands as a function of W and the type of domain present. The type of spin texture observed depends on a balance between multiple energy terms such as the exchange (E_{ex}) term, which favors parallel $\boldsymbol{m}$ alignment in ferromagnets (i.e., gradient $||\nabla \boldsymbol{m}|| = 0$), and magnetostatic ($E_{ms}$) term, which favors stray field ($\boldsymbol{H}_s$) minimization. These stray fields are

produced by divergent magnetizations (div($\boldsymbol{H_s}$) = -div($\boldsymbol{m}$)) which are referred to as magnetic poles. Lee *et al.* demonstrated in Ref. [58] that the spin textures in LSMO-based micromagnets can be simulated by defining values for the magnetic parameters A_{ex}, M_{sat}, and K_1 such that only the exchange energy, E_{ex}, magnetostatic energy, E_{ms}, and magnetocrystalline anisotropy energy, E_{mca}, were defined, respectively. Furthermore, the domains observed in their XMCD PEEM studies were best reproduced in micromagnetic simulations by modeling K_1 to vanish approximately 300 nm away from the micromagnet edges due to the lateral strain imposed on the micromagnets through the ion implantation-based patterning process which is also used for this work [58].

Figure 4.2(a-c) shows the width-dependence of the magnetic energies for different types of spin textures. Increasing W from 100 nm to 200 nm causes the volume of the nanoisland to increase. For Ising domains, E_{ms} grows with increasing W while E_{ex} is independent of W as the nanoisland maintains an macrospin-like state across the range of W values studied. However, for single and double vortex domains, both E_{ms} and E_{ex} decrease with increasing W. While the E_{ex} curves for the different domain types in Figure 4.2(a) do not intersect within the range of W studied, Figure 4.2(b) shows that E_{ms} for single and double vortex domains may exceed those of Ising domains when $W \leq 115$ nm. The combined W-dependence of E_{ex} and E_{ms} is reflected in the total energy shown in Figure 4.2(c) which shows that Ising domains are favored when $W \leq 150$ nm while CSTs are favored when $W > 150$ nm. Close inspection of Figure 4.2(c) shows that, within the range 150 nm $< W \leq 195$ nm, the double vortex domain is favored while single vortex domains are favored for $W > 195$ nm.

The origin of the W-dependent energetics in CSTs can be understood by considering how the spin texture changes with W. Figure 4.2(d, e) shows maps of $\boldsymbol{m}$ along with calculated gradients and pole densities for single (Figure 4.2(d)) and double (Figure 4.2(e)) vortex domains for W =

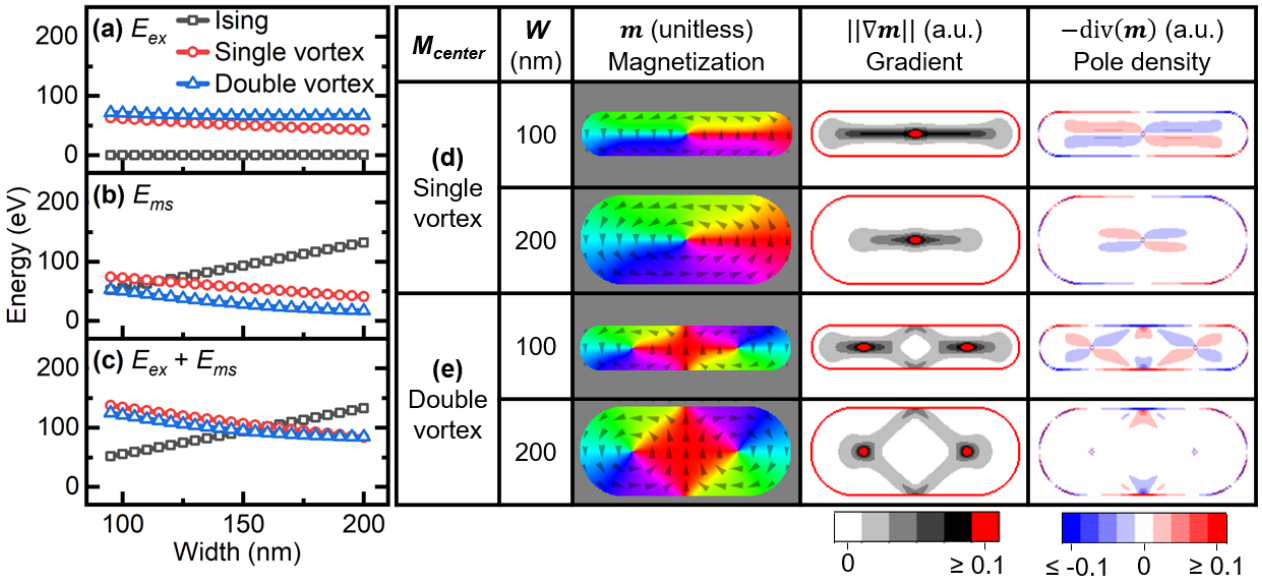

Figure 4.2: *(a) Exchange, (b) magnetostatic, and (c) total energy of isolated nanoislands simulated as a function of nanoisland domain type and width W. The nanoisland length, L, was fixed to 470 nm. Maps of the local unit magnetization m and corresponding gradient magnitudes and divergence (i.e., pole densities) for (d) single and (e) double vortex domains. The color bars for the gradient magnitude and pole densities are scaled linearly. a.u. arbitrary units.*

100 nm and 200 nm. For both CSTs, the gradient maps show that W = 100 nm produces larger areas of higher gradients (larger dark areas) compared to W = 200 nm. This behavior indicates that as W is reduced from 200 nm to 100 nm, the rotation of the local magnetization is forced to curl more sharply within the nanoisland in order to form its single or double vortex topology. The associated pole density maps show similar trends where nanoislands with W = 100 nm contains larger areas with higher pole densities (blue/red regions) compared to nanoislands with W = 200 nm. In other words, the pole density maps suggest that single and double vortex CSTs will produce more stray fields (i.e., increase E_{ms}) as W decreases from 200 nm to 100 nm.

While Figure 4.2(c) implies that CSTs should be observed as long as $W > 150$ nm, this result neglects the energetic contribution from *inter*island magnetostatic interactions [109]. To understand how the nanoisland magnetizations influence the energetics in brickwork ASIs, I analyzed the five nanoisland arrangement shown in Figure 4.1(c) as a function of M_{center} and M_{NN} at a fixed geometry of $a = 650$ nm and $W = 175$ nm. In Ref. [109], these values of a and W were associated with the largest CST populations observed in LSMO-based brickwork ASIs within the range of a and W studied. To account for energy variations associated with the extent of the curling of magnetization at the tips of Ising domains, I performed two types of simulations: (1) all nanoisland spin textures were allowed to relax and (2) all nanoisland textures *except* Ising domains were allowed to relax.

Figure 4.3(e) shows a table where each cell in the table (separated by thick black lines) contains the ΔE band diagrams for each unique combination of M_{NN} (table rows) and M_{center} domain type (table columns) simulated in this work. The two ΔE bands within each cell corresponds with the two orientations for Ising domains (i.e., up or down states) or the two chiral states for CSTs. The ΔE bands for these two states are colored light or dark gray if they are degenerate or split into two different energy bands, respectively. The lower and upper bounds of each energy band correspond with ΔE calculated from simulations (1) and (2), respectively.

For Ising M_{center}, the relative energies between up and down states depend on which M_{NN} is present. This result can be understood by treating each nanoisland as a dipole and counting the amount of attracting "head-to-tail" (reduce E_{ms}, blue box in Figure 4.3(d)) or repelling (increase E_{ms}, red box in Figure 4.3(d)) "head-to-head" or "tail-to-tail" pair-wise interactions present. If flipping M_{center} does not change the number of attracting interactions produced, then the up and

down states will be two-fold degenerate. Otherwise, the two orientations will be split into high (maximum repulsion) and low energy (maximum attraction) states.

To compare the interaction changes produced by the up and down states for a given M_{NN}, I first define a correlation constant C_{ij} to quantitively classify attracting and repelling nanoisland interactions as $C_{ij} = +1$ and $C_{ij} = -1$, respectively. Figure 4.3(d) schematically shows C_{ij} values for all Ising (left column in Figure 4.3(d)) or Ising-CST (right column in Figure 4.3(d)) nearest-neighboring interactions. As will be discussed later, Ising-CSTs interactions can be analyzed within this framework by modeling CSTs with effective Ising-like dipoles with their magnetizations perpendicular to the nanoisland length. I then calculated the average correlation $\langle C_{ij} \rangle$ for different combinations of M_{center} and M_{NN} as

$$\langle C_{ij} \rangle = \sum_{j=1}^{4} C_{ij} / 4 \qquad \text{Eq. 4.1}$$

where i represents the M_{center} nanoisland and j corresponds with the four nanoislands which comprise M_{NN}. The values of $\langle C_{ij} \rangle$ are shown in Figure 4.3(e) as color-coded red ($\langle C_{ij} \rangle < 0$), white ($\langle C_{ij} \rangle = 0$), and blue ($\langle C_{ij} \rangle > 0$) regions. When the up and down states are degenerate, as is the case for the C3 and C4 M_{NN} configurations, then $\langle C_{ij} \rangle = 0$ for both orientations. In contrast, if the up and down states are not degenerate, then the magnitude $|\langle C_{ij} \rangle|$ for both orientations will be identical, but the sign of $\langle C_{ij} \rangle$ will be positive or negative for the orientation which maximizes the amount of attracting or repelling interactions, respectively. For example, when M_{NN} is set to the C1 configuration, the down state produces $\langle C_{ij} \rangle = +1$ and has lower ΔE values compared to the up state which has $\langle C_{ij} \rangle = -1$. A similar behavior also occurs with the C2 M_{NN} configuration, except $|\langle C_{ij} \rangle| = 0.5$. This reduced magnitude is caused by the bottom set of nanoislands in the C2 M_{NN} configuration, which produces one attracting and one repelling interaction with an up or down

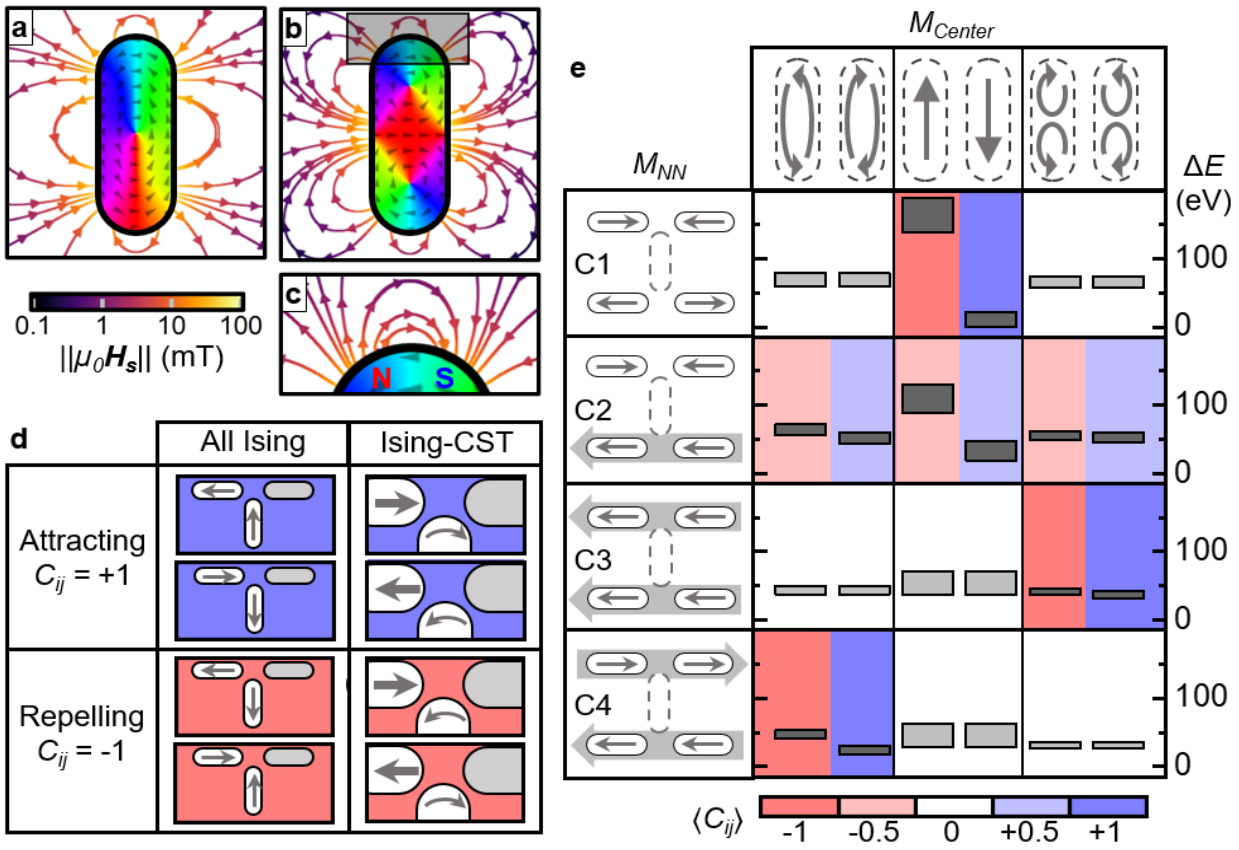

Figure 4.3: *Magnetization maps and stray field profiles of (a) single and (b) double vortex domains. The colored regions within the black outline represents the in-plane component of the magnetization (also indicated by the arrows). The magnitude of the stray field is indicated by the color bar. (c) Zoom-in of the nanoisland tip in (b), which exhibits a dipole-like stray field profile. Similar stray field profiles are also present in the tip of (a). (d) Schematics of attracting (blue) and repelling (red) magnetization configurations at the brickwork vertices for pairs of nearest neighboring Ising domains and Ising-CST nanoislands. (e) Magnetization-dependence of ΔE bands for brickwork units with W = 175 nm and a = 650 nm. The top and bottom of each ΔE band corresponds with calculations where* ***m*** *in Ising nanoislands either remain fully magnetized or are allowed to relax, respectively. Each cell in the table corresponds with a unique combination of* M_{NN} *and* M_{center} *and are color coded based on the associated* $\langle C_{ij} \rangle$ *value calculated from Equation 4.1 (see main text for details).*

M_{center}. Thus, C_{ij} between M_{center} and the bottom two nanoislands sum to zero while the top sets of nanoislands sum to ±2.

The ΔE bands in Figure 4.3(e) also show that for CSTs, the relative energies between two chiral states depend on which M_{NN} is present. I will demonstrate that this behavior can be understood by first simplifying the interpretation of Ising-CST interactions using an effective dipole model and subsequently calculating $\langle C_{ij} \rangle$ for the different chiral states. To understand how vortex-bearing nanoislands interact with adjacent Ising-bearing nanoislands, I studied the $\boldsymbol{H_s}$ profiles emitted by the vortex domains. Figure 4.3(a, b) show the $\boldsymbol{H_s}$ profiles for (Figure 4.3(a)) single and (Figure 4.3(b)) double vortex domains, which resemble those produced by quadrupoles and hexapoles, respectively. These profiles suggest that the transformations between spin texture topologies allow the nanoislands to switch between dipolar (Ising), quadrupolar (single vortex), and hexapolar (double vortex) behaviors. Consequently, these topology transformations alter the nature of interisland interactions in our ASIs not only from the reduced $\boldsymbol{H_s}$ magnitude associated with vortex domains, but also how their stray fields are directed in space.

Figure 4.3(c) shows a zoom-in of the $\boldsymbol{H_s}$ profile near the tip of a double-vortex-bearing nanoisland. This field pattern is also representative for nanoislands containing single vortex domains. The $\boldsymbol{H_s}$-profile near the CST nanoisland tips (i.e., where the strongest magnetostatic interaction takes place in the brickwork ASI) suggests that these tips behave as effective Ising-like dipoles which point towards the left or right. These two orientation states are controlled by the vortex chirality, where transforming between the chiral states will "flip" the Ising tip dipole. For the single and double vortex domains, the top and bottom tip dipoles are oriented antiparallel and parallel with each other, respectively. From these observations, I assumed that the Ising-CST magnetostatic interactions can be analyzed within an Ising framework by approximating the tips

of CST-bearing nanoislands as dipoles with magnetizations parallel or antiparallel with the adjacent Ising-bearing nanoislands as shown in Figure 4.3(d). Through this assumption, C_{ij} values for Ising-CST configurations were assigned in Figure 4.3(d) for the attracting and repelling tip configurations.

To test the validity of this approximation, I compared the ΔE bands and calculated $\langle C_{ij} \rangle$ for different M_{NN} and CST M_{center} in Figure 4.3(e). Within each cell of Figure 4.3(e), I find that $\langle C_{ij} \rangle$ predicts if the two chiral states of a CST M_{center} will be degenerate or be split into low and high energy states. That is, (1) $\langle C_{ij} \rangle = 0$ only when the chiral states are degenerate, (2) $\langle C_{ij} \rangle$ is nonzero if the chiral states are non-degenerate, and (3) $\langle C_{ij} \rangle > 0$ for the chirality which produces more attracting interactions (lower ΔE) while $\langle C_{ij} \rangle < 0$ for the other chiral state which produces more repelling interactions. This result demonstrates that the chirality-dependent energy shifting for CST M_{center} can be interpreted in the same manner that was discussed for the up and down M_{center} states. In other words, by treating the CST tip magnetizations as Ising-like dipoles, energy shifting between the chiral states can be predicted based on the relative amount of attracting and repelling tip interactions these two states produce for a given M_{NN}. From Figure 4.3(e), I find that the magnitude $|\langle C_{ij} \rangle|$ only depends on the combination of M_{NN} and CST type while the sign of $\langle C_{ij} \rangle$ depends on which chiral state is present. This behavior is identical to those observed in the correlation analysis for the Ising M_{center}. For both Ising and CST M_{center}, $|\langle C_{ij} \rangle| = 0.5$ (light red/blue regions in Figure 4.3(e)) when M_{NN} is set to the C2 configuration. Conversely, for each M_{center} domain type, only one M_{NN} exists which uniquely maximizes interisland attraction/repulsion (i.e., $\langle C_{ij} \rangle = \pm 1$, solid red/blue colored regions in Figure 4.3(e)) and two M_{NN} which causes the orientations/chiralities to become two-fold degenerate (i.e., $\langle C_{ij} \rangle = 0$, white regions in Figure 4.3(e)). I note that our definition of $\langle C_{ij} \rangle$ only informs us about degeneracies or energy splitting

that occurs between the two orientations/chiral states of a *given* M_{NN} and M_{center} domain type. That is, comparisons between $\langle C_{ij} \rangle$ calculated from Equation 4.1 can only be made between two states in a given cell of the table in Figure 4.3(e).

The energy and correlation analysis in Figure 4.3(e) suggests that for a given M_{NN} and M_{center} domain type, non-degenerate orientations and chiralities should appear with differing abundances, where the state with positive $\langle C_{ij} \rangle$ (lower ΔE) should appear with greater abundance than the negative $\langle C_{ij} \rangle$ (higher ΔE) state. For thermally demagnetized ASIs containing only Ising nanoislands, this behavior is generally expected for strongly interacting nanoislands and has been observed in LSMO brickwork ASIs [109]. However, it is not clear whether non-degenerate CST chiralities will appear with differing abundances in thermally-demagnetized ASIs. To this end, I analyzed XMCD PEEM images of the thermalized LSMO brickwork ASI used in Ref. [109] to determine the relative abundance of different M_{NN} and CST M_{center} combinations present in these images. The four XMCD PEEM images in this dataset contained 332 ± 24 I-shaped nanoisland sets (i.e., Figure 4.1(c)). Out of this set, I examined the single and double vortex domains with $|\langle C_{ij} \rangle| > 0$, which comprises 3.5% ± 1.1% and 9.9% ± 2.0% of the total set population, respectively. The errors correspond with the standard deviation between statistics gathered from four XMCD-PEEM images.

Figure 4.4 plots the relative abundance between the two chiral states for single and double vortex domains when $\langle C_{ij} \rangle = \pm 1$ (Figure 4.4(a)) and ± 0.5 (Figure 4.4(b)). The error bars represent the standard deviation between the relative abundances acquired from four unique XMCD PEEM images. As discussed before, for both single and double vortex domains, $\langle C_{ij} \rangle = \pm 0.5$ when M_{NN} is set to the C2 configuration. When $\langle C_{ij} \rangle = \pm 1$, the M_{NN} for single and double vortex domains is associated with the C4 and C3 configurations, respectively. For the double vortex domain with

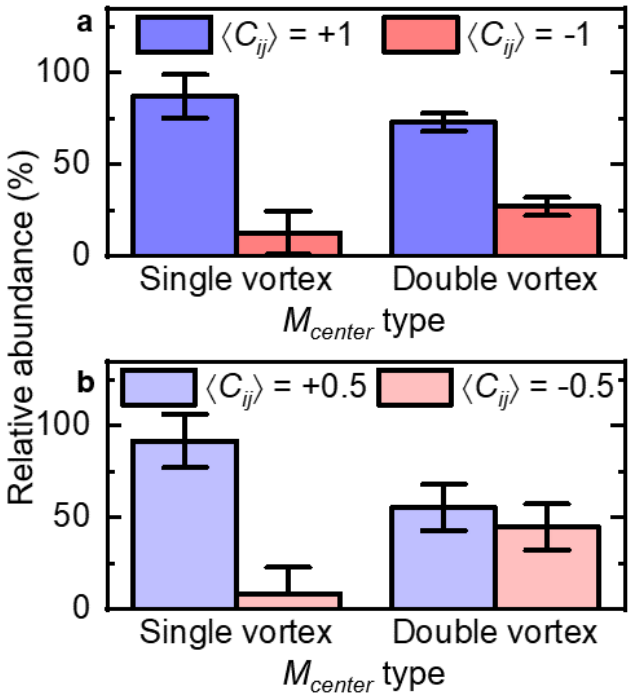

Figure 4.4: *(a,b) Relative abundance of non-degenerate CST chiral states appearing in XMCD PEEM images with (a) ⟨C_{ij}⟩ = ±1 or (b) ⟨C_{ij}⟩ = ±0.5 (see Figure 4.3(e)). The error bars represent the standard deviation between the relative frequencies gathered from four unique XMCD PEEM images.*

⟨C_{ij}⟩ = ± 0.5 in Figure 4.4(b), the relative abundance between the two chiralities is similar to within the first standard deviation (i.e., the error bars overlap). Outside of this exception, Figure 4.4(a, b) show that the positively-correlated domain orientations/chiralities appear with greater abundance in the system. This correlation between the chirality-dependent CST populations, the micromagnetic simulations, and the correlation analysis suggests that CST formation is sensitive to the dipolar interactions imposed by the specific magnetizations of the nearest neighboring nanoislands.

The results of this work carry several implications for the study of ASI systems with mixed domain states. The ability to stabilize multiple domain states, along with the non-trivial nature of

the Ising-CST dipolar interaction, may give rise to ASI kinetics more complex than those observed in pure-Ising systems [10,24,66,113–117]. In such systems, the observable evolution occurs through a series of Ising domain flips (i.e., the magnetization changes orientation by 180°) and the thermal dynamics can be simulated using an Ising model of the ASI and applying the kinetic Monte Carlo method [24,115,116,118]. ASIs capable of possessing *both* Ising and CST domains, however, can be expected to possess additional relaxation pathways associated with the ability to access several domain states along with each exhibit different types of magnetostatic nanoisland coupling. Such insights could be applied towards designing annealing-based nanomagnetic logic devices [10,66] capable of exploiting the six spin texture states and their unique magnetostatic coupling behaviors.

Additionally, the stray fields emitted by CST domains shown in Figure 4.3(a-c) may give rise to exotic ordering behavior in ASI structures such as the pinwheel [113,119,120], quadrupole [8], and trident [116] arrays. Unlike the brickwork ASI, where the nanoislands meet exclusively at the tips (i.e., experiences the shortest island-to-island distance), pairs of nanoislands in these systems are either positioned side-by-side or have the tip of one nanoisland point into the body of another. Such systems could take advantage of the magnetostatic coupling between nanoislands producing dipolar (Ising), quadrupolar (single vortex), and hexapolar (double vortex) stray field profiles.

4.4 – Conclusions

In conclusion, using micromagnetic simulations and XMCD PEEM imaging, I demonstrate how the energetics and formation of chiral CSTs depend on the magnetization of the nearest neighboring nanoislands. By analyzing the stray field emission profiles of single and double vortex domains, I found that the analysis of magnetostatic interactions with CST-bearing nanoislands can

be simplified by approximating the nanoisland tips to possess effective Ising-like dipoles. This approximation facilitated the interpretation of our energy calculations of interacting nanoisland sets, where M_{NN}-dependent energy splitting between CST chiralities was explained by changes in the amount of attracting and repelling tip interactions each chiral state produced. Finally, I show though a statistical XMCD PEEM study that Ising-CST configurations with higher correlation values appear in greater abundance in contrast with configurations that are not as highly correlated. Our findings show that Ising and CST domains can magnetostatically couple in non-trivial manners, which have potential consequences for the study of thermally-active ASI systems and design of annealing-based nanomagnetic logic devices which seek to exploit these states.

Chapter 5: Imaging Thermal Relaxation in $La_{0.7}Sr_{0.3}MnO_3$-Based Artificial Spin Ice Structures

5.1 – Introduction

Chapters 3 and 4 focused on the static behavior of ASIs which were thermally annealed to achieve a low energy configuration. Another area of active interest is the study of the relaxation dynamics of thermally-active ASIs to understand how thermodynamically stable magnetic phases can be accessed in these interacting systems [24,113,115]. Additionally, the thermal relaxation behavior of ASIs have potential applications in the development of annealing-based nanomagnetic logic devices [10,66]. In these studies, the system is held near its magnetic transition temperature (e.g., T_c) and the evolution in magnetic ordering can be monitored using, for example, XMCD-PEEM [24,113,115], transmission x-ray microscopy [121], and superconducting quantum interference device (SQUID) magnetometry [122]. Most studies of thermally-active ASIs have focused on systems where the nanoislands can only stabilize Ising states (henceforth referred to as "pure-Ising ASIs"). The evolution of such system occur through the 180° magnetization reversal of the Ising-like nanoisland, where the rate of these so-called "flips" are sensitive to the magnetostatic (dipolar) interactions imposed by both the magnetization of the neighboring nanoislands [24] as well as the ASI lattice geometry [113].

The ability for the LSMO-based ASIs to stabilize both Ising and CST states in Chapters 3 and 4 raises the question of what the relaxation pathways look like in these types of systems. While Chapters 3 and 4 provided insight into the energetics of these systems along with how likely one would observe certain domain states, they do not provide direct information about *how* the individual nanoisland domain states and different magnetic ordering states in the LSMO-based ASI are accessed. Understanding the relaxation pathways in LSMO-based ASIs is essential to

engineer spin texture states and magnetic ordering in both ASI systems as well as computing devices based on ASI or nanomagnet architectures which seek to exploit the multi-domain states of nanoislands for computing or memory-based applications.

In this chapter, I used XMCD PEEM to investigate the thermal relaxation behavior in ASIs capable of bearing Ising and CST states. Using the *in-situ* heating capabilities of the PEEM-3 microscope at the Advanced Light Source, I used a pulsed annealing protocol to capture several "snapshots" of a magnetized LSMO-based ASI undergoing thermal relaxation. By tracking the domain changes in each nanoisland as a function of the cumulative annealing time, the rates of different types of domain changes were calculated. The variation of these rates as a function of the cumulative annealing time indicates that the ASI prefers to stabilize either Ising or CST states during different stages of the annealing process. These results also suggest that vortex nucleation-annihilation may serve as the primary transformation mechanism influencing the intrinsic energy barrier of each nanoisland.

5.2 – Methods

A 3 nm LSFO / 40 nm LSMO bilayer was grown epitaxially on a (001)-oriented Nb-doped $SrTiO_3$ (0.5 wt. % Nb) substrate using pulsed laser deposition with a laser fluence of ~1 J cm^{-2} and frequency of 10 Hz and 1 Hz for the LSFO and LSMO layers, respectively. As will be discussed later, we assume that this sample can be approximated as a single layer of LSMO as the LSFO layer was found to be nonmagnetic. During the growth, the substrate temperature was held at 700 °C with an oxygen pressure of 0.3 Torr. The films were slowly cooled to room temperature post deposition in 300 Torr O_2 to ensure proper oxygen stoichiometry. Structural characterization was performed with x-ray reflectivity and x-ray diffraction to confirm coherent growth, crystalline quality, and thickness of the film. ASI arrays with a lattice spacing, a = 638 nm were defined in

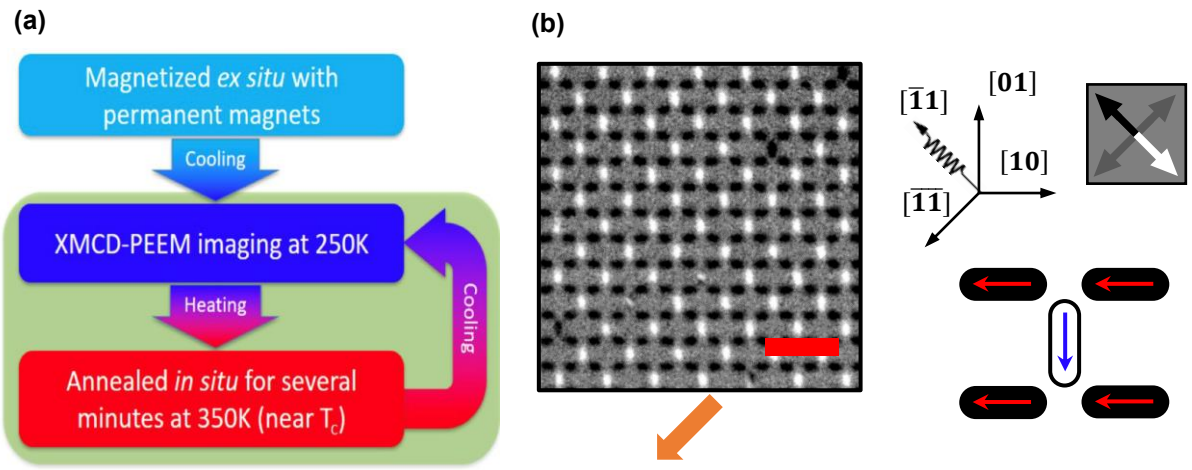

Figure 5.1: *(a) Schematic of the pulsed annealing/imaging protocol used to probe thermal dynamics in LSMO-based ASIs. (b) XMCD PEEM image and associated magnetization schematic of the magnetized brickwork ASI. The legends on the far right indicate the experimental geometry and magnetization orientation. The sample was magnetized along the [$\bar{1}\bar{1}$]-direction. Scale bar is 2 μm.*

different regions of the sample using a patterning technique based on the local modification of the structural and magnetic order by a flood Ar^+ ion implantation (For details, see Chapter 2). Atomic force microscopy measurements indicated that the lengths and widths of the patterned nanoislands were approximately 398 ± 10 nm and 173 ± 9 nm, respectively. These nanoislands were patterned such that the two-dimensional ⟨10⟩ axes of the ASI were aligned with the ⟨110⟩ in-plane easy axes of the LSMO film under tensile strain [92].

To study the thermal relaxation behavior of LSMO-based ASIs, a pulsed-annealing protocol was used with the steps schematically shown in Figure 5.1(a). This protocol was chosen over a fixed temperature measurement to (1) maximize the XMCD signal strength to enable the confident identification of CST domains while (2) enabling the observation of the ASI relaxation behavior within the limited amount of experimental time allotted for the PEEM3 microscope (on

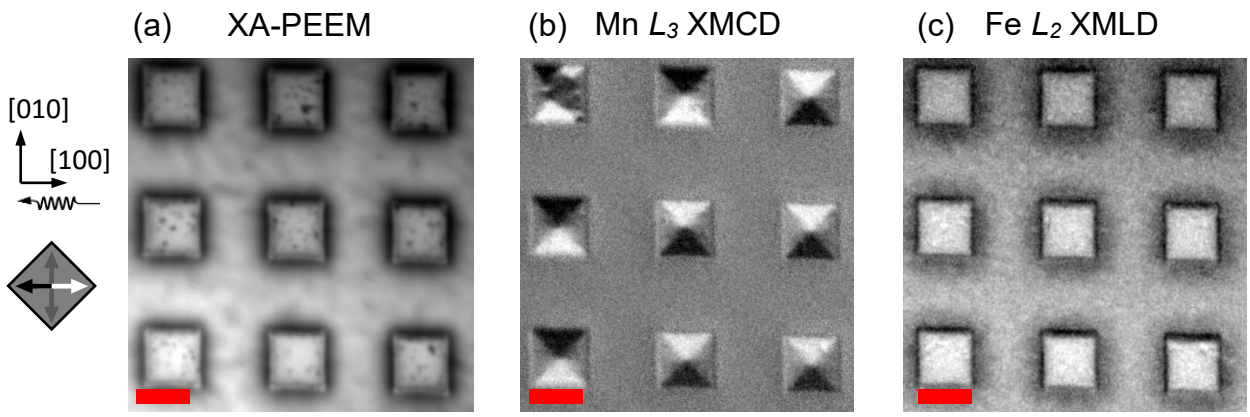

Figure 5.2: *(a) XA-PEEM image of square micromagnets patterned in the LSMO/LSFO bilayer sample. (b,c) Corresponding (b) Mn L_3 XMCD and (c) Fe L_2 XMLD PEEM image of the region imaged in (a). All measurements shown here were acquired at a temperature of 110 K. Scale bars are 2 μm. The legends shown on the far left indicate the sample geometry and magnetization orientations in the XMCD PEEM image.*

the order of a day). Prior to the experiment, the sample was magnetized along the $[\overline{11}]$ direction using a pair of permanent magnets attached to a steel core. The magnetized sample was first imaged at a temperature of 250 K (Figure 5.1(b)) to freeze the magnetic configuration in place during the acquisition of an XMCD PEEM image. Prior to imaging, the sample was held at 250 K for ~10 minutes. This temperature was chosen to achieve an optimal balance between the XMCD contrast signal strength (increases at lower temperatures) and reducing the time required to subsequently heat the sample to the annealing temperature T_{anneal} of 350 K (rate of 5 K/min). The time the sample temperature dwelled at T_{anneal}, t_{anneal}, was on the order of several minutes. After the annealing step was completed, the sample was cooled back down to 250 K at a rate of ~ 9 K/min for imaging. To study the thermal evolution, the annealing and imaging steps are performed several times.

5.3 – Single Layer LSMO Approximation

Prior to imaging the ASI arrays, the magnetism in the LSMO and LSFO layers of the bilayer were assessed by performing XMCD and XMLD PEEM imaging studies, respectively. Figure 5.2 shows 2 μm squares patterned into a different region of the same bilayer sample, where Figure 5.2(b) shows the Mn L_3 XMCD-PEEM image for the LSMO layer and Figure 5.2(c) shows the Fe L_2 XMLD-PEEM for the LSFO layer. The images were acquired at a sample temperature of 110 K, which is well below the nominal bulk LSMO T_c ~ 360 K and LSFO Néel temperature T_N ~ 400 K. As shown in Figure 5.2(b), the LSMO layer exhibits a pronounced XMCD signal as demonstrated by the clear black, white, and grey contrast, mostly corresponding to Landau domains. Conversely, in Figure 5.2(c), no noticeable XMLD signal was detected in the LSFO layer (i.e., no appreciable contrast variations were observed within each micromagnet). This behavior suggests that, at even 110 K, the LSFO layer does not exhibit antiferromagnetic ordering.

In previous studies of LSMO/LSFO superlattice systems, it was observed that the LSFO layers should exhibit antiferromagnetic ordering which is perpendicularly oriented with the LSMO magnetization through an interfacial exchange interaction known as spin-flop coupling [123]. However, the absence of an obvious antiferromagnetic signal in Figure 5.2(c) suggests that the magnetic properties of the LSFO layer were altered during the patterning process. One plausible explanation for this behavior is that, during the Ar^+ implantation process, the sample temperature may have become elevated which would increase oxygen mobility within the perovskite sample. This effect, in turn, would increase the likelihood of chromium oxide formation at the interface between the Cr hard mask and the LSFO surface, resulting in the 3 nm thick LSFO layer to become oxygen deficient. This oxygen deficiency would, in turn, alter the magnetic properties of the layer. While the exact cause of this behavior remains unknown, I assumed in the subsequent discussion

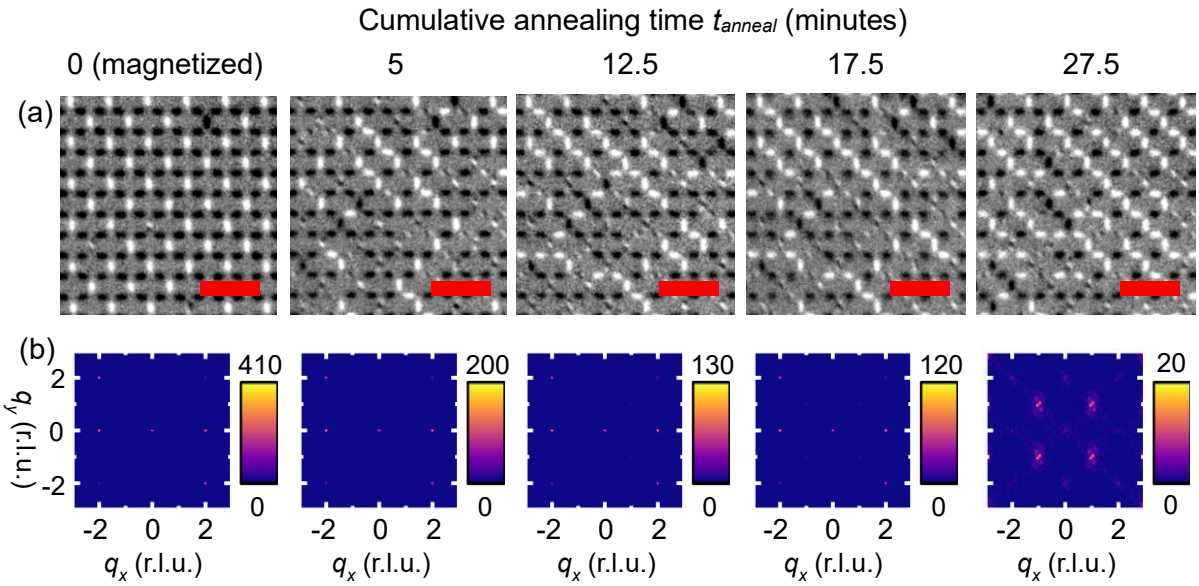

Figure 5.3: *(a) Representative XMCD PEEM images and (b) MSF calculations of thermal relaxation in brickwork ASIs. Each MSF map represent the average of MSFs calculated for XMCD PEEM images of three duplicate ASIs. Scale bars are 2 μm. reciprocal lattice units (r.l.u.)*

that the LSFO layer does not magnetically influence the system and can be ignored. Despite this behavior, the LSFO effectively serves as a capping layer which prevents the degradation of the studied LSMO layer.

5.4 – Results and Discussion

Figure 5.3(a) shows XMCD-PEEM images acquired for the brickwork ASIs over the course over several annealing steps. The total time the sample dwells at the annealing temperature is represented by the cumulative annealing time, t_{anneal}. As shown in Figure 5.3(a), the first annealing step resulted in the production of CSTs (nanoislands which contain black and white speckles) as well as low-energy Ising configurations which appear as black/white staircase-like patterns. As the system undergoes subsequent annealing cycles, the lengths of the black/white staircase patterns grows, indicating the gradual establishment of the ground state Type I configuration. This behavior can also be observed in the corresponding magnetic structure factors

(MSF) in Figure 5.3(b), which represents the mean MSF calculated from XMCD PEEM images of three duplicate ASIs. As the ASI undergoes thermal annealing, the most intense magnetic Bragg peaks of the magnetized state at (2 0), ($\bar{2}$ 0), ($\bar{2}$ 2), and (2 $\bar{2}$) decreases in intensity. The establishment of the ASI ground state configuration appears in the MSF as peaks located at {11}, which exhibit the strongest intensities at the final annealing step at t_{anneal} = 27.5 minutes.

Understanding the thermal evolution in LSMO-based ASIs requires studying the collective ordering of the system (i.e., Figure 5.3) as well as the individual nanoisland behavior. The transformation rate, ν, of the individual nanoislands can be modeled using an Arrhenius expression

$$\nu = \nu_0 \exp\left(-\frac{E_a}{k_B T}\right) \quad \text{Eq. 5.1}$$

where k_B is the Boltzmann constant, E_a is the activation energy barrier, and v_0 is the Arrhenius prefactor (also referred to as the attempt frequency). v_0 is often assumed to be constant on the order of 10^{10}-10^{12} sec^{-1} [15,24,115,124] depending on the nanoisland morphology and domain transformation mechanism involved [125].

Assuming that v_0 is constant, then ν at a fixed T_{anneal} depends on E_a, which itself reflects the intrinsic energy barrier to change the nanoisland domain state E_c and an extrinsic energy barrier associated with changes in dipolar interactions E_i

$$E_a = E_c + E_i \quad \text{Eq. 5.2}$$

For pure-Ising ASIs, E_i can be calculated as the difference between the dipolar interaction energies (Eq. 1.1) of a nanoisland set before and after an Ising flip. The evaluation of E_c is generally less straightforward as it depends on the specific domain transformation mechanism involved. Ising flips have been modeled as a coherent rotation of the magnetization or a nucleation and propagation of a domain wall [125]. The mechanism involved depends on the size of the

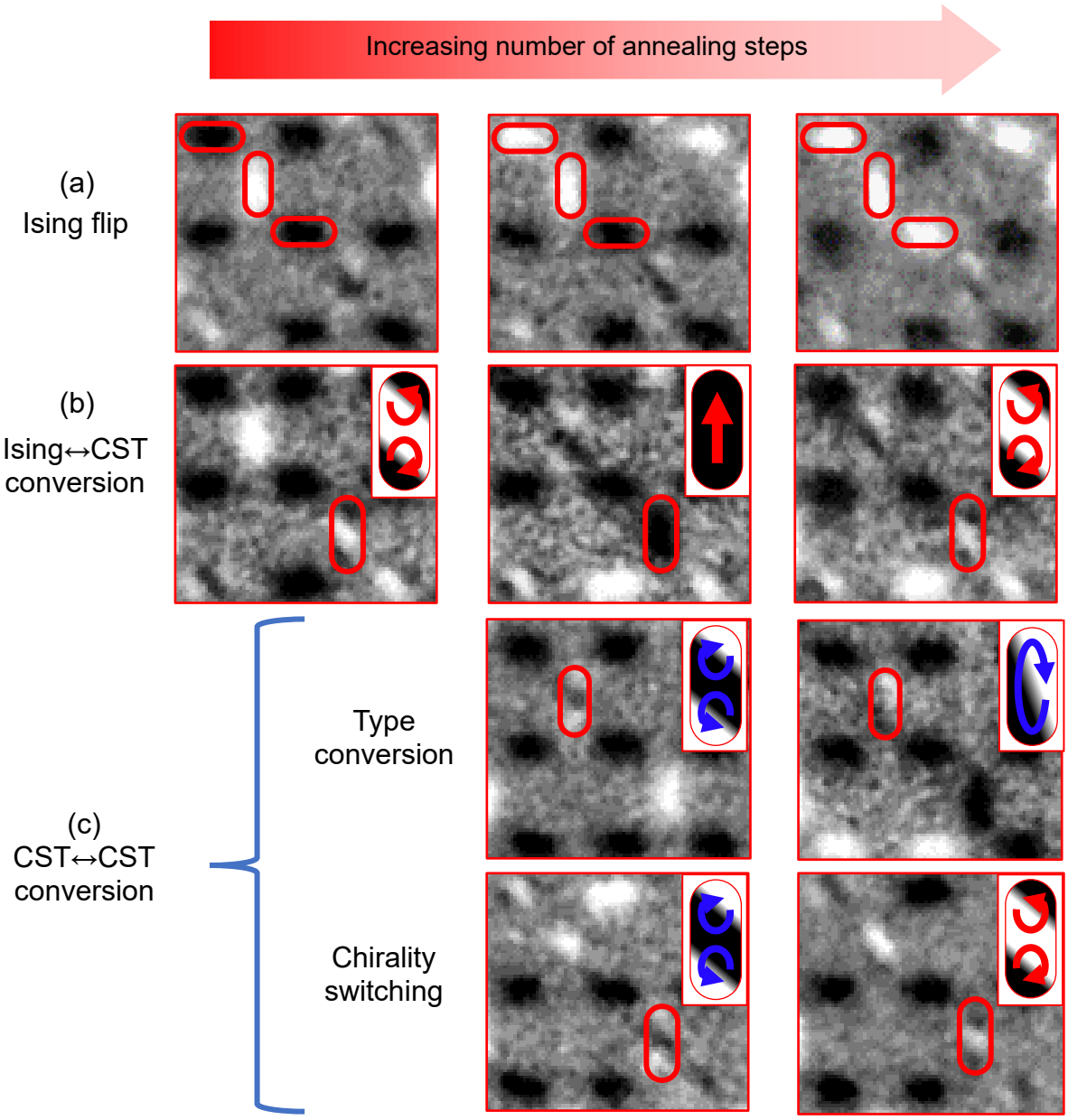

Figure 5.4: *(a-d) XMCD PEEM images of fixed regions after multiple annealing steps, where adjacent images (left-to-right) differ by one annealing step. Local state changes observed after annealing cycles involved (a) Ising flips, (b) Ising-CST conversions, (c) CST type conversion (i.e., single to double vortex conversion or vice versa), and (d) CST chirality switching.*

nanoisland, where nanoislands too small to accommodate a domain wall will favor coherent rotation over domain wall formation.

Developing a model capable of reproducing the dynamics of CST-bearing ASIs requires knowledge of the different domain transformations which occur as the ASI thermally relaxes. To characterize the different domain changes which occur in this system, I compared the domain states of each nanoisland across several annealing steps. Figure 5.4 shows the different types of domain transformations observed after a series of annealing steps is performed. Note that, since the dynamics of the ASIs are not being imaged in real-time, Figure 5.4 shows the *apparent* transformation observed in the system; this point will be discussed later in this chapter.

The first transformation type is called an Ising flip (Figure 5.4(a)), where an Ising state nanoisland experiences a 180° rotation of its magnetization (i.e., the black domain turns white, and vice versa). The second transformation type is an Ising↔CST conversion (Figure 5.4(b)), where an Ising state transforms into a CST (Ising→CST) and vice versa (CST→Ising). Figure 5.4(b) shows the Ising→CST conversion observed for the nanoisland highlighted in red, where the initially double vortex CST state (left image, black-white-black pattern) transforms into an Ising state (center image, uniformly black) after one annealing step. The CST→Ising conversion can be observed for this nanoisland by annealing the system once more, converting the Ising state (center image) into a double vortex CST (right image). The third type of transformation shown in Figure 5.4(c) is a conversion between the different CST states referred to as CST↔CST conversion. This transformation type includes both changes in the CST type (i.e., single to double vortex state) and chirality (i.e., inversion of grayscale contrast).

To quantitively compare the rates at which different domain transformation types "□" (box symbol) are observed (i.e., Figure 5.4), I calculated the apparent domain transformation rate, $\nu_{\square}$ as

$$\nu_{\square} = \frac{N_{\square}}{N_{ASI} \cdot \Delta t_{anneal}} \qquad \text{Eq. 5.3}$$

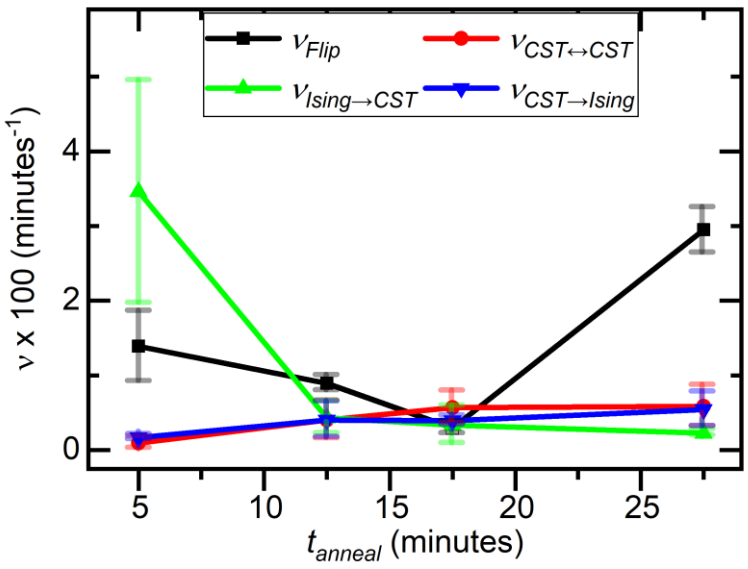

Figure 5.5: *t_{anneal}-dependence of ν_{Flip}, $\nu_{CST\leftrightarrow CST}$, $\nu_{Ising\rightarrow CST}$, $\nu_{CST\rightarrow Ising}$. Error bars represent the standard deviation across XMCD PEEM images of 3 duplicate ASIs.*

where N_{ASI} is the total number of nanoislands studied in the ASI (746 ± 31 across three duplicate patterns), Δt_{anneal} is the duration that T_{anneal} was maintained for an annealing step, and "□" corresponds with either an Ising flip (□ = "Flip"), CST↔CST conversions (□ = "CST↔CST"), Ising→CST conversions (□ = "Ising→CST"), or CST→Ising conversion (□ = "CST→Ising"). Since the XMCD PEEM images acquired before and after the anneal may not capture all transformation events which occurred during the anneal, $\nu_{□}$ represents the lower bound to the actual t_{anneal}-dependent transformation rates of the system. For brevity, these apparent rates and apparent transformations will be henceforth referred to as rates and transformations, respectively.

Figure 5.5 shows the different apparent transformation rates plotted as a function of t_{anneal}. The error bars in Figure 5.5 corresponds with the standard deviation between XMCD PEEM images acquired for three duplicate ASIs. The initial evolution of the ASI at t_{anneal} = 5 minutes largely involved the Ising→CST conversion, with $\nu_{Ising\rightarrow CST}$ being about twice as large as ν_{Flip}. The CST↔CST and CST→Ising conversions occur with the smallest frequencies at this annealing step,

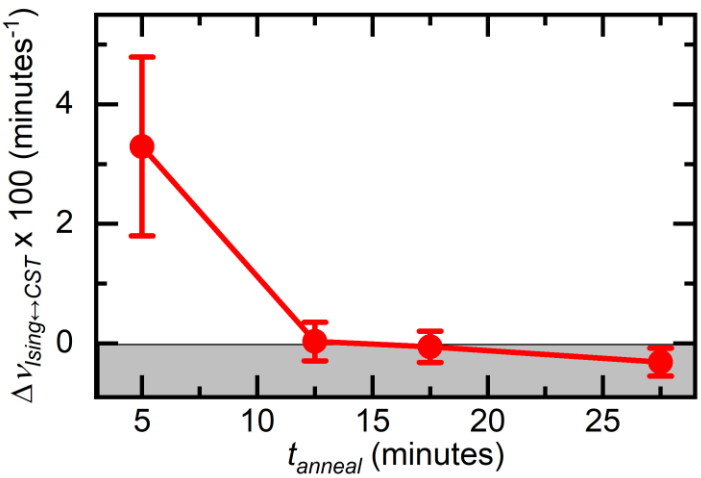

Figure 5.6: *$\Delta\nu_{Ising\rightarrow CST}$ as a function of t_{anneal}. Error bar represent the standard deviation across XMCD PEEM images collected for three duplicate ASIs. The gray region highlights when the rate difference is less than zero.*

which can either be attributed to the initial magnetized state containing < 5% CSTs or the Ising→CST conversion being kinetically preferable over the CST→Ising conversion. As the anneal progressed, several trends were observed for the different transformation types. For Ising→CST conversions, $\nu_{Ising\rightarrow CST}$ experienced an initial sharp decrease for t_{anneal} = 12.5 minutes, followed by a slower decrease in value as t_{anneal} approached 27.5 minutes. The opposite CST→Ising conversion, $\nu_{Ising\rightarrow CST}$ increased as t_{anneal} increased, but remained relatively constant from t_{anneal} = 12.5 to 17.5 minutes. Conversions between CST states $\nu_{CST\leftrightarrow CST}$ also increased with t_{anneal} until 17.5 minutes, where $\nu_{CST\leftrightarrow CST}$ remained relatively constant until t_{anneal} = 27.5 minutes. Finally, ν_{Flip} decreased with t_{anneal} until 17.5 minutes, after which ν_{Flip} increased by approximately an order of magnitude from 17.5 minutes to 27.5 minutes.

For ASIs capable of bearing both Ising and CST states, it is of interest to compare the different rates at which Ising states will convert into CSTs and vice versa. This comparison was performed by calculating $\Delta\nu_{Ising\leftrightarrow CST}$ defined as

$$\Delta\nu_{Ising\leftrightarrow CST} = \nu_{Ising\rightarrow CST} - \nu_{CST\rightarrow Ising} \qquad \text{Eq. 5.3}$$

Figure 5.6 plots $\Delta v_{Ising \leftrightarrow CST}$ as a function of t_{anneal}. Figure 5.6 can be understood as follows: If $\Delta v_{Ising \leftrightarrow CST} > 0$ (i.e., white region in Figure 5.6), then the rate of Ising→CST conversion is faster than CST→Ising conversions. Conversely, if $\Delta v_{Ising \leftrightarrow CST} < 0$ (i.e., gray region in Figure 5.6), then the opposite is true. If $\Delta v_{Ising \leftrightarrow CST} = 0$, then $\nu_{Ising \rightarrow CST} = \nu_{CST \rightarrow Ising}$. For this case, both rates can either be non-zero or zero, which indicate that transformations between Ising and CST states are either observed or not, respectively. While Eq. 5.3 cannot distinguish between these two situations, this equation can serve to highlight changes in the overall rate of new Ising and CST states produced in the system. As shown in Figure 5.6, $\Delta v_{Ising \leftrightarrow CST}$ achieves its maximum value at t_{anneal} = 5 minutes (i.e., rate of Ising→CST conversion is maximized), but progressively decreases below zero as t_{anneal} approaches 27.5 minutes.

These behaviors in Figures 5.5 and 5.6 suggest that the ASI undergoes several regimes of relaxation. The initial stage of relaxation (t_{anneal} = 5 minutes) is largely dominated by the conversion of Ising states into CSTs as well as Ising states flipping events. The intermediate stage of relaxation (t_{anneal} from 12.5 to 17.5 minutes) involves comparatively similar rates of the different domain transformation types. The final stage of observed relaxation is dominated by Ising flipping events while CSTs are being converted back into Ising states.

Before discussing the details of the experimental results, it is important to note several limitations of this approach in understanding the relaxation kinetics of the system. First, the annealing protocol used (Figure 5.1) only images the system before and after an annealing step is performed and, thus, will not capture all events which may have occurred in the system. As discussed earlier, the transformations observed in Figure 5.4 do not necessarily represent instantaneous changes which may occur in the system. That is, for each of the reported transformation mechanisms, several other domain transformations could have occurred within the

duration of that annealing step. Thus, a more accurate mapping of the kinetics would require a finer annealing time step Δt_{anneal}. Practically, the smallest usable Δt_{anneal} would be based on how quickly the sample temperature can be moved away from T_{anneal} (within a specified margin of error) using only the cryogen and heater controls of the PEEM3 microscope. The "sample temperature" reported by the PEEM3 microscope measures the temperature of the sample holder body and not the sample itself. While this work assumes that the actual sample and holder temperatures are equivalent, experimental and theoretical thermal characterization of the sample holder and LSMO sample should be performed to assess potential temperature variations. Second, the kinetics of the system will likely vary during the heating and cooling processes which may cause the measurements to be sensitive to the length of Δt_{anneal} with respect to the heating and cooling times. From Figure 5.5, an obvious correlation between Δt_{anneal} and $\nu_{\square}$ was not observed (i.e., the different rates do not appear to grow or shrink with Δt_{anneal}). This observation does not necessarily indicate that the kinetics are not influenced by the chosen annealing protocol as $\nu_{\square}$ will also be influenced by the magnetic configuration of the ASI itself. It should be noted that, while this latter effect can be expected to strongly influence the thermal evolution of the ASI, it is not a limitation associated with the experimental protocol itself and is an intrinsic behavior of the ASI. In this preliminary study, Δt_{anneal} was adjusted throughout the experiment in an attempt to capture the salient features of the thermal relaxation process. Subsequent studies should examine the dependence of $\nu_{\square}$ on a fixed Δt_{anneal} step size. Third, exact knowledge of the specific transformation mechanism requires a real-time domain imaging technique with high temporal resolution, high spatial resolution, and strong magnetic contrast. In many cases, all three criteria cannot be fulfilled simultaneously, and thus the domain transformation mechanism must be inferred based on whichever model best describes the evolution observed in the system.

Despite these limitations, the approach used in this study does allow for several insights to be drawn about the kinetics of ASIs capable of bearing CSTs. First, Figure 5.4 suggests that all domain transformations are facilitated by the nucleation and annihilation of vortex cores (henceforth referred to as vortex nucleation-annihilation). For nucleation, a vortex core is created at the nanoisland edge while, in annihilation, a vortex core is pulled out of the nanoisland body. Such a mechanism can broadly explain the how transformations involving CSTs occur. In regard to the Ising flip mechanism, the ability for a nanoisland to stabilize CSTs suggests that the nanoislands are too large to make coherent magnetization rotation a likely transformation mechanism. Thus, Ising flips in this situation may occur through what is effectively a domain wall nucleation and propagation event, where the domain wall is in the form of a vortex. It should be noted that vortex nucleation-annihilation can occur through several different modes. For an uniformly magnetized states (e.g., Ising), the nucleation of vortices may occur through several modes which, for instance, involves the magnetization vector field curling at the ends to resemble the letter "C" [126] and "S" [127].

The annihilation mechanism for a single vortex is typically described for systems under an applied magnetic field, where increasing the field strength increases the volume of moments aligned with the field at the expense of moments aligned antiparallel with the field. In other words, one half of the vortex grows while the other shrinks until the core sitting between the two halves is pushed "out of" the nanoisland wall. The vortex core, which can be considered as a topological defect, is not "deleted" from the system (i.e., violating winding number conservation) but rather breaks into topological edge defects pairs which can travel to opposite ends of the nanomagnet [128]. Micromagnetic studies of nano-sized disks have also predicted that vortex core annihilation events can be facilitated by thermally-induced fluctuations in the

magnetization [129,130]. Despite the expectation that thermal fluctuations should induce random displacements of the vortex core, it was found that finite temperatures can lead to a spontaneous net gyroscopic motion of vortex core about the disk center. This behavior thus causes the vortex core becomes displaced from the center (on the order of a few nanometers in permalloy), where the displacement increases with temperature [129].

Second, the results of Figure 5.5 suggest that the domain transformation kinetics of each nanoisland is sensitive to the magnetostatic interaction produced by the neighboring nanoislands. If the transformation rates were independent of dipolar interactions, then $\nu_{\square}$ would be constant as t_{anneal} is varied. However, Figure 5.5 shows obvious variations in $\nu_{\square}$ as t_{anneal} is varied. Increasing t_{anneal} also changes the magnetic ordering of the system as shown in Figure 5.3. With respect to Eq. 5.2, these results suggest that E_a depends on the magnetostatic interactions in the system. For pure-Ising ASIs, this behavior can be understood through the dependence of E_a on the dipolar interaction E_i, which can be calculated between the initial and final state using Eq. 1.1. For ASIs bearing CSTs, the magnetostatic interactions may influence both E_i as well as E_c, the latter of which is sensitive to the specific domain transformation mechanism involved. The relevant mechanism, as discussed before, are the nucleation and annihilation of vortices which have been demonstrated to depend on dipolar interactions in field-dependent studies [131]. Moreover, the magnetizations of each nanoisland can be slightly altered depending on the magnetization of the neighboring nanoisland. For instance, while an isolated nanoisland with an Ising state will have uniform magnetization, a pair of interacting nanoislands with Ising states may experience a curling of the tip magnetization to minimize the extent of "heads-to-heads" dipolar orientation [14]. Therefore, similar to the results of Chapter 4, the mode of vortex nucleation-annihilation may also depend on the domain state of the neighboring nanoislands as well as the nanoisland of interest.

Finally, the XMCD PEEM results in Figures 5.3 and 5.4 show that CSTs can be (meta)stabilized in the horizontal nanoislands of the brickwork ASI. While this behavior appears to conflict with the results of Chapter 3 and 4, the images in this work show ASI systems which are undergoing thermal relaxation from an excited (i.e., magnetized) state to the ground state configuration. In contrast, the ASIs studied in Chapters 3 and 4 were near the ground state configuration. The observation of CSTs in horizontal nanoislands during thermal relaxation may reflect several behaviors. Assuming that all domain transformations occur through vortex nucleation-annihilation, then the horizontal nanoisland can be expected to possess CSTs at various points in time while the ASI is thermally active. Even if the horizontal nanoislands favor the stabilization of Ising states, reversing the Ising magnetization would require the presence of a vortex to facilitate that process. However, this behavior alone would not explain why CSTs were more readily observed in the horizontal nanoislands of the nearly-magnetized ASI (Figure 5.3) but not in the thermalized ASI (Chapter 3 and 4). From Chapter 4 and the above discussion about the vortex nucleation-annihilation modes, it may be inferred that the (meta)stability of CSTs in the horizontal nanoislands is dependent on the magnetization of the nearest neighboring nanoisland. The results of Figures 5.3 and Chapter 3 suggest that CST (meta)stabilization in the horizontal nanoislands is more favorable when the ASI is largely magnetized along the ASI ⟨11⟩ directions (i.e., low values of t_{anneal}). However, as the ASI relaxes towards a demagnetized state, these states are no longer stable in the horizontal nanoislands.

5.5 – Conclusions

In conclusion, using XMCD PEEM imaging, I investigated the thermal relaxation behavior of ASIs capable of bearing Ising and CST states. I demonstrated that a pulsed annealing protocol can be used to probe the thermal relaxation of magnetized LSMO-based ASIs capable of bearing

Ising and CST states. As the ASI thermally relaxed towards the ground state Ising configuration, the individual nanoisland domain states underwent several different types of domain transformations. The rates at which each domain transformation types occurred exhibit different dependence on t_{anneal}. The observations suggest that thermal relaxation in LSMO-based ASIs is driven by vortex nucleation-annihilation events. This behavior further implies that the energy barriers associated with the domain transformation mechanism also depends on the magnetostatic interactions in the ASI. These results, combined with Chapters 3 and 4, illustrate that LSMO-based ASIs exhibit a complex energy landscape with relaxation pathways that are highly sensitive to magnetostatic interactions. Understanding the complex kinetics of this system can pave the way towards exploiting Ising and CST states in annealing-based nanomagnetic logic devices with ASI-inspired architectures.

Chapter 6: Conclusions

The work performed in this dissertation has further developed our understanding of spin texture formation in patterned magnetic nanostructures which experience dipolar interactions, with a specific focus on LSMO-based ASI systems. Nanostructured complex oxides have been proposed as promising foundations for next-generation computing devices capable of exploiting both charge and spin degrees of freedom (i.e., spintronics). Such devices would require the patterning of magnetic materials into nanostructures, whose shapes can influence the types of spin textures formed and, thus, influence the device functionality. Moreover, these nanostructures may couple with each other through magnetostatic interactions, which would also influence spin texture formation. Studies, such as those discussed in this dissertation, can clarify the sensitive relationship between spin texture formation, nanostructure properties, and magnetostatic interactions to create devices which can either suppress or exploit arbitrary spin texture states for computing applications.

Synchrotron soft x-ray photoemission electron microscopy has served as an indispensable tool for directly visualizing the magnetic domain at the nanoscale. The work of Chapter 3 applied XMCD PEEM imaging to study the magnetic ordering in LSMO-based ASIs, where an unusual nanomagnet-size and -spacing dependent formation of Ising and CST states were observed. In this study, micromagnet simulations have also been invaluable in clarifying the energetic reasoning associated with how the geometry-dependence of the magnetostatic interaction can influence domain formations in ASI systems. The formation of Ising and CSTs arise from the unique combination of magnetic properties in LSMO, which enables an energetic competition to occur between *intra*island effects (i.e., physics intrinsic to each nanoisland) and *inter*island effects (i.e., magnetostatic interactions).

While Chapter 3 demonstrated that spin texture formation depends on magnetostatic interactions from a geometry standpoint, Chapter 4 expanded upon this discussion by illustrating how the magnetizations of adjacent nanoislands influence the energetics of different spin texture states. Micromagnetic simulations demonstrated that the energetics of chiral CSTs depend on the magnetization of the nearest neighboring nanoislands. This behavior was clarified through an analysis of the stray fields produced by CSTs, which suggested that the tips of CSTs behave as effective Ising spins which experience dipolar coupling with the neighboring Ising nanoislands. This method of approximating the Ising-CST nanoisland interaction facilitated the interpretation of energetic differences between different CST chiralities with identical nearest neighboring nanoisland magnetizations. Though a statistical XMCD PEEM study, it was found that CST chiralities capable of minimizing the tip dipolar interactions appeared in greater abundance compared to the opposite chirality which maximizes the tip interactions. These findings show that Ising and CST domains can magnetostatically couple in non-trivial manners, which have potential consequences for the study of thermally-active ASI systems and design of annealing-based nanomagnetic logic devices which seek to exploit these states.

Finally, Chapter 5 investigated the relaxation kinetics of LSMO-based ASI systems capable of bearing multiple spin texture states. The feasibility of a pulsed annealing protocol was demonstrated in XMCD PEEM studies, allowing for the acquisition of multiple snapshots of the ASI relaxation process with acceptable XMCD signal strength to resolve CSTs. This experimental protocol enabled the observation of several different types of domain transformations, which suggest that thermal relaxation in LSMO-based ASIs is driven by vortex nucleation-annihilation events. The rates at which each domain transformation type occurred evolved over the course of the annealing experiment, suggesting that the energy barriers associated with the domain

transformation mechanism also depend on the magnetostatic interactions in the ASI. These results, combined with Chapters 3 and 4, illustrate that LSMO-based ASIs exhibit a complex energy landscape with relaxation pathways that are highly sensitive to magnetostatic interactions. In other words, the behavior of the individual LSMO-based nanoislands is highly sensitive to its intrinsic geometric and material properties as well as the magnetostatic interactions between the nanoislands. The results of this work suggests the potential to use magnetostatic interactions and nanoisland properties (geometric and material) to tailor the formation of arbitrary spin textures and exploit these different states in nanomagnet-based computing devices.

6.1 – Future Work

6.1.1 – Kinetics of Ising-CST Transformations

A comprehensive understanding of the kinetics in multidomain-bearing ASIs requires an understanding of the relaxation pathways along with the intermediate states which influences the evolution rate. Chapters 3-4 provide information about the (meta)stable magnetic states in the ASI systems while Chapter 5 sheds some light on the relaxation pathways such ASI systems may take. To gain a fundamental understanding about the kinetics of these systems, several additional studies should be performed.

First, imaging studies of the thermal relaxation process should be performed with a fixed annealing time step on the order of several seconds to minutes. Improving the time resolution of this type of experiment can provide greater clarity about the time-dependent trends associated with each different domain transformation rate. Moreover, a higher time resolution may allow for the study of transformation events involving a single nanoisland experiencing a domain change while the nearest neighboring nanoislands remain unchanged. The ability to observe these types of events could provide insights into how the domain transformation kinetics is influenced by the

magnetizations of the nearest neighboring nanoislands (e.g., Chapter 4). Such insights can provide greater clarity regarding the transient states (i.e., mode of vortex nucleation/annihilation) which can occur in these systems. From an experimental standpoint, such studies conducted with PEEM3 would require a further optimization of the thermal annealing protocol to minimize the total time required for heating and cooling the samples. Such efforts require minimizing the temperature difference between the annealing (350 K) and imaging (250 K) temperatures, which can be facilitated by either using a higher imaging temperature, lowering the annealing temperature, or altering the stoichiometry of the LSMO film to lower the T_c. Using the latter strategy, however, would require re-evaluating the ASI energy landscape as the magnetic properties (M_{sat}, A_{ex}, K_1) will be altered.

Second, the temperature-dependence of the magnetic energies would need to be evaluated. The energies calculated in Chapters 3 and 4 used the magnetic properties of LSMO at 110 K. However, these properties will vary with temperature, especially near the T_c of the sample. Thus, kinetic models of LSMO-based systems should account for the temperature dependence of the system energetics. Moreover, calculating the temperature-dependence of the different magnetic state energies can allow for the development of Monte Carlo simulations to further explore the equilibrium behavior as a function of temperature. For the development of Monte Carlo simulations, the energies of each state must be calculated beforehand. For ASIs containing CSTs, one approach to perform such simulations is to define each state based on the I-shaped structure at the heart of the brickwork ASI. The results of Chapter 5 suggests that each nanoisland (both vertical and horizontal orientations) in the brickwork structure can stabilize either Ising or CST states as the system relaxes from a magnetized state to the ground state configuration. Consequently, accurate simulations of the kinetics will require the consideration that each

nanoisland can possess six states (three domain types each with two orientations/chiralities). For the I-shaped structure, there will be a total of $6^5 = 7776$ individual magnetic states. However, the total number of unique states to consider will be less than 6^5 due to symmetries between the different magnetic states.

6.1.2 – Investigating CST Formation in Different ASI Geometries

This dissertation work provides insights into how the magnetostatic interactions between nanoislands can influence spin texture formation in brickwork ASI lattice. However, this work alone does not provide a general understanding of interaction-dependent spin texture formation since the magnetostatic interactions are sensitive to both the separation and orientation between adjacent nanomagnets. Thus, future efforts in investigating these effects should focus on studying nanoisland arrangements beyond the brickwork lattice geometry.

This research direction can be facilitated by the numerous lattice geometries which have been explored in the field of ASIs (Figure 1.3, [1]). Each ASI geometry subjects the nanoislands to different magnetostatic interaction environments. While some geometries force the nanoisland tips to point towards each other (e.g., square, brickwork, and Kagome ASIs), others have the nanoislands placed side-by-side (e.g., dipolar quadrupole and trident ASIs) or have tip of one nanoisland point into the body of another (e.g., pinwheel ASI). When fabricated from LSMO, such ASI geometries could serve as a platform for investigating how spin texture formation depends on the orientations of the individual nanoislands. Moreover, the stray field analysis discussed in Chapter 4 suggests that CSTs could facilitate tip-body magnetostatic coupling between the nanoislands in ASIs such as the pinwheel and trident systems. These interactions could give rise to ordering behaviors and phase transitions beyond those observed in pure Ising systems.

Appendix

A.1 – Instrumentation Development of an X-ray Detected Ferromagnetic Resonance Spectrometer

A.1.1 – Introduction

X-ray detected ferromagnetic resonance (XFMR) is a technique based on x-ray magnetic circular dichroism (XMCD) for studying the time-resolved precessional motion of spins undergoing ferromagnetic resonance (FMR) [132–135]. XFMR combines the sensitivity of FMR spectroscopy to the magnetization dynamics of a sample with the chemical sensitivity of x-ray absorption spectroscopy which serves as the underlying detection mechanism. Thus, XFMR is a powerful tool to investigate the magnetization dynamics of complex material systems and enables the element and valence specific detection of magnetization dynamics. Such detection capabilities are also instrumental for investigating the propagation of spin currents in complex heterostructure systems [132].

At the Advanced Light Source beamline (BL) 4.0.2 (henceforth referred to as BL 4.0.2), the XMCD signal measured during FMR (in the following referred to as XFMR signal) is detected through the total optical photoluminescence yield (LY) signal of the sample [132,133,136]. The strength of the LY signal, and thus the XFMR signal, depends on several factors intrinsic to both the sample properties and the instrumentation used. In terms of the samples, the detected LY signal can strongly depend on factors, such as sample temperature and choice of substrate [137]. Generally, the greater the LY efficiency (i.e., conversion of x-ray flux into visible photons) of a substrate, the easier it is to detect and measure a potential XFMR signal. Thus, substrates such as MgO and $MgAl_2O_4$ (MAO), which exhibit large room temperature LY efficiencies of

approximately 0.1 and 0.03, respectively, are preferred over substrates with small room temperature LY efficiencies, like LSAT (0.004) and STO (0.0009) [137].

Therefore, the selection of a suitable substrate should partially be guided by experimental requirements (i.e., a substrate with greater LY efficiency may be preferable for LY-based XAS studies), however, epitaxial single crystal thin films cannot be grown on arbitrarily chosen substrates: similar crystal structures must be maintained between the film and the substrate. Thus, thin film growth of complex oxides on highly luminescent substrates may not be feasible.

If the LY emission of the sample cannot be further optimized, then an alternative route to enhance the LY signal is to improve the LY detection hardware. In order to enable the investigation of LSMO-based epitaxial heterostructures with XFMR, which are nominally grown on LSAT or STO substrates, I investigated and implemented methods to enhance the detection sensitivity of the XFMR instrumentation at BL 4.0.2. Comparative XAS studies performed between the dedicated XFMR and LY holders revealed the former did not provide sufficient signal sensitivity to measure samples grown on LSAT substrates. By upgrading the photodiode (PD) used in the XFMR holder, I found an improvement in the LY detection capability, where the XFMR holder measures LY signal sensitivity comparable to those produced by the standard LY holder.

A.1.2 – Principles of XFMR

In XFMR, XAS-XMD spectroscopy is used to probe microwave (GHz-frequency) excited magnetization dynamics. XFMR is based on FMR spectroscopy, where magnetic moments are driven into precession about a static magnetizing field $\boldsymbol{H}_{static}$ through an oscillating RF magnetic field $\boldsymbol{H}_{RF}$. In these measurements, $\boldsymbol{H}_{static}$ is perpendicular to $\boldsymbol{H}_{RF}$ and an FMR spectrum is collected as a function of $\boldsymbol{H}_{static}$ magnitude and/or $\boldsymbol{H}_{RF}$ frequency [138,139]. While FMR detects magnetization dynamics through the absorption of microwave power, in XFMR the underlying

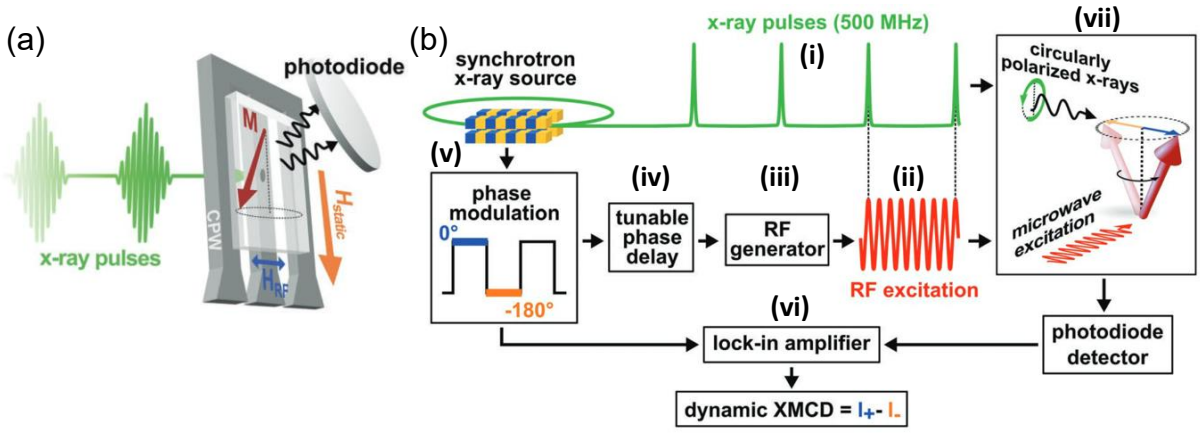

Figure A.1.1: *(a) Schematic of the LY signal measurement scheme for XFMR experiments at ALS BL 4.0.2. (b) Schematic of the time-resolved XFMR measurement technique* [132]. *The role of the instruments and processes labeled with (i-vii) are discussed in the text.*

detection mechanism is the XAS-XMCD signal. As discussed later, the XMCD signal can be mapped as a function of time, where changes in the XCMD signal intensity corresponds with the time-varying projection of the magnetic moment $\boldsymbol{m}$ onto the x-ray beam orientation $\boldsymbol{k}$ (i.e., $I_{XMCD} \propto \boldsymbol{m} \cdot \boldsymbol{k}$).

The precessional behavior of a ferromagnetic system can be described by the Landau-Lifshitz-Gilbert equation of motion

$$\frac{d\boldsymbol{m}}{dt} = -\frac{\gamma}{1+\alpha^2}\left(\boldsymbol{m} \times \boldsymbol{H_{eff}} + \alpha\left[\boldsymbol{m} \times \left(\boldsymbol{m} \times \boldsymbol{H_{eff}}\right)\right]\right) \qquad \text{Eq. A.1}$$

where $\boldsymbol{m}$ is the magnetic moment, α is a damping parameter, γ is the gyromagnetic ratio, and $\boldsymbol{H_{eff}}$ is the effective magnetic field influencing $\boldsymbol{m}$. $\boldsymbol{H_{eff}}$ includes both the externally applied field (i.e., $\boldsymbol{H}_{static}$) and different magnetic effects (e.g., exchange interaction, magnetocrystalline anisotropy, magnetostatics) which can be modeled as effective field terms [62]. Generally, resonant absorption of microwaves by thin film samples depends on several factors including the precessional motion

damping quantified by the Gilbert damping coefficient, α, any sources of magnetic anisotropy, as well as magnetic and structural inhomogeneities [138–140].

In XFMR spectroscopy, time-resolved XMCD is used to directly measure the motion of the precessing magnetic moments. Specifically, the magnetization precesses about $\boldsymbol{H}_{static}$ oriented perpendicular to the x-ray beam, and the time-dependent projection of the magnetization onto the x-ray beam is probed. Henceforth, any discussion of XFMR instrumentation is made in reference to the experimental setup at BL 4.0.2 [132,133]. In both broadband (i.e., variable radio frequency) FMR and XFMR, the sample is mounted film-side down on top of a coplanar wave guide (CPW) as shown in Figure A.1.1(a). GHz-frequency AC current is sent down the CPW, generating $\boldsymbol{H}_{RF}$ which oscillates perpendicular to the CPW length. In XFMR, the CPW possesses a ~100 μm diameter hole for the x-rays to pass through and irradiate the sample. The LY detection mode is used to collect the XAS-XMD signal. Time-resolved measurements in XFMR are performed by exploiting the time structure of the ALS synchrotron storage ring, referred to as the master oscillator. The ALS does not produce a continuous beam, but rather behaves as a strobe light producing ~70 ps long x-ray pulses every ~ 2 ns. This pulse time corresponds with a master oscillator frequency f_{ALS} of ~ 500 MHz (499.642 MHz ± 6 kHz [141]).

Figure A.1.1(b) schematically illustrates how the time-resolved XFMR measurement works. The roman numeral indices (i-v) discussed below are in reference to the same indices used in Figure A.1.1(b) to this discussion. XFMR works by phase locking $\boldsymbol{H}_{RF}$ (ii) with the synchrotron master oscillator (i). The frequency of $\boldsymbol{H}_{RF}$ is controlled by an RF comb generator (iii) which produces higher harmonics of f_{ALS} between 1 GHz to 4 GHz. Exceeding ~4 GHz results in a strong suppression of a measurable XFMR signal due to a blurring effect caused by the finite x-ray pulse length at the ALS [132]. Through phase locking the x-ray pulses (i) and RF excitation (ii), a

stroboscopic measurement of the magnetic precession can be performed. If a peak in $\boldsymbol{H_{RF}}$ is phase locked (i.e., "aligned" in time) with the x-ray pulses, then all subsequent x-ray pulses will arrive at the sample *only* when $\boldsymbol{H_{RF}}$ is at *a* peak position. By manually introducing a time offset (i.e., a phase delay (iv)) between the incoming x-ray pulses and $\boldsymbol{H_{RF}}$, different points in the magnetic precession can be accessed. Thus, the entire time-dependent RF response of a material can be mapped by measuring the XFMR signal as a function of the phase delay time.

As discussed earlier, in XFMR the GHz dynamics is driven by the CPW-generated $\boldsymbol{H_{RF}}$ while the precessional motion of the driven magnetic moments is measured via XMCD (or XMLD). As a function of time, $I_{XMCD/XMLD}$ changes as the moment precesses. Measurement of this signal is challenging since the cone that the precessing moment traces out has an angle on the order of $\Delta\theta \leq 1°$, where $\Delta\theta$ represents the maximum range of the moment angle variation. Thus, the XFMR signal is expected to be several orders of magnitude smaller than a static XAS-XMCD measurement, where $\Delta\theta = 180°$. For this reason, a lock-in amplifier (LIA, vi) setup is used to extract the small dynamic XMC/LD signal in an X-FMR measurement. A LIA is an instrument capable of detecting and measuring very small AC signals when provided a modulating reference signal for comparison. In an XMCD-XFMR experiment, the reference signal used is a 333 Hz-frequency 180° modulation (v) of the $\boldsymbol{H_{RF}}$ phase. This modulation allows for the measurement of an XMCD signal which represents the difference between XAS captured with (1) left and right hand polarized light for a fixed $\boldsymbol{H}$ (e.g., Figure 2.11(b)) or, equivalently, (2) $\boldsymbol{H}$ applied along two opposite directions for a fixed H magnitude and circular polarization. The phase modulation in XFMR utilizes method (2) to capture the dynamic XMCD signal, where $\boldsymbol{H}$ corresponds with $\boldsymbol{H_{RF}}$ which is being "flipped" along two opposite directions through the 180° phase modulation as shown in (vii) in Figure A.1.1.

For the case for a fixed circular polarization, the XFMR signal extracted by the LIA is the dynamic XMCD signal

$$I_{dyn}^{XMCD} = I_+ - I_- \qquad \text{Eq. A.1.2}$$

Where I_+ and I_- corresponds with the LY signal intensities at 0° and 180° modulation of $\boldsymbol{H_{RF}}$, respectively. With respect to Figure 2.11, I_+ and I_- would correspond with the XAS signal produced with RCP and LCP x-rays.

A.1.2 – XFMR Instrumentation at ALS Beamline 4.0.2

Prior to discussing the specific modifications made to the XFMR instrument, it is useful to provide context into the nature of the instrumentation used at BL 4.0.2. BLs are essentially vacuum pipes that the synchrotron-produced x-rays travel down towards the sample contained within experimental stations called "endstations". BL 4.0.2 contains several endstations, one of which is called the vector magnet (VMM, **v**ector **m**agneto**m**eter) endstation [142]. The VMM consists of an octupole electromagnet which surrounds a small vacuum chamber that the studied sample will reside within. This vacuum chamber is directly connected to the beamline and allows the sample to be exposed to the soft x-rays. The octupole magnet enables the sample to experience up to a 0.5 T magnetic field oriented in any arbitrary direction relative to the x-ray beam.

The samples themselves are attached to the sample holder which consists of a long (~1 m) shaft attached to a vacuum flange as schematically shown in Figure A.1.2(a). The length of the sample holder is required to position the sample within the center of the vacuum chamber surrounded by the octupole magnets. Depending on the type of measurement being performed, the copper end piece can either be solid bodies (for electron yield measurements) or be hollowed out to fit a PD (e.g., Figure A.1.2(d)) as in the case of a dedicated LY sample holder, referred to as the "LY holder". In the case of the "XFMR holder" shown in Figure A.1.2, the sample end piece is

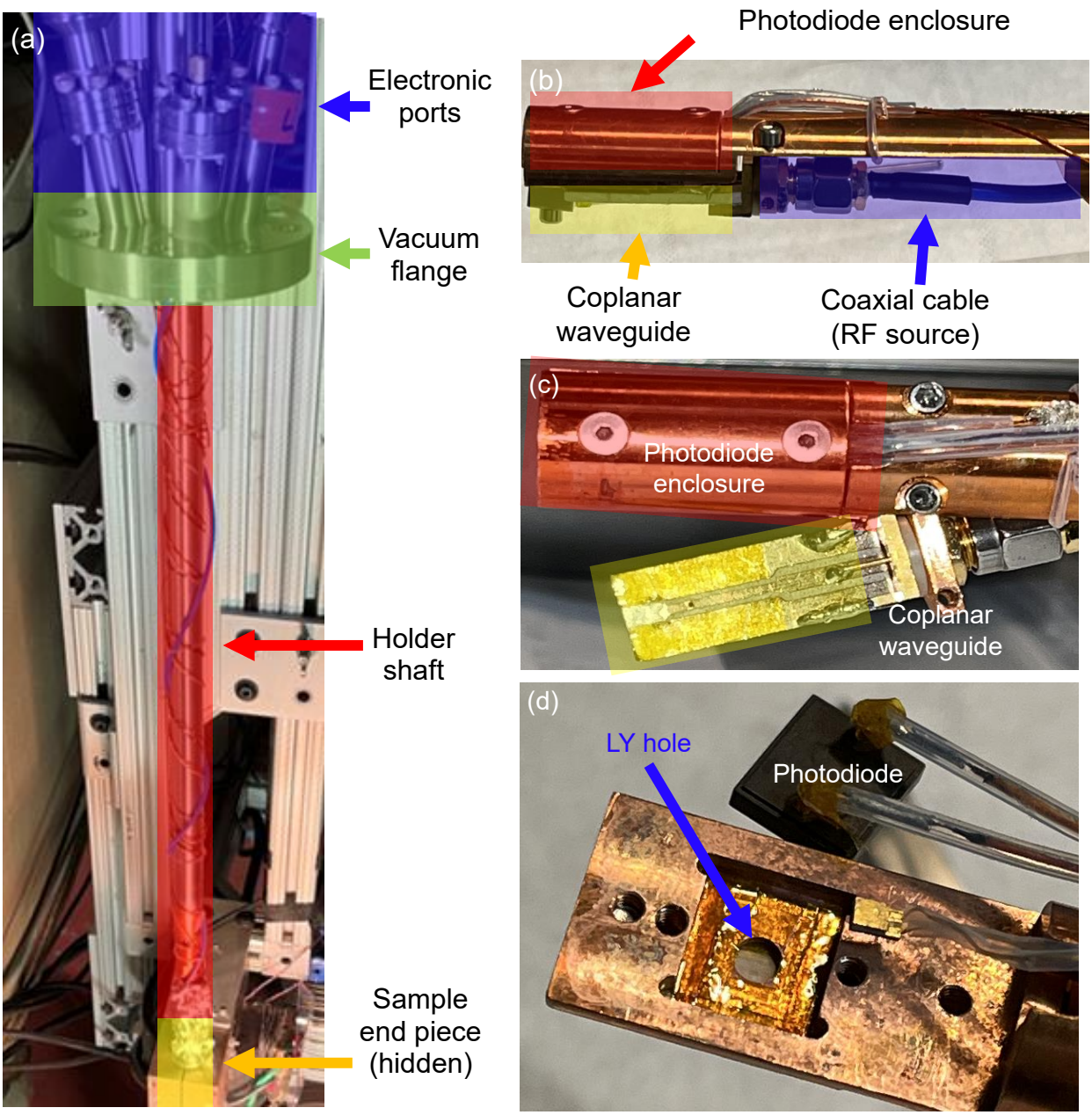

Figure A.1.2: *(a) Picture of the XFMR sample holder used in the VMM endstation at BL 4.0.2. Different functional portions of the holder are color coded and labeled. The actual sample end piece in this image is hidden by part of an testing enclosure that the holder is mounted to. (b) Zoom-in side-view image of the XFMR end piece attached to the end of the sample holder (i.e., yellow region in (a)). (c) Back view of (b) with the coplanar wave guide exposed. (d) Back view of (b) with coplanar wave guide mounted and the photodiode enclosure cap and photodiode*

comprised of two halves and shown in Figure A.1.2(b-d): One half contains the PD while the other half consists of a radio frequency (RF) coplanar waveguide with a ~0.5 mm hole in the center to allow x-rays to pass through (i.e., the small hole in Figure A.1.2(c)). The nominal diameter of the x-ray beam at BL 4.0.2 is about 0.1 mm. The LY flux produced by the x-ray-irradiated sample then travels to the photodiode through a ~3 mm diameter hole (LY hole in Figure A.1.2(d)) drilled through the sample end piece. All electrical connections between the sample end piece and the vacuum flange are tied around the metal shaft to prevent contact with the walls of the vacuum chamber. The holder is designed such that cryogen can also flow through the holder shaft, allowing it to serve as a cold finger which can bring the sample end piece temperature down to ~20 K with liquid helium and ~80 K with liquid nitrogen. Moreover, the holder is equipped with a heater which allows for the sample temperature to be controlled during an experiment. For holders capable of measuring an LY signal (i.e., the LY and XFMR holders), the PD terminals are connected to a Bayonet Neill-Concelman (BNC) vacuum feedthrough flange (i.e., electronic ports in Figure A.1.2(a)). Through this component, the in-vacuum PD leads can be connected to a current amplifier residing outside the vacuum system.

A.1.3 – Optimizing Luminescence Yield Detection Sensitivity

The LY signal detection sensitivity of the XFMR instrument was first compared against the LY holder used for conventional static XAS measurement. In these measurements, the BL 4.0.2 XFMR standard sample comprised of (001)-oriented MgO // 12 nm permalloy / 3 nm Cu was measured on both the LY and XFMR holders. All measurements were performed at room temperature (300 K). Figure A.1.3 shows a comparison between LY photocurrents A_{LY} measured for the two different holders, where “PD-LY” correspond with the LY holder while “PD-AXUV” corresponds with the original XFMR holder AXUV20HS1 from Opto Diode Corporation. To

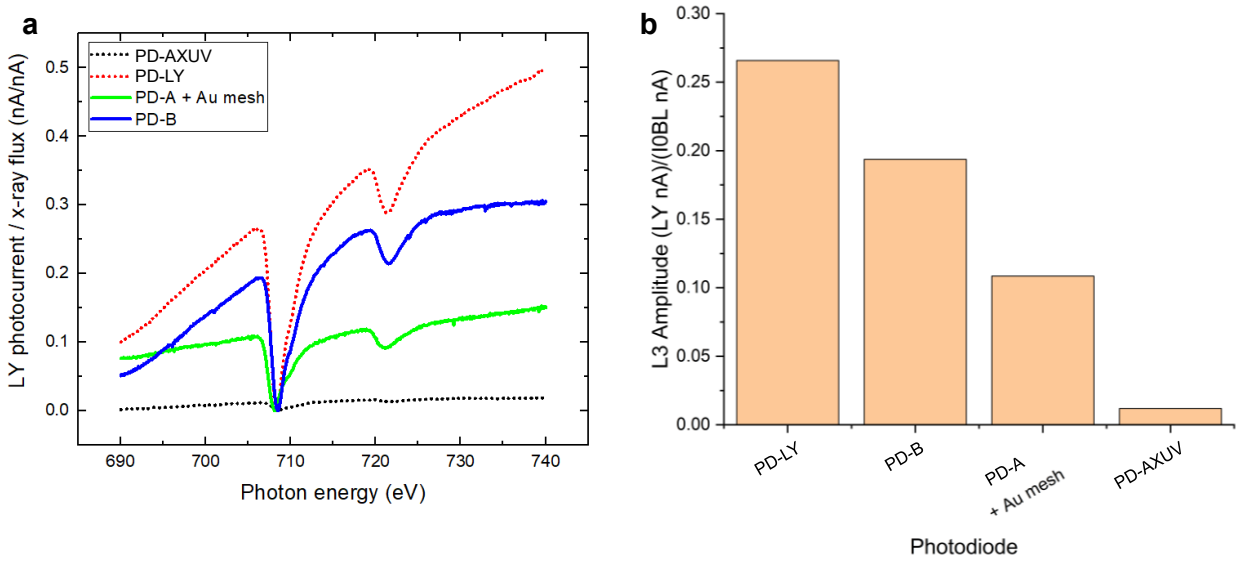

Figure A.1.3: *(a) Fe $L_{2,3}$ spectra for a (001)-oriented MgO // 12 nm permalloy / 3 nm Cu film collected using several photodiode configurations. All spectra have been offset so that the L_3 edge minima is set to zero. The LY signal photocurrent was normalized by the flux of the incident x-ray beam. (b) Comparison of the Fe L_3 amplitude measured for several different photodiode configurations. The amplitude is defined by the maximum intensity in (a) at energies below the L_3 edge.*

consistently compare the signal strength measured across the different hardware and experiment times, all signals were normalized by the incident x-ray flux photocurrent A_{in} which were measured simultaneously with A_{LY}.

As shown in Fig. A.1.3(a), the LY signal produced by the XFMR holder is substantially weaker in comparison to the signal produced detected by the LY holder. By using the amplitudes of the Fe L_3 XAS signal (i.e., the intensity difference between the edge minimum at ~708 eV and the pre-edge maximum at ~706 eV in Fig. A.1.3(a)) as a measure of the signal sensitivity, I found that the XFMR holder is approximately 20 times less sensitive to the LY signal changes compared to the LY holder as shown in Fig. A.1.3(b).

This difference in photodetection sensitivities between the two holders can be explained by the different PDs these systems use. The photosensitivity of a PD, also known as responsivity, quantifies how efficiently the diode produces photocurrent when irradiated with different wavelengths of light. The XFMR holder uses an AXUV20HS1 from Opto Diode Corporation (referred to as the "PD-AXUV") while the LY holder uses an S3588-08 from Hamamatsu Photonics Kabushiki Kaisha (referred to as the "PD-LY"). The responsivities of the PD-AXUV and PD-LY, found in Ref. [143] and Ref. [144] respectively, demonstrate that the former PD is less responsive across the visible light spectrum (400 nm – 700 nm) compared to the latter.

In principle, using the PD-LY in the XFMR holder would resolve any LY signal sensitivity discrepancies between the two instruments. However, several additional constraints must be considered when selecting an optimal diode for XFMR measurements. The first is a geometric constraint associated with utilizing the existing XFMR holder design: the PD must be able to fit within the diode slot (rectangular hole in Figure A.1.2(d)) with dimensions of ~2 mm x 5 mm x 5 mm. The PD-LY is approximately ~30 mm in length and, thus, cannot fit in this holder. Second, the rise time of the PDs must be faster than the rise time of the current amplifier (30 μs) used in the XFMR setup, ideally by at least a factor of 10. Thus, the ideal PD is one which provides the best visible light range responsivity (e.g., the PD-LY), the fastest rise time (e.g., faster than 3 μs), and shares the same form factor as the XFMR PD.

Based on a consideration of these factors, two PDs from Hamamatsu Photonics were selected for testing: the S1337-66BR (PD-A) and S1227-66BR (PD-B). The specifications for PD-A and B can be found in Ref. [145] and [146], respectively. Figure A.1.3(a,b) shows the XAS signal strength of the same permalloy reference sample measured using PD-A and B. These results

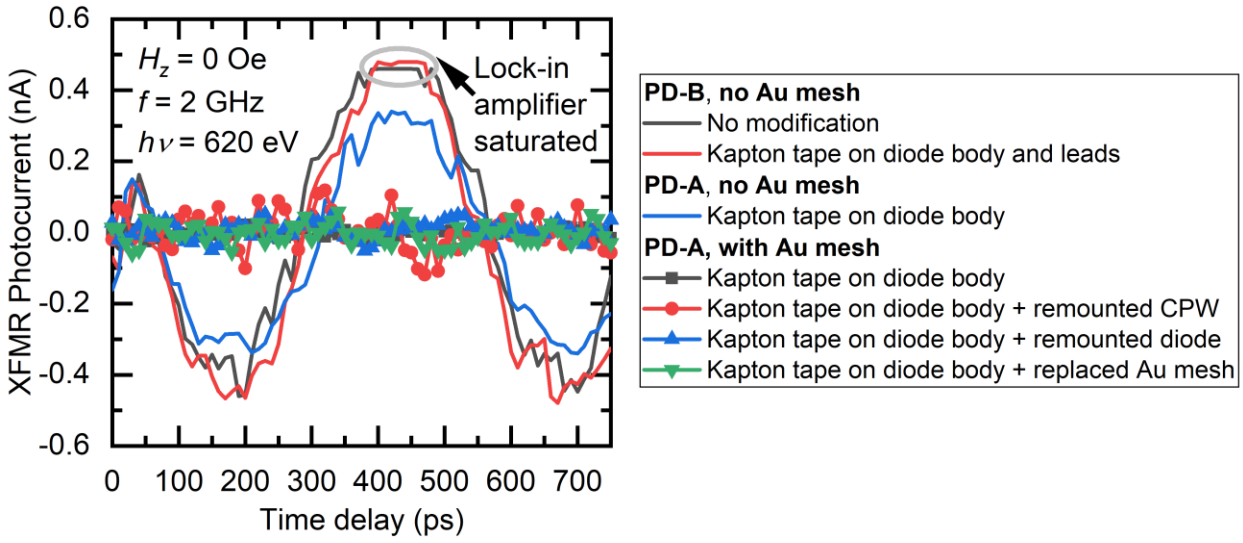

Figure A.1.4: *Comparison of XFMR signals captured with a bare (001)-oriented LSAT substrate for different detector hardware configurations. The applied static field, RF frequency, and photon energy are represented with H_{static}, f, and hv, respectively.*

show that using PD-A and B introduces a near order of magnitude improvement in LY detection sensitivity over the PD-AXUV. For the measurement performed with PD-A, the light received by the diode was partially blocked by a gold mesh covering which is rated to block ~40 % of the visible light transmission. The role of this gold mesh will be discussed in the following section.

I note that a complete comparative study between PD-A and B were not performed due to the limited time available to perform diagnostics on the XFMR instrument *with* soft x-rays. The subsequent use of PD-A and a lack of XAS data for PD-A without the gold mesh were a consequence of *ad hoc* diagnostic decisions made during the beamtime (duration on the order of ~24 hours).

A.1.4 – Identification of an XFMR Artifact Signal

While upgrading the PDs resulted in an improvement to the total LY (i.e., static) detection sensitivity, additional tests were conducted to ensure that the ability to perform XFMR (i.e.,

dynamic) measurements were not compromised. For these tests, a bare (001)-oriented LSAT substrate was measured, which is nominally diamagnetic [147]. All measurements were performed at room temperature (300 K). The purpose of using a non-ferromagnetic sample is to test for the potential presence of artifact signals that may have been introduced by the hardware changes. When measuring ferromagnetic samples, a similar diagnostic test may also be conducted by setting the photon energy to two conditions: (1) the energy which maximizes the static XMCD signal (~0.2 eV lower than the L_3 resonance edge for Mn in LSMO) and (2) off the elemental resonance. In principle, XFMR delay scans (e.g., Figure A.1.4) performed with condition (2) should produce a flat curve as the XFMR signal is fundamentally an XMCD signal and can only be detected near the elemental resonance.

To test for the presence of an artifact signal, I measured XFMR time delay scans for the LSAT substrate and different detector hardware configurations using an H_{RF} frequency of 2 GHz, H_{static} = 0 Oe, and an off-resonance photon energy $h\nu$ = 620 eV. The results of these measurements, shown in Figure A.1.4, indicates that using PD-A and PD-B introduces an anomalous sinusoidal signal which shares the same frequency as H_{RF}. Because the presence of this sinusoidal signal cannot reflect the precessional motion of magnetic moments in the sample (i.e., the photon energy is off resonance and no ferromagnetic materials were used), I concluded that this signal is likely an artifact. This artifact signal was never observed when PD-AXUV was installed in the XFMR holder. The most obvious difference between PD-AXUV and PD-A and B is that the latter two diodes are potted with resin while PD-AXUV is uncapped. However, it remains unclear what additional differences exist between the packaging of PD-AXUV and PD-A and B.

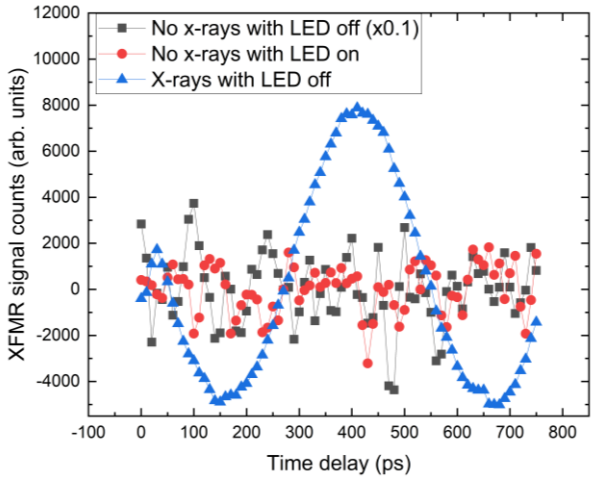

Figure A.1.5: *Comparison of XFMR delay scan line shapes in the presence and absence of x-rays and visible range white light illumination from an LED.*

A.1.5 – Suppression of the XFMR Artifact Signal

In order to benefit from the LY sensitivity improvements PD-A and PD-B offer over the PD-AXUV, the source of the artifact signal must be identified and suppressed. Assuming that the artifact signal does not reflect a time-varying photon absorption of the sample (i.e., some physical process in the sample), it follows that visible-range photons (i.e., the LY yield signal) are not the source of the artifact signal. Two potential sources of the artifact signal are radio transmission from the coplanar waveguide to the PD or photoelectron emission.

To isolate the source of the artifact signal, several diagnostic tests were performed with PD-A installed in the XFMR end piece. Assuming that radio transmission from the coplanar waveguide was the primary source of the artifact, I performed several XFMR measurements using the same bare (001)-oriented LSAT substrate and three different sample illumination conditions: (1) sample is not illuminated by either x-rays or a white light LED, (2) the sample is only illuminated by a white light LED, and (3) the sample is only illuminated by x-rays. All other

experimental parameters (sample temperature, photon energy, H_{static}, and H_{RF} frequency) are identical to those used in Figure A.1.4.

The results of these measurements are shown in Figure A.1.5, which shows that an artifact signal is only clearly observed when the sample is illuminated by x-rays. The observation that the artifact signal production is correlated with x-ray illumination, but not visible light illumination, suggests that x-ray photoemitted electrons may be the primary carrier of the artifact signal. That is, photoelectrons traveling from the sample to the PD via the LY hole may be facilitating the transfer of an RF signal produced by the coplanar wave guide. In previous XFMR holder designs, the PD packaging and terminals had direct line-of-sight to the interior of the VMM vacuum chamber. It was found that XFMR measurements performed with this end piece design contained substantial noise, which was hypothesized to originate from free photoelectrons impacting the PD. The current XFMR holder is designed such that the PD is encased within a copper body which effectively serves as a Faraday cage to prevent the PD from receiving any photoelectrons. However, the current design does not completely isolate the PD from photoelectrons due to the LY hole, which is a necessary design component to allow the sample-produced LY flux to reach the PD. With these observations, I hypothesized that the artifact signal results from the sample-produced photoelectrons impinging on the PD.

While the reasons behind the true nature of the PD-dependent artifact signal transmission and reception remains unclear, investigation into the matter would not be necessary if the PDs can be shielded from the artifact signal source *without* interfering with the detection of visible light. Investigation into the underlying cause of artifact susceptibility in the PDs would be interesting from a scientific standpoint. But due to the limited availability of beamtime (on the order of a few days granted every year), such an in-depth investigation would be impractical. Thus, the aim of

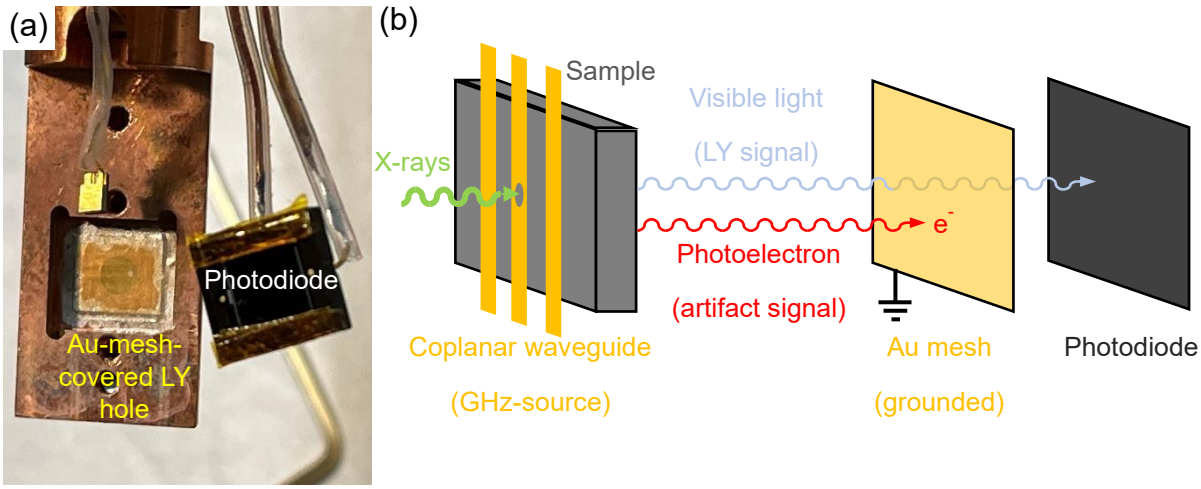

Figure A.1.6: *(a) Image of the XFMR end piece with the Au mesh covering the LY hole. (b) Schematic of the hypothesized mechanism behind the XFMR artifact observed in Figures A.1.4 and A.1.5.*

this portion of the work is not to understand the full nature of the artifact signal production, but to find a solution to suppress this signal.

In principle, the PD can be completely shielded from photoelectrons if the hole was covered with metal foil that is electrically grounded to the rest of the XFMR holder. However, metal foils are generally opaque and would thus prevent the measurement of an LY signal. The solution I conceived was to cover the hole with a thin Au mesh sheet with ~40 μm hole size. As shown in Fig. A.1.6, my hypothesis was that the mesh wire density was sufficient to block all or enough photoelectrons from reaching the PD to produce a detectable artifact signal while allowing sufficient visible light to pass through to produce a meaningful LY signal. The mesh was mounted directly inside the PD-slot of the XFMR holder and was electrically grounded and mechanically adhered to the Cu body using silver paint. To prevent the PD surface from making full contact with

the Au mesh, two ~1 mm x 2 mm x 5 mm rectangular pieces of layered Kapton tape were attached to the top and bottom ends of the surface of PD-B.

The off-resonance XFMR measurements performed with the Au mesh on PD-A is shown in Fig. A.1.4 (all curves with symbols), which clearly demonstrate the lack of an artifact signal (i.e., the time-delay scan is flat). Moreover, this observation is reproducible: even after readjusting the end piece hardware and remounting a new Au mesh piece, the measured XFMR scan remains free of the artifact signal. This observation supports the hypothesis that the artifact signal is carried by photoelectrons traveling down the LY hole which are effectively blocked by the Au mesh. Most importantly, the introduction of the mesh still allows PD-A to collect enough light to outperform the old XFMR photodiode as shown in Figure A.1.3. These measurements show that the combination of PD-A with the Au mesh provides a near order of magnitude improvement in LY sensitivity over the original XFMR hardware when measured on the MgO sample.

A.1.6 – Conclusions

In conclusion, I've investigated and implemented methods to improve the measurement sensitivity of the XFMR instrument at BL 4.0.2. Comparing the LY measurement performance between the XFMR and LY sample holders revealed that the XFMR PD was an order of magnitude less sensitive compared to the PD in the LY holder. Through the installation of new PDs with improved responsivity characteristics in the XFMR end piece, the LY signal strengths measured by the XFMR holder became comparable to those produced by the LY holder. While the new PDs enhanced the LY measurement sensitivity of the XFMR setups, an anomalous artifact signal was introduced into time-resolved XFMR measurements. Instrument diagnostics revealed that the potential carrier of this artifact signal were photoelectrons produced by the x-ray-irradiated sample, which were effectively suppressed by the introduction of a Au mesh layer. This Au mesh enabled

the formation of a full Faraday cage around the PD to isolate the PD from photoelectrons, allowing for the suppression of the artifact signal. The instrumentation work performed in this dissertation will improve the measurement capabilities of the XFMR instrument at BL 4.0.2 by allowing for the detection of smaller LY signals, which in turn improves the acquisition of XFMR signals with higher signal-to-noise ratio. Moreover, the ability to suppress the XFMR artifact signal allows for future upgrades of the photodiode without concerns for potential diode-dependent artifact susceptibility.

Bibliography

[1] S. H. Skjærvø, C. H. Marrows, R. L. Stamps, and L. J. Heyderman, *Advances in Artificial Spin Ice*, Nat. Rev. Phys. **2**, 13 (2020).

[2] R. F. Wang, C. Nisoli, R. S. Freitas, J. Li, W. McConville, B. J. Cooley, M. S. Lund, N. Samarth, C. Leighton, V. H. Crespi, and P. Schiffer, *Artificial "spin Ice" in a Geometrically Frustrated Lattice of Nanoscale Ferromagnetic Islands*, Nature **439**, 303 (2006).

[3] S. Ladak, D. E. Read, G. K. Perkins, L. F. Cohen, and W. R. Branford, *Direct Observation of Magnetic Monopole Defects in an Artificial Spin-Ice System*, Nat. Phys. **6**, 359 (2010).

[4] A. Farhan, M. Saccone, C. F. Petersen, S. Dhuey, R. V. Chopdekar, Y. L. Huang, N. Kent, Z. Chen, M. J. Alava, T. Lippert, A. Scholl, and S. van Dijken, *Emergent Magnetic Monopole Dynamics in Macroscopically Degenerate Artificial Spin Ice*, Sci. Adv. **5**, eaav6380 (2019).

[5] L. J. Heyderman and R. L. Stamps, *Artificial Ferroic Systems: Novel Functionality from Structure, Interactions and Dynamics*, J. Phys. Condens. Matter **25**, 363201 (2013).

[6] V. Kapaklis, U. B. Arnalds, A. Harman-Clarke, E. T. Papaioannou, M. Karimipour, P. Korelis, A. Taroni, P. C. W. Holdsworth, S. T. Bramwell, and B. Hjörvarsson, *Melting Artificial Spin Ice*, New J. Phys. **14**, (2012).

[7] L. Anghinolfi, H. Luetkens, J. Perron, M. G. Flokstra, O. Sendetskyi, A. Suter, T. Prokscha, P. M. Derlet, S. L. Lee, and L. J. Heyderman, *Thermodynamic Phase Transitions in a Frustrated Magnetic Metamaterial*, Nat. Commun. **6**, (2015).

[8] J. Sklenar, Y. Lao, A. Albrecht, J. D. Watts, C. Nisoli, G. W. Chern, and P. Schiffer, *Field-Induced Phase Coexistence in an Artificial Spin Ice*, Nat. Phys. **15**, 191 (2019).

[9] M. T. Kaffash, S. Lendinez, and M. B. Jungfleisch, *Nanomagnonics with Artificial Spin Ice*, Phys. Lett. Sect. A Gen. At. Solid State Phys. **402**, 127364 (2021).

[10] H. Arava, P. M. Derlet, J. Vijayakumar, J. Cui, N. S. Bingham, A. Kleibert, and L. J. Heyderman, *Computational Logic with Square Rings of Nanomagnets*, Nanotechnology **29**, 265205 (2018).

[11] C. Castelnovo, R. Moessner, and S. L. Sondhi, *Spin Ice, Fractionalization, and Topological Order*, Annu. Rev. Condens. Matter Phys. **3**, 35 (2012).

[12] B. C. Dem Hertog and M. J. P. Gingras, *Dipolar Interactions and Origin of Spin Ice in Ising Pyrochlore Magnets*, Phys. Rev. Lett. **84**, 3430 (2000).

[13] R. Moessner, *Magnets with Strong Geometric Frustration*, Can. J. Phys. **79**, 1283 (2001).

[14] N. Rougemaille, F. Montaigne, B. Canals, M. Hehn, H. Riahi, D. Lacour, and J. C. Toussaint, *Chiral Nature of Magnetic Monopoles in Artificial Spin Ice*, New J. Phys. **15**, (2013).

[15] V. Kapaklis, U. B. Arnalds, A. Farhan, R. V. Chopdekar, A. Balan, A. Scholl, L. J. Heyderman, and B. Hjörvarsson, *Thermal Fluctuations in Artificial Spin Ice*, Nat. Nanotechnol. **9**, 514 (2014).

[16] W. R. Branford, S. Ladak, D. E. Read, K. Zeissler, and L. F. Cohen, *Emerging Chirality in Artificial Spin Ice*, Science (80-.). **335**, 1597 (2012).

[17] S. Lendinez and M. B. Jungfleisch, *Magnetization Dynamics in Artificial Spin Ice*, J. Phys. Condens. Matter **32**, (2020).

[18] X. Ke, J. Li, C. Nisoli, P. E. Lammert, W. McConville, R. F. Wang, V. H. Crespi, and P. Schiffer, *Energy Minimization and Ac Demagnetization in a Nanomagnet Array*, Phys.

Rev. Lett. **101**, 037205 (2008).
[19] B. Canals, I. A. Chioar, V. D. Nguyen, M. Hehn, D. Lacour, F. Montaigne, A. Locatelli, T. O. Menteş, B. S. Burgos, and N. Rougemaille, *Fragmentation of Magnetism in Artificial Kagome Dipolar Spin Ice*, Nat. Commun. **7**, 11446 (2016).
[20] F. Montaigne, D. Lacour, I. A. Chioar, N. Rougemaille, D. Louis, S. M. Murtry, H. Riahi, B. S. Burgos, T. O. Menteş, A. Locatelli, B. Canals, and M. Hehn, *Size Distribution of Magnetic Charge Domains in Thermally Activated but Out-of-Equilibrium Artificial Spin Ice*, Sci. Rep. **4**, 1 (2014).
[21] J. Drisko, S. Daunheimer, and J. Cumings, *FePd3 as a Material for Studying Thermally Active Artificial Spin Ice Systems*, Phys. Rev. B **91**, 224406 (2015).
[22] X. Zhang, Y. Lao, J. Sklenar, N. S. Bingham, J. T. Batley, J. D. Watts, C. Nisoli, C. Leighton, and P. Schiffer, *Understanding Thermal Annealing of Artificial Spin Ice*, APL Mater. **7**, 111112 (2019).
[23] R. V. Chopdekar, B. Li, T. A. Wynn, M. S. Lee, Y. Jia, Z. Q. Liu, M. D. Biegalski, S. T. Retterer, A. T. Young, A. Scholl, and Y. Takamura, *Nanostructured Complex Oxides as a Route towards Thermal Behavior in Artificial Spin Ice Systems*, Phys. Rev. Mater. **1**, 024401 (2017).
[24] A. Farhan, P. M. Derlet, A. Kleibert, A. Balan, R. V. Chopdekar, M. Wyss, J. Perron, A. Scholl, F. Nolting, and L. J. Heyderman, *Direct Observation of Thermal Relaxation in Artificial Spin Ice*, Phys. Rev. Lett. **111**, (2013).
[25] Y. Perrin, B. Canals, and N. Rougemaille, *Extensive Degeneracy, Coulomb Phase and Magnetic Monopoles in Artificial Square Ice*, Nature **540**, 410 (2016).
[26] E. Östman, H. Stopfel, I. A. Chioar, U. B. Arnalds, A. Stein, V. Kapaklis, and B. Hjörvarsson, *Interaction Modifiers in Artificial Spin Ices*, Nat. Phys. **14**, 375 (2018).
[27] J. Li, X. Ke, S. Zhang, D. Garand, C. Nisoli, P. Lammert, V. H. Crespi, and P. Schiffer, *Comparing Artificial Frustrated Magnets by Tuning the Symmetry of Nanoscale Permalloy Arrays*, Phys. Rev. B **81**, 092406 (2010).
[28] J. Park, B. L. Le, J. Sklenar, G. W. Chern, J. D. Watts, and P. Schiffer, *Magnetic Response of Brickwork Artificial Spin Ice*, Phys. Rev. B **96**, 024436 (2017).
[29] Y. Li, T. X. Wang, Z. T. Hou, H. Y. Liu, X. F. Dai, and G. D. Liu, *Thermodynamics and Magnetization Reversal in Artificial Brickwork Spin Ice*, Phys. Lett. Sect. A Gen. At. Solid State Phys. **380**, 2013 (2016).
[30] T. Dion, J. C. Gartside, A. Vanstone, K. D. Stenning, D. M. Arroo, H. Kurebayashi, and W. R. Branford, *Observation and Control of Collective Spin-Wave Mode Hybridization in Chevron Arrays and in Square, Staircase, and Brickwork Artificial Spin Ices*, Phys. Rev. Res. **4**, 013107 (2022).
[31] D. Louis, D. Lacour, M. Hehn, V. Lomakin, T. Hauet, and F. Montaigne, *A Tunable Magnetic Metamaterial Based on the Dipolar Four-State Potts Model*, Nat. Mater. **17**, 1076 (2018).
[32] V. M. Parakkat, K. Xie, and K. M. Krishnan, *Tunable Ground State in Heterostructured Artificial Spin Ice with Exchange Bias*, Phys. Rev. B **99**, 54429 (2019).
[33] V. M. Parakkat, G. M. Macauley, R. L. Stamps, and K. M. Krishnan, *Configurable Artificial Spin Ice with Site-Specific Local Magnetic Fields*, Phys. Rev. Lett. **126**, 017203 (2021).
[34] J. Nogués and I. K. Schuller, *Exchange Bias*, J. Magn. Magn. Mater. **192**, 203 (1999).
[35] P. Zubko, S. Gariglio, M. Gabay, P. Ghosez, and J. M. Triscone, *Interface Physics in*

Complex Oxide Heterostructures, Annu. Rev. Condens. Matter Phys. **2**, 141 (2011).
[36] H. Y. Hwang, Y. Iwasa, M. Kawasaki, B. Keimer, N. Nagaosa, and Y. Tokura, *Emergent Phenomena at Oxide Interfaces*, Nat. Mater. **11**, 103 (2012).
[37] J. M. Rondinelli, C. J. Fennie, M. Rondinelli, and C. J. Fennie, *Octahedral Rotation-Induced Ferroelectricity in Cation Ordered Perovskites*, Adv. Mater. **24**, 1961 (2012).
[38] R. D. Shannon, *Revised Effective Ionic Radii and Systematic Studies of Interatomic Distances in Halides and Chalcogenides*, Acta Crystallogr. Sect. A **32**, 751 (1976).
[39] V. M. Goldschmidt, *Die Gesetze Der Krystallochemie*, Naturwissenschaften **14**, 477 (1926).
[40] H. Bethe, *Termaufspaltung in Kristallen*, Ann. Phys. **395**, 133 (1929).
[41] J. Stöhr and H. C. Siegmann, *Magnetism: From Fundamentals to Nanoscale Dynamics* (2006).
[42] N. A. Spaldin, *Magnetic Materials: Fundamentals and Applications* (Cambridge University Press, 2010).
[43] M. Opel, *Spintronic Oxides Grown by Laser-MBE*, J. Phys. D. Appl. Phys. **45**, (2012).
[44] J. B. Goodenough, *Magnetism and the Chemical Bond* (Interscience Publishers, 1963).
[45] J. Kanamori, *Superexchange Interaction and Symmetry Properties of Electron Orbitals*, J. Phys. Chem. Solids **10**, (1959).
[46] P. W. Anderson, *Antiferromagnetism. Theory of Superexchange Interaction*, Phys. Rev. **79**, (1950).
[47] M. Capone, C. J. Ridley, N. P. Funnell, M. Guthrie, and C. L. Bull, *Subtle Structural Changes in LaFeO3 at High Pressure*, Phys. Status Solidi **258**, 2000413 (2021).
[48] J. Hemberger, A. Krimmel, T. Kurz, H. A. Krug von Nidda, V. Y. Ivanov, A. A. Mukhin, A. M. Balbashov, and A. Loidl, *Structural, Magnetic, and Electrical Properties of Single-Crystalline La1-XSrxMnO3 (0.4 < x < 0.85)*, Phys. Rev. B **66**, 1 (2002).
[49] C. Zener, *Interaction between the D-Shells in the Transition Metals. II. Ferromagnetic Compounds of Manganese with Perovskite Structure*, Phys. Rev. **82**, 403 (1951).
[50] A. Urushibara, Y. Moritomo, T. Arima, A. Asamitsu, G. Kido, and Y. Tokura, *Insulator-Metal Transition and Giant Magnetoresistance in La1-XSrxMnO3*, Phys. Rev. B **51**, 14103 (1995).
[51] E. Dagotto, T. Hotta, and A. Moreo, *Colossal Magnetoresistant Materials: The Key Role of Phase Separation*, Phys. Rep. **344**, 1 (2001).
[52] J. H. Park, E. Vescovo, H. J. Kim, C. Kwon, R. Ramesh, and T. Venkatesan, *Direct Evidence for a Half-Metallic Ferromagnet*, Nature **392**, 794 (1998).
[53] J. M. De Teresa, A. Barthélémy, A. Fert, J. P. Contour, F. Montaigne, and P. Seneor, *Role of Metal-Oxide Interface in Determining the Spin Polarization of Magnetic Tunnel Junctions*, Science (80-.). **286**, 507 (1999).
[54] Y. Lu, X. Li, G. Gong, G. Xiao, A. Gupta, P. Lecoeur, and J. Sun, *Large Magnetotunneling Effect at Low Magnetic Fields in Micrometer-Scale EpitaxiaM Tunnel Junctions*, Phys. Rev. B **54**, R8357 (1996).
[55] P. Salev, L. Fratino, D. Sasaki, R. Berkoun, J. del Valle, Y. Kalcheim, Y. Takamura, M. Rozenberg, and I. K. Schuller, *Transverse Barrier Formation by Electrical Triggering of a Metal-to-Insulator Transition*, Nat. Commun. **12**, 5499 (2021).
[56] P. Salev, L. Fratino, D. Sasaki, S. Bag, Y. Takamura, M. Rozenberg, and I. K. Schuller, *Magnetoresistance Anomaly during the Electrical Triggering of a Metal-Insulator Transition*, Phys. Rev. B **108**, 174434 (2023).

[57] P. Salev, I. Volvach, D. Sasaki, P. Lapa, Y. Takamura, V. Lomakin, and I. K. Schuller, *Voltage-Controlled Magnetic Anisotropy Enabled by Resistive Switching*, Phys. Rev. B **107**, 54415 (2023).
[58] M. S. Lee, T. A. Wynn, E. Folven, R. V. Chopdekar, A. Scholl, A. T. Young, S. T. Retterer, J. K. Grepstad, and Y. Takamura, *Tailoring Spin Textures in Complex Oxide Micromagnets*, ACS Nano **10**, 8545 (2016).
[59] Y. Takamura, R. V. Chopdekar, A. Scholl, A. Doran, J. A. Liddle, B. Harteneck, and Y. Suzuki, *Tuning Magnetic Domain Structure in Nanoscale La0.7Sr 0.3MnO 3 Islands*, Nano Lett. **6**, 1287 (2006).
[60] E. J. Kim, J. L. R. Watts, B. Harteneck, A. Scholl, A. Young, A. Doran, and Y. Suzuki, *Magnetic Domain Structure of La0.7Sr0.3MnO 3 Nanoislands: Experiment and Simulation*, J. Appl. Phys. **109**, 07D712 (2011).
[61] A. Hubert and R. Schäfer, *Magnetic Domains. The Analysis of Magnetic Microstructures* (Springer, 1998).
[62] A. Vansteenkiste, J. Leliaert, M. Dvornik, M. Helsen, F. Garcia-Sanchez, and B. Van Waeyenberge, *The Design and Verification of MuMax3*, AIP Adv. **4**, 107133 (2014).
[63] J. Fidler, R. W. Chantrell, T. Schrefl, and M. A. Wongsam, *Micromagnetics: Basic Principles*, in *Encyclopedia of Materials: Science and Technology* (Elsevier, 2001), pp. 5642–5650.
[64] A. Imre, G. Csaba, L. Ji, A. Orlov, G. H. Bernstein, and W. Porod, *Majority Logic Gate for Magnetic Quantum-Dot Cellular Automata*, Science (80-.). **311**, 205 (2006).
[65] J. C. Gartside, K. D. Stenning, A. Vanstone, H. H. Holder, D. M. Arroo, T. Dion, F. Caravelli, H. Kurebayashi, and W. R. Branford, *Reconfigurable Training and Reservoir Computing in an Artificial Spin-Vortex Ice via Spin-Wave Fingerprinting*, Nat. Nanotechnol. 2022 175 **17**, 460 (2022).
[66] H. Arava, N. Leo, D. Schildknecht, J. Cui, J. Vijayakumar, P. M. Derlet, A. Kleibert, and L. J. Heyderman, *Engineering Relaxation Pathways in Building Blocks of Artificial Spin Ice for Computation*, Phys. Rev. Appl. **11**, (2019).
[67] A. Fert, V. Cros, and J. Sampaio, *Skyrmions on the Track*, Nat. Nanotechnol. **8**, 152 (2013).
[68] M. S. N. Tey, X. Chen, A. Soumyanarayanan, and P. Ho, *Chiral Spin Textures for Next-Generation Memory and Unconventional Computing*, ACS Appl. Electron. Mater. **4**, 5088 (2022).
[69] S. S. P. Parkin, M. Hayashi, and L. Thomas, *Magnetic Domain-Wall Racetrack Memory*, Science (80-.). **320**, 190 (2008).
[70] J. W. Matthews and A. E. Blakeslee, *Defects in Epitaxial Multilayers: I. Misfit Dislocations*, J. Cryst. Growth **27**, 118 (1974).
[71] T. F. Kuech, *Integration of Dissimilar Materials*, in *Comprehensive Semiconductor Science and Technology*, Vols. 1–6 (Elsevier, 2011), pp. 1–24.
[72] J. F. Ziegler, M. D. Ziegler, and J. P. Biersack, *SRIM - The Stopping and Range of Ions in Matter (2010)*, Nucl. Instruments Methods Phys. Res. Sect. B Beam Interact. with Mater. Atoms **268**, 1818 (2010).
[73] M. Lee, Designing Magnetic Spin Textures in Complex Oxide Thin Films, University of California, Davis, 2018.
[74] M. Birkholz, *Thin Film Analysis by X-Ray Scattering* (John Wiley and Sons, 2006).
[75] H. Kiessig, *Untersuchungen Zur Totalreflexion von Röntgenstrahlen*, Ann. Phys. **402**, 715

(1931).
[76] A. Glavic and M. Björck, *GenX 3: The Latest Generation of an Established Tool*, J. Appl. Crystallogr. **55**, 1063 (2022).
[77] A. M. Miller, M. Lemon, M. A. Choffel, S. R. Rich, F. Harvel, and D. C. Johnson, *Extracting Information from X-Ray Diffraction Patterns Containing Laue Oscillations*, Zeitschrift Fur Naturforsch. - Sect. B J. Chem. Sci. **77**, 313 (2022).
[78] J. Kowalska and S. DeBeer, *The Role of X-Ray Spectroscopy in Understanding the Geometric and Electronic Structure of Nitrogenase*, Biochim. Biophys. Acta - Mol. Cell Res. **1853**, 1406 (2015).
[79] M. Giménez-Marqués, E. Bellido, T. Berthelot, T. Simón-Yarza, T. Hidalgo, R. Simón-Vázquez, Á. González-Fernández, J. Avila, M. C. Asensio, R. Gref, P. Couvreur, C. Serre, and P. Horcajada, *GraftFast Surface Engineering to Improve MOF Nanoparticles Furtiveness*, Small **14**, 1801900 (2018).
[80] G. van der Laan and A. I. Figueroa, *X-Ray Magnetic Circular Dichroism - A Versatile Tool to Study Magnetism*, Coord. Chem. Rev. **277**, 95 (2014).
[81] T. Kinoshita, *Photoemission Electron Microscope*, in *Compendium of Surface and Interface Analysis* (Springer, Singapore, 2018), pp. 465–469.
[82] I. Gilbert, Y. Lao, I. Carrasquillo, L. O'brien, J. D. Watts, M. Manno, C. Leighton, A. Scholl, C. Nisoli, and P. Schiffer, *Emergent Reduced Dimensionality by Vertex Frustration in Artificial Spin Ice*, Nat. Phys. **12**, 162 (2016).
[83] A. Farhan, A. Scholl, C. F. Petersen, L. Anghinolfi, C. Wuth, S. Dhuey, R. V. Chopdekar, P. Mellado, M. J. Alava, and S. Van Dijken, *Thermodynamics of Emergent Magnetic Charge Screening in Artificial Spin Ice*, Nat. Commun. **7**, 12635 (2016).
[84] E. Mengotti, L. J. Heyderman, A. Fraile Rodríguez, A. Bisig, L. Le Guyader, F. Nolting, and H. B. Braun, *Building Blocks of an Artificial Kagome Spin Ice: Photoemission Electron Microscopy of Arrays of Ferromagnetic Islands*, Phys. Rev. B **78**, 144402 (2008).
[85] L. F. Yin, D. H. Wei, N. Lei, L. H. Zhou, C. S. Tian, G. S. Dong, X. F. Jin, L. P. Guo, Q. J. Jia, and R. Q. Wu, *Magnetocrystalline Anisotropy in Permalloy Revisited*, Phys. Rev. Lett. **97**, 067203 (2006).
[86] Y. Takamura, E. Folven, J. B. R. Shu, K. R. Lukes, B. Li, A. Scholl, A. T. Young, S. T. Retterer, T. Tybell, and J. K. Grepstad, *Spin-Flop Coupling and Exchange Bias in Embedded Complex Oxide Micromagnets*, Phys. Rev. Lett. **111**, 107201 (2013).
[87] E. Folven, J. Linder, O. V. Gomonay, A. Scholl, A. Doran, A. T. Young, S. T. Retterer, V. K. Malik, T. Tybell, Y. Takamura, and J. K. Grepstad, *Controlling the Switching Field in Nanomagnets by Means of Domain-Engineered Antiferromagnets*, Phys. Rev. B **92**, 094421 (2015).
[88] J. Mizusaki, N. Mori, H. Takai, Y. Yonemura, H. Minamiue, H. Tagawa, M. Dokiya, H. Inaba, K. Naraya, T. Sasamoto, and T. Hashimoto, *Oxygen Nonstoichiometry and Defect Equilibrium in the Perovskite-Type Oxides La1-XSrxMnO3+d*, Solid State Ionics **129**, 163 (2000).
[89] J. M. Porro, A. Bedoya-Pinto, A. Berger, and P. Vavassori, *Exploring Thermally Induced States in Square Artificial Spin-Ice Arrays*, New J. Phys. **15**, 055012 (2013).
[90] S. Zhang, I. Gilbert, C. Nisoli, G. W. Chern, M. J. Erickson, L. O'Brien, C. Leighton, P. E. Lammert, V. H. Crespi, and P. Schiffer, *Crystallites of Magnetic Charges in Artificial Spin Ice*, Nature **500**, 553 (2013).

[91] E. Folven, T. Tybell, A. Scholl, A. Young, S. T. Retterer, Y. Takamura, and J. K. Grepstad, *Antiferromagnetic Domain Reconfiguration in Embedded LaFeO3 Thin Film Nanostructures*, Nano Lett. **10**, 4578 (2010).
[92] L. M. Berndt, V. Balbarin, and Y. Suzuki, *Magnetic Anisotropy and Strain States of (001) and (110) Colossal Magnetoresistance Thin Films*, Appl. Phys. Lett. **77**, 2903 (2000).
[93] A. Doran, M. Church, T. Miller, G. Morrison, A. T. Young, and A. Scholl, *Cryogenic PEEM at the Advanced Light Source*, J. Electron Spectros. Relat. Phenomena **185**, 340 (2012).
[94] G. Danuser, *Computer Vision in Cell Biology*, Cell **147**, 973 (2011).
[95] Y. Rubner, C. Tomasi, and L. J. Guibas, *Earth Mover's Distance as a Metric for Image Retrieval*, Int. J. Comput. Vis. **40**, 99 (2000).
[96] E. Y. Tsymbal, *Theory of Magnetostatic Coupling in Thin-Film Rectangular Magnetic Elements*, Appl. Phys. Lett. **77**, 2740 (2000).
[97] R. Álvarez-Sánchez, J. L. Costa-Krämer, and F. Briones, *Analytical Model for Shape Anisotropy in Thin-Film Nanostructured Arrays: Interaction Effects*, J. Magn. Magn. Mater. **307**, 171 (2006).
[98] A. M. Kane, I.-T. Chiu, N. J. Ahlm, R. V Chopdekar, A. T. N'Diaye, E. Arenholz, A. Mehta, V. Lauter, and Y. Takamura, *Controlling Magnetization Vector Depth Profiles of La0.7Sr0.3CoO3/La0.7Sr0.3MnO3 Exchange Spring Bilayers via Interface Reconstruction*, ACS Appl. Mater. Interfaces **12**, 45437 (2020).
[99] A. M. Kane, R. V Chopdekar, A. T. N'Diaye, A. Scholl, E. Arenholz, A. Mehta, and Y. Takamura, *Decoupling Exchange Bias and Coercivity Enhancement in a Perovskite Oxide Exchange Spring Bilayer*, Phys. Rev. Mater. **3**, 14413 (2019).
[100] W. Eerenstein, M. Wiora, J. L. Prieto, J. F. Scott, and N. D. Mathur, *Giant Sharp and Persistent Converse Magnetoelectric Effects in Multiferroic Epitaxial Heterostructures*, Nat. Mater. **6**, 348 (2007).
[101] B. Náfrádi, P. Szirmai, M. Spina, A. Pisoni, X. Mettan, N. M. Nemes, L. Forró, and E. Horváth, *Tuning Ferromagnetism at Room Temperature by Visible Light*, Proc. Natl. Acad. Sci. U. S. A. **117**, 6417 (2020).
[102] D. Petti, S. Tacchi, and E. Albisetti, *Review on Magnonics with Engineered Spin Textures*, J. Phys. D. Appl. Phys. **55**, 293003 (2022).
[103] Z. Gu, M. E. Nowakowski, D. B. Carlton, R. Storz, M. Y. Im, J. Hong, W. Chao, B. Lambson, P. Bennett, M. T. Alam, M. A. Marcus, A. Doran, A. Young, A. Scholl, P. Fischer, and J. Bokor, *Sub-Nanosecond Signal Propagation in Anisotropy-Engineered Nanomagnetic Logic Chains*, Nat. Commun. **6**, 6466 (2015).
[104] B. Van Waeyenberge, A. Puzic, H. Stoll, K. W. Chou, T. Tyliszczak, R. Hertel, M. Fähnle, H. Brückl, K. Rott, G. Reiss, I. Neudecker, D. Weiss, C. H. Back, & G. Schütz, G. Schütz, and & G. Schütz, *Magnetic Vortex Core Reversal by Excitation with Short Bursts of an Alternating Field*, Nature **444**, 461 (2006).
[105] N. Nagaosa and Y. Tokura, *Topological Properties and Dynamics of Magnetic Skyrmions*, Nat. Nanotechnol. **8**, 899 (2013).
[106] M. Saccone, J. C. Gartside, K. D. Stenning, W. R. Branford, and F. Caravelli, *From Vertices to Vortices in Magnetic Nanoislands*, Phys. Fluids **35**, 17101 (2023).
[107] E. Folven, A. Scholl, A. Young, S. T. Retterer, J. E. Boschker, T. Tybell, Y. Takamura, and J. K. Grepstad, *Crossover from Spin-Flop Coupling to Collinear Spin Alignment in Antiferromagnetic/Ferromagnetic Nanostructures*, Nano Lett. **12**, 2386 (2012).

[108] C. C. Chang, Y. C. Chang, W. S. Chung, J. C. Wu, Z. H. Wei, M. F. Lai, and C. R. Chang, *Influences of the Aspect Ratio and Film Thickness on Switching Properties of Elliptical Permalloy Elements*, IEEE Trans. Magn. **41**, 947 (2005).
[109] D. Y. Sasaki, R. V. Chopdekar, S. T. Retterer, D. Y. Jiang, J. K. Mason, M. S. Lee, and Y. Takamura, *Formation of Complex Spin Textures in Thermally Demagnetized La0.7Sr0.3Mn O3 Artificial-Spin-Ice Structures*, Phys. Rev. Appl. **17**, 064057 (2022).
[110] R. Puttock, A. Manzin, V. Neu, F. Garcia-Sanchez, A. Fernandez Scarioni, H. W. Schumacher, O. Kazakova, O. R. Kazakova Puttock, O. Kazakova, R. Puttock, A. Manzin, F. Garcia-Sanchez, V. Neu, A. Fernandez Scarioni, and H. W. Schumacher, *Modal Frustration and Periodicity Breaking in Artificial Spin Ice*, Small **16**, 2003141 (2020).
[111] A. Talapatra, N. Singh, and A. O. Adeyeye, *Magnetic Tunability of Permalloy Artificial Spin Ice Structures*, Phys. Rev. Appl. **13**, 14034 (2020).
[112] J. Ahrens, B. Geveci, and C. Law, *ParaView: An End-User Tool for Large-Data Visualization*, Vis. Handb. 717 (2005).
[113] S. Gliga, G. Hrkac, C. Donnelly, J. Büchi, A. Kleibert, J. Cui, A. Farhan, E. Kirk, R. V. Chopdekar, Y. Masaki, N. S. Bingham, A. Scholl, R. L. Stamps, and L. J. Heyderman, *Emergent Dynamic Chirality in a Thermally Driven Artificial Spin Ratchet*, Nat. Mater. **16**, 1106 (2017).
[114] A. Farhan, A. Kleibert, P. M. Derlet, L. Anghinolfi, A. Balan, R. V. Chopdekar, M. Wyss, S. Gliga, F. Nolting, and L. J. Heyderman, *Thermally Induced Magnetic Relaxation in Building Blocks of Artificial Kagome Spin Ice*, Phys. Rev. B **89**, (2014).
[115] A. Farhan, P. M. Derlet, A. Kleibert, A. Balan, R. V. Chopdekar, M. Wyss, L. Anghinolfi, F. Nolting, and L. J. Heyderman, *Exploring Hyper-Cubic Energy Landscapes in Thermally Active Finite Artificial Spin-Ice Systems*, Nat. Phys. **9**, 375 (2013).
[116] A. Farhan, C. F. Petersen, S. Dhuey, L. Anghinolfi, Q. H. Qin, M. Saccone, S. Velten, C. Wuth, S. Gliga, P. Mellado, M. J. Alava, A. Scholl, and S. Van Dijken, *Nanoscale Control of Competing Interactions and Geometrical Frustration in a Dipolar Trident Lattice*, Nat. Commun. **8**, 995 (2017).
[117] H. Saglam, A. Duzgun, A. Kargioti, N. Harle, X. Zhang, N. S. Bingham, Y. Lao, I. Gilbert, J. Sklenar, J. D. Watts, J. Ramberger, D. Bromley, R. V Chopdekar, L. O'Brien, C. Leighton, C. Nisoli, and P. Schiffer, *Entropy-Driven Order in an Array of Nanomagnets*, Nat. Phys. **18**, 706 (2022).
[118] N. D. Lepley, N. A. W. Holzwarth, W. M. Young, and E. W. Elcock, *Monte Carlo Studies of Vacancy Migration in Binary Ordered Alloys: I*, Proc. Phys. Soc. **89**, 735 (1966).
[119] G. M. Macauley, G. W. Paterson, Y. Li, R. Macêdo, S. Mcvitie, and R. L. Stamps, *Tuning Magnetic Order with Geometry: Thermalization and Defects in Two-Dimensional Artificial Spin Ices*, Phys. Rev. B **101**, 144403 (2020).
[120] Y. Li, G. W. Paterson, G. M. MacAuley, F. S. Nascimento, C. Ferguson, S. A. Morley, M. C. Rosamond, E. H. Linfield, D. A. MacLaren, R. MacEdo, C. H. Marrows, S. McVitie, and R. L. Stamps, *Superferromagnetism and Domain-Wall Topologies in Artificial "Pinwheel" Spin Ice*, ACS Nano **13**, 2213 (2019).
[121] S. A. Morley, J. M. Porro, A. Hrabec, M. C. Rosamond, D. A. Venero, E. H. Linfield, G. Burnell, M. Y. Im, P. Fischer, S. Langridge, and C. H. Marrows, *Thermally and Field-Driven Mobility of Emergent Magnetic Charges in Square Artificial Spin Ice*, Sci. Rep. **9**, 1 (2019).
[122] J. M. Porro, S. A. Morley, D. A. Venero, R. Macêdo, M. C. Rosamond, E. H. Linfield, R.

L. Stamps, C. H. Marrows, and S. Langridge, *Magnetization Dynamics of Weakly Interacting Sub-100 Nm Square Artificial Spin Ices*, Sci. Rep. **9**, (2019).
[123] M. S. Lee, P. Lyu, R. V. Chopdekar, A. Scholl, S. T. Retterer, and Y. Takamura, *Controlling Antiferromagnetic Domains in Patterned La 0.7 Sr 0.3 FeO 3 Thin Films* , J. Appl. Phys. **127**, 203901 (2020).
[124] S. Bedanta and W. Kleemann, *Supermagnetism*, J. Phys. D. Appl. Phys. **42**, 013001 (2009).
[125] S. Krause, G. Herzog, T. Stapelfeldt, L. Berbil-Bautista, M. Bode, E. Y. Vedmedenko, and R. Wiesendanger, *Magnetization Reversal of Nanoscale Islands: How Size and Shape Affect the Arrhenius Prefactor*, Phys. Rev. Lett. **103**, 127202 (2009).
[126] H. F. Ding, A. K. Schmid, D. Li, K. Y. Guslienko, and S. D. Bader, *Magnetic Bistability of Co Nanodots*, Phys. Rev. Lett. **94**, (2005).
[127] K. Y. Guslienko, V. Novosad, Y. Otani, H. Shima, and K. Fukamichi, *Magnetization Reversal Due to Vortex Nucleation, Displacement, and Annihilation in Submicron Ferromagnetic Dot Arrays*, Phys. Rev. B **65**, 244141 (2002).
[128] A. Pushp, T. Phung, C. Rettner, B. P. Hughes, S. H. Yang, L. Thomas, and S. S. P. Parkin, *Domain Wall Trajectory Determined by Its Fractional Topological Edge Defects*, Nat. Phys. **9**, 505 (2013).
[129] T. S. MacHado, T. G. Rappoport, and L. C. Sampaio, *Vortex Core Magnetization Dynamics Induced by Thermal Excitation*, Appl. Phys. Lett. **100**, 112404 (2012).
[130] G. M. Wysin and W. Figueiredo, *Thermal Vortex Dynamics in Thin Circular Ferromagnetic Nanodisks*, Phys. Rev. B **86**, 104421 (2012).
[131] V. Novosad, K. Y. Guslienko, H. Shima, Y. Otani, S. G. Kim, K. Fukamichi, N. Kikuchi, O. Kitakami, and Y. Shimada, *Effect of Interdot Magnetostatic Interaction on Magnetization Reversal in Circular Dot Arrays*, Phys. Rev. B **65**, 060402 (2002).
[132] C. Klewe, Q. Li, M. Yang, A. T. N'Diaye, D. M. Burn, T. Hesjedal, A. I. Figueroa, C. Hwang, J. Li, R. J. Hicken, P. Shafer, E. Arenholz, G. van der Laan, and Z. Qiu, *Element- and Time-Resolved Measurements of Spin Dynamics Using X-Ray Detected Ferromagnetic Resonance*, Synchrotron Radiat. News **33**, 12 (2020).
[133] C. Klewe, S. Emori, Q. Li, M. Yang, B. A. Gray, H. M. Jeon, B. M. Howe, Y. Suzuki, Z. Q. Qiu, P. Shafer, and E. Arenholz, *Experimental Realization of Linearly Polarized X-Ray Detected Ferromagnetic Resonance*, New J. Phys. **24**, (2022).
[134] G. van der Laan and T. Hesjedal, *X-Ray Detected Ferromagnetic Resonance Techniques for the Study of Magnetization Dynamics*, Nucl. Instruments Methods Phys. Res. Sect. B Beam Interact. with Mater. Atoms **540**, 85 (2023).
[135] G. Boero, S. Rusponi, P. Bencok, R. S. Popovic, H. Brune, and P. Gambardella, *X-Ray Ferromagnetic Resonance Spectroscopy*, Appl. Phys. Lett. **87**, 1 (2005).
[136] T. K. Sham, *X-Ray Excited Optical Luminescence*, in *International Tables for Crystallography Volume I*, edited by C. T. Chantler, F. Boscherini, and B. Bunker (International Union of Crystallography, 2022), pp. 1–11.
[137] C. Piamonteze, Y. W. Windsor, S. R. V. Avula, E. Kirkc, and U. Staub, *Soft X-Ray Absorption of Thin Films Detected Using Substrate Luminescence: A Performance Analysis*, J. Synchrotron Radiat. **27**, 1289 (2020).
[138] S. Chikazumi and S. Charap, *Physics of Ferromagnetism* (John Wiley and Sons, New York, 1964).
[139] V. Franco and B. Dodrill, *Magnetic Measurement Techniques for Materials*

Characterization (2021).
[140] J. R. Fermin, A. Azevedo, F. M. De Aguiar, B. Li, and S. M. Rezende, *Ferromagnetic Resonance Linewidth and Anisotropy Dispersions in Thin Fe Films*, J. Appl. Phys. **85**, 7316 (1999).
[141] *Machine Information*, https://als.lbl.gov/machine-information/.
[142] E. Arenholz and S. O. Prestemon, *Octupole Magnet For Soft X Ray Magnetic Dichroism Experiments: Design and Performance*, AIP Conf. Proc. **705**, 1170 (2004).
[143] Opto Diode Corporation, *AXUV20HS1*.
[144] Hamamatsu Photonics Kabushiki Kaisha, *Si PIN Photodiode S2744/S3588-08, -09 Large*.
[145] Hamamatsu Photonics Kabushiki Kaisha, *Si Photodiodes S1337 Series*, 6 (2015).
[146] Hamamatsu Photonics Kabushiki Kaisha, *Si Photodiodes S1227 Series*, 5 (2015).
[147] M. Khalid, A. Setzer, M. Ziese, P. Esquinazi, D. Spemann, A. Pöppl, and E. Goering, *Ubiquity of Ferromagnetic Signals in Common Diamagnetic Oxide Crystals*, Phys. Rev. B - Condens. Matter Mater. Phys. **81**, 214414 (2010).
[148] A. J. Haider, T. Alawsi, M. J. Haider, B. A. Taha, and H. A. Marhoon, *A Comprehensive Review on Pulsed Laser Deposition Technique to Effective Nanostructure Production: Trends and Challenges*, Optical and Quantum Electronics.
[149] G. F. Harrington and J. Santiso, *Back-to-Basics Tutorial: X-Ray Diffraction of Thin Films*, J. Electroceramics **47**, 141 (2021).